UNIVERSITÀ DEGLI STUDI DI MILANO

Scuola di Dottorato in Fisica, Astrofisica e Fisica Applicata

Dipartimento di Fisica

Corso di Dottorato in Fisica, Astrofisica e Fisica Applicata

Ciclo XXIV

ADDITIVE MICRO- AND NANOPATTERNING FOR THE FABRICATION OF BRAIN CELL NETWORKS

Settore Scientifico Disciplinare FIS/03

Supervisore: Professor Paolo MILANI

Coordinatore: Professor Matteo PARIS

Tesi di Dottorato di:

Anita Previdi

Anno Accademico 2020/2021

External referees:

Dr. Leandro Lorenzelli
Center for Materials and Microsystems (CMM)
FBK - Foundation Bruno Kessler

Prof. Stefano Vassanelli
Department of Biomedical Sciences
University of Padova

Commission of the final examination:

Prof. Paolo Milani
CIMaINa, Department of Physics
University of Milan

Prof. Antonio Malgaroli
Center for Behavioral Neuroscience and Communication (BNC)
University Vita-Salute San Raffaele

Prof. Francesco Greco
Istituto di BioRobotica
Scuola Superiore Sant'Anna

Final examination:

20/01/2022

University of Milan, Department of Physics, Milan, Italy

Cover illustration:

Immunofluorescence images of primary hippocampal astrocytes confined on micropatterned zirconia dots, fixed and stained after 3 DIV. The actin cytoskeleton is stained with phalloidin, tetramethylrhodamine (TRITC-conjugated, red) and the cell nucleus with Hoechst 33,342 (blue).

MIUR subjects:

FIS/03

PACS:

81.07.-b

Contents

Introduction

0.1 The complexity of the human brain

Today, we are at a stage of technological development where it is reasonable to compare, in terms of performance, human brains and the central processing units (CPU)s of computers. Both systems are composed of a huge number of highly interconnected elementary units that exchange electric signals. However, technology is still nowhere near the realization of CPUs able to reproduce the sophisticated functions of the brain, namely *learning*, with the same robustness, adaptive abilities [1] and low power consumption [2].

The human brain comprises an estimated number of 10^{11} neurons, which form 10^{15} synaptic connections between them [3]. Synapses are plastic, meaning that their strength can be modified according to the activity of pre- and post-synaptic neurons [4]. Human brains are believed to owe their powerful computational performance to their structurally complex, parallel and self-organizing architecture [5]. Communication within the nervous system takes place over many scales [6], see Fig. 1. At the single cell level, intracellular signaling comprises protein-protein interactions and propagation of second messengers [4], whereas neurons and glia, connected at synapses, exchange transmitters [7]. Ensembles of cells form local circuits which are, in turn, interconnected at the brain-wide level [6]. While we understand the basic principles underlying synaptic transmission between neurons, it is unclear how cells interact together in local circuits, and then on a global scale. Any attempt to understand the working mechanisms of the brain by recording the activity of every single neuron is not only technically unfeasible, but it might also be unnecessary. Despite its staggering complexity, there is evidence the cognitive functions of the brain arise from the activation of subpopulations of neurons in distributed networks [8].

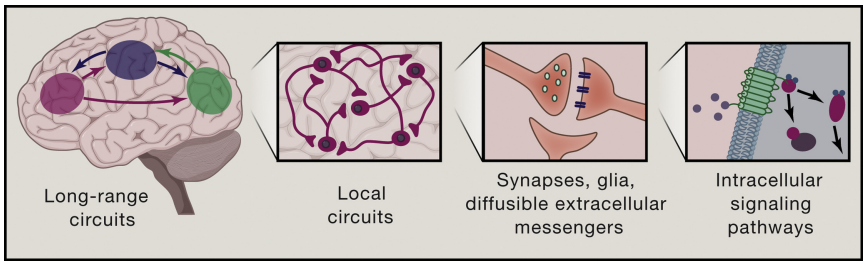

Figure 1: Scheme of the different scales over which nervous systems communicate. From left to right, information transfer takes place at the brain-wide level, within local circuits, at the intercellular (synaptic) level, and the intracellular level. Reproduced with permission [6]. Copyright ©2016 Elsevier Inc.

Unraveling how the human brain stores and processes information could lead to a better understanding of neural diseases and provide the key for improved brain machine interfaces [9]. From the technological point of view, the study of the mechanisms underlying data processing in the brain are source of inspiration to find novel hardware and software solutions to overcome the intrinsic limitation of the digital computer paradigm [10–12].

0.1.1 The connectome: a structural and functional map of the brain

In the last decades, scientists have been mapping the so-called connectome [3], i.e. the complex wiring diagram of structural connections of the central nervous system (CNS). The scheme reported in Fig. 2 conveys the idea of the complexity of such systems, as it shows the connectome of the *Caenorhabditis elegans*, a nematode whose nervous system is composed of only 302 neurons [13]. Even in this small network, the neurons are linked by a labyrinth of thousands of synaptic connections [13].

The connectome constitutes the anatomical foundation of neuronal signaling and integration. The more and more precise characterization of the connectome greatly contributed to the elucidation of the organizational principles underlying brain connectivity, thus offering a solid anatomical and functional substrate for the understanding of the cognitive system. The human connectome originates from two main driving forces [14, 15]. The first tends to minimize the physical and metabolic cost of wiring, promotes modularity and the formation of local circuits. The second is apt to the maximization of network efficiency, that enables information transfer and integration between anatomically and functionally distant neurons or brain regions. These forces are responsible for the multiscale architecture of the brain, based on a large-scale network of cortical areas that supports and integrates brain functions distributed across spatially segregated regions [16]. Recent literature recognized alterations in the connectome as a hallmark

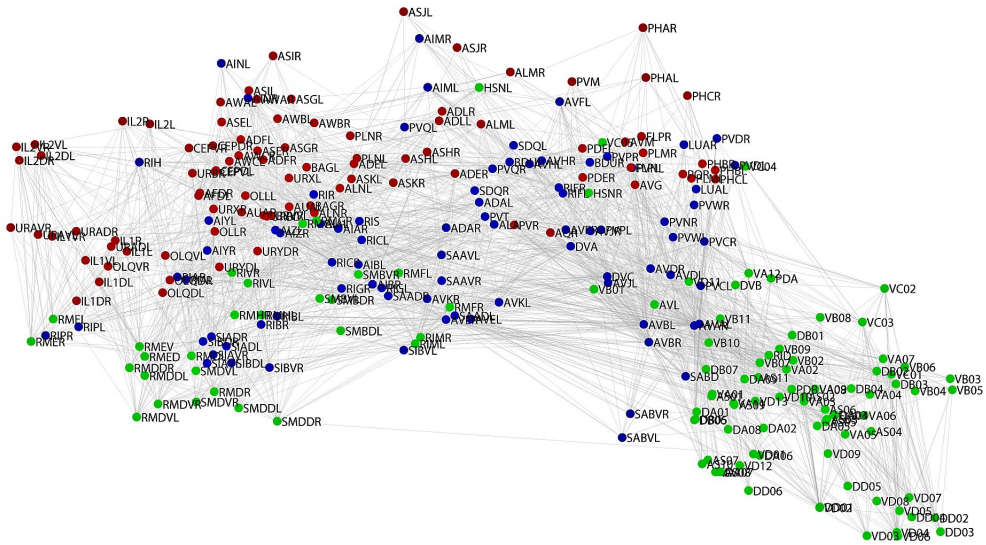

Figure 2: A visualization of brain complexity: the connectome of *Caenorhabditis elegans*, comprising all its 302 neurons and their chemical synapses. The three-letter labels indicate different neurons. Reproduced (adapted) with permission [13]. Copyright ©2011 Varshney *et al.*

of brain pathology [17, 18], highlighting potentially shared network mechanisms that underpin brain dysfunctions.

Lately, it has been proposed that a connectome comprising only neurons would make an incomplete map of the anatomical and functional connectivity in the brain [19]. A more realistic description should also include glial cells, which, with neurons, constitute its building blocks [4]. Previously believed to fulfill an ancillary role to neurons by providing metabolic support, it is now clear that glial cells impact on brain connectivity both on a structural and functional level [20, 21]. They form networks in which information is propagated with signaling mechanisms at temporal and spatial scales different from their neuronal counterpart [22]. At the same time, they communicate with neurons and integrate information processing [23, 24]. Also, they have an active role in modulating their synaptic connectivity [19]. This view adds a significant degree of complexity to the system, especially because the research on glial communication is in its infancy and many aspects are still to be clarified. Nonetheless, the contribution of glia in brain functioning cannot be neglected.

0.1.2 Bottom-up neuroscience

While the field of connectomics is providing a full anatomical framework for brain wiring maps and neurobiology is clarifying the molecular intricacy of the nervous system, there

are still insufficient strategies to understand the connection between the structural motif of brain circuits and their functioning at a network level. Often, to study brain cell ensembles, scientists focus on specific realizations of brain structures in the framework of particular cognitive functions, for instance the role of the hippocampus in learning [8]. This approach, although effective for discerning brain pathology, does not allow a comprehensive and coherent understanding of the underlying basic mechanisms of cognitive behavior [8].

Experimental research in this field is incredibly challenging due to the dynamic complexities of the brain. The high synaptic connectivity hampers the possibility to probe the correlations between structure and function of isolated circuits. The challenge is further complicated because the structure of the vast majority of behaviorally relevant brain cell circuits are not mere consequences of genetics, rather they are formed and continuously modulated by stimuli-dependent learning mechanisms [8] that ensure adaptation to environmental inputs. Similarly, despite the development of neuroimaging methods to monitor activity in real-time and in physiological environments, *in vivo* cell networks are constantly subjected to chemical stimuli that modulate the properties of single neurons, glial cells, synapses, or local circuits and that are impossible to control e.g., amines, neuropeptides, gases, and other molecules [25–31].

Among the strategies to reduce the number of variables and study the brain in a controlled environment, there are computational models that can offer sophisticated theories on brain cell network functionality [32, 33]. However they are often difficult to test and pair directly with mechanisms occurring *in vivo*, so it is also necessary to develop technologies that allow the realization of experiments with real biological entities, where the system variables can be minimized and systematically monitored.

A rewarding strategy, complementary to theoretical and *in vivo* research, is bottom-up neuroscience, which promotes the understanding of the brain step-by-step via engineering and analyzing small and well-defined neural networks *in vitro* as a representation of elementary brain functions [34]. Standard cultures of brain cells form intricate networks with random connections, where only global, network-wide properties can be observed. Whereas small networks of brain cells cultured *in vitro* can be tailored to match specific geometric designs or the arrangement of electrode arrays used to both stimulate and record their activity. In this way, it is possible to reproduce circuits of cells with controlled topological properties, in conditions where the number and subtypes of cells and their connectivity patterns are precisely determined *a priori*, see Fig. 3.

In vitro tailored brain cell cultures recapitulate an incredibly rich catalog of behaviors present *in vivo*, including growth and differentiation [36], plasticity [37], electrical activity [38] and information processing [39]. Therefore, they represent a practical tool to un-

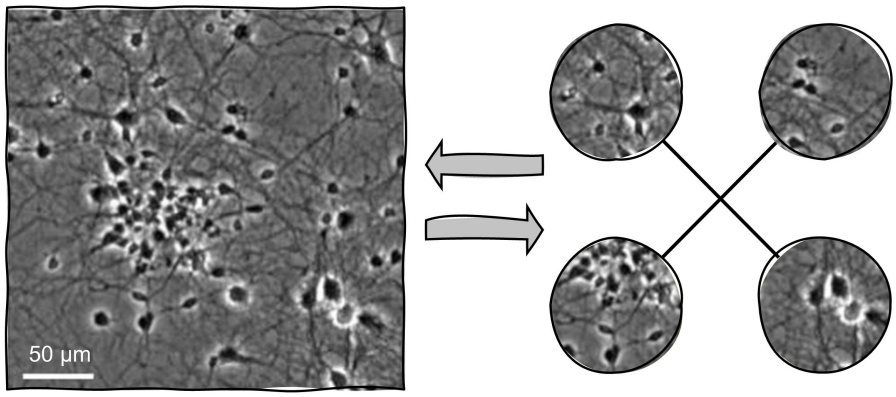

Figure 3: Schematic representation of the idea of bottom-up neuroscience. The aim is to minimize the number of variables of random neuronal cultures (left image) by building simple neuronal networks of well-defined topologies (right image). Reproduced (adapted) with permission [35].

derstand the nervous system, from the molecular actors of neuronal and glial functions, to the behaviors produced by embodied cultures [40]. Interfacing brain cell cultures with patterned substrates able to recapitulate the complexity experienced by neurons and glia *in vivo* is therefore a necessary step to understand and control many of these processes.

Achieving spatial control of cell networks is a major challenge, since it requires a strong integration of neurobiological, material science and nanotechnology expertise for the development of culture substrates able to constrain the adhesion of individual living cells on predefined substrate areas, see Fig. 4 for some examples. The fabrication of micropatterned substrates that control cell adhesion are typically based on processes for the selective modification of the surface chemical properties [44–46]. For example, photolithography and microcontact printing have been employed for creating micropatterns of adhesive molecules (e.g. proteins of the ECM like matrigel, laminin, fibronectin, or poly-D-lysine [42, 47, 48]) on surfaces functionalized to be cell repelling (e.g. with PLL-PEG [49] or agarose layer [50]). With inkjet printers it is possible to directly deposit patterns of adhesive molecules on substrates [51] or even single cells [52]. Also, patterns can be obtained with photosensitive molecules whose adhesive properties can be changed with UV light [53, 54]. Among the approaches that do not entail surface chemistry modification there are PDMS microchannel structures (fabricated with soft lithography) [41] or patterns of functionalized gold nanopillars (fabricated with ion beam milling) [43] able confine cell somas and guide axon growth.

These techniques, although effective in confining cells, often provide substrates that are quite different from the natural environment in which brain cells grow, thus hampering their physiological development. It has been recognized that a mere material

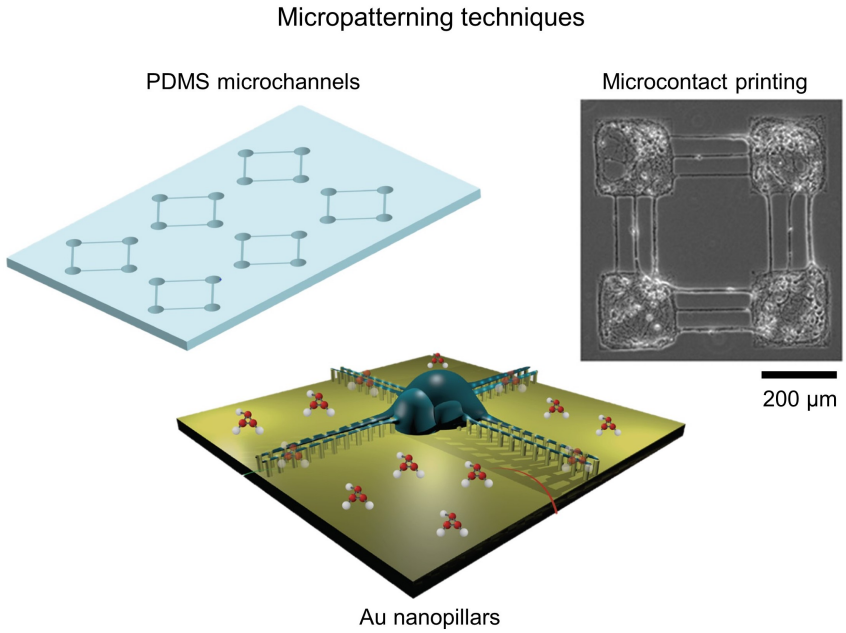

Figure 4: Examples of micropatterning techniques for the reproduction of controlled neural networks *in vitro*. On the top left, a PDMS microstructured circuit: the round wells host the neuronal bodies, the channels are for the axons. Reproduced (adapted) with permission from [41]. Copyright ©2018 Elsevier B.V. On the top right, a phase-contrast micrograph of a neural network obtained by culturing cells on an agarose-coated coverslip with adhesive areas composed of a mixture of poly-D-lysine and extra-cellular matrix (ECM) gel, delivered with microcontact printing. Reproduced (adapted) with permission from [42]. Copyright ©Yamamoto *et al.* On the bottom, A schematic representation of a neuron grown on a system of gold nanopillars, coated with a specific adhesion-promoting molecule, PDLO. Reproduced (adapted) with permission from [43]. Copyright ©. 2018 American Chemical Society

biocompatibility is a necessary requirement, but not sufficient to guarantee neural cell adhesion and the emergence of the electrical behavior typical of neural networks [55]. For relevant *in vitro* studies of brain networks, cells should acquire the closest phenotype to that observed *in vivo*, and this is often not the case when cells are grown on flat and rigid substrates.

The *in vivo* environment of brain cells, called extra-cellular matrix (ECM), is a set of intricate guidance cues including diffusible factors, substrate bound molecules and physical cues like rigidity and nanoscale topography [56]. It has recently been demonstrated that the latter is of critical importance for the maintenance and regulation of neuronal function [36]. A crucial aspect in the replication of *in vitro* neural networks is the understanding of the precise mechanisms of interaction between a neural cell and the artificial substrate on which it adheres. Neurite/axon outgrowth, synaptogenesis and

network maturation are fostered by complex mechanotransductive processes and signaling which is triggered by the neuronal interaction with appropriate nanotopographic surface features [36]. It is thus very important to be able to provide controlled patterned substrates for restricted cell adhesion with features that recapitulate also the biophysical and structural complexity of the ECM.

During the last ten years at the Interdisciplinary Centre for Nanostructured Materials and Interfaces (CIMaINa), where this thesis was carried out, an additive method to fabricate surfaces to study quantitatively the effect of nanoscale topography on biological entities has been developed [57]. Zirconia (ZrO_x, substechiometric zirconium oxide [58]) nanostructured surfaces have been used to develop and assess a method able to explore the parameter space of topographic cues. This was done with the rapid and parallel fabrication of surfaces with different nanoscale topographies and subsequent assaying of the biological activity of cells exposed to the different conditions (at different scales from nano to micro and with high-throughput methods) [59].

The fabrication method is based on the use of supersonic cluster beam deposition (SCBD), that consists in the assembling on a substrate of neutral clusters produced by condensation in the gas phase and accelerated by a supersonic expansion. This approach produces nanostructured films with a nanoscale topography whose roughness can be accurately controlled and varied in a reproducible manner [57]. The extremely precise control over nanoscale topography can be easily obtained over macroscopic areas as required for the large number of experiments typical of *in vitro* biological assays [59]. Nanostructured ZrO_x surfaces produced by SCBD have a nanoscale topography that resembles that of the ECM and this promotes neuronal differentiation by mechanotransductive processes and signaling [60]. Moreover, primary neuronal cells can be cultured on these substrates where they display an accelerated maturation and build-up of a functional network of neurons and synapses [55]. Therefore, cluster assembled ZrO_x films are a viable and promising material for cell culture, which mimic important physical features of the ECM and ensure physiological development of cells.

SCBD can be employed to fabricate micropatterns of cluster assembled films, by using stencil masks. The geometric partitioning of zones can be obtained by depositing nanostructured zirconia micropatterns on glass substrates previously functionalized with an antifouling cell-repellent surface treatment. The possibility of confining neuronal cells on simple micropatterns with a defined nanoscale topography fabricated by SCBD has been previously demonstrated [61]. Micropatterns have been tested on a neuronal-like cell line (PC12) and on primary hippocampal neurons showing that, both types of cells grew, moved and differentiated on the adhesive nanostructured zirconia areas and scarcely overcame the boundaries between adhesive and cell-repellent territo-

ries. This can be considered the starting point for the fabrication of multi-scale substrates with controlled micro- and nanostructure to support the growth of brain cell networks while studying the properties of the biotic-abiotic interface in the cell development.

0.2 Thesis outline

In this thesis, nanostructured substrates with complex micropatterns were fabricated and used to replicate networks of glial cells, specifically astrocytes, *in vitro*. The goal was to characterize the combined effect of the nanoscale topography and cell confinement on astrocytic ensembles. Also, cell patterning allowed the reproduction of simple networks with shapes that are anatomically relevant. Such systems could leverage several interesting applications, which we started to explore in this work e.g., they could be used to elucidate some aspects of the involvement of astrocytes in information processing in the brain or contribute to the development of experimental platforms for studies of astrocytes in disease and brain dysfunction.

This thesis is organized as follows.

In Chapter 1, the motivation for research in nanomaterials applied to cell biology is explained. The biological aspects of biotic/abiotic interactions (in particular mechanotransduction) are briefly described and a few examples of applications are discussed. The second part of the chapter sets the foundation for the work developed in this thesis. It is devoted to the analysis of the previously characterized surface features of nanostructured zirconia films which make them an interesting tool for obtaining neuronal cells *in vitro* that differentiate and function like in their physiological environment.

Chapter 2 provides the biological framework for the cell model chosen for the investigations carried out in this thesis. Starting from a general description of astrocytic morphology and behavior in the physiological and pathological context, the relevance of this cell type in today's research is discussed. In fact, the role of astrocytes has recently been revised, with several experiments hinting at their active participation in information processing in the brain. The concepts of tripartite synapse and the known mechanisms for calcium signaling are delineated, while highlighting the questions that are still open. Also, a brief overview on the use of biomaterials for the culture of astrocytes in research is presented.

In Chapter 3 the details of the fabrication techniques and of the experimental methods employed in the thesis are presented.

Chapter 4 is dedicated to the technical description of the method for the fabrication of nanostructured micropatterned films. A large part of this work was devoted to the development of a robust strategy to obtain reproducible patterns with a resolution ≤ 20 µm, while ensuring tunable surface nanoscale topographic properties. The advantages

and the limitations of the technique are critically analyzed, and practical solutions are proposed to obtain viable results. Also, as astrocytes are able to grow elongated processes and are a highly adaptable and adhesive cell type, a stable protocol to obtain cell confinement is drawn up.

Chapter 5 reports the analysis of the impact of the nanostructure on astrocytic behavior and development. Cluster-assembled zirconia films are shown to induce an *in vivo*-like phenotype in astrocytes, typically not observed on standard cell-culture substrates. Surface roughness at the nanoscale is demonstrated to have reproducible effects on proliferation, morphology, actin cytoskeleton organization and calcium propagation.

In Chapter 6, stable confinement of astrocytes is demonstrated on nanostructure micrometric patterns. The effect of restrictive adhesion is identified in several properties both at the single cell and network levels. Astrocytic ensembles are shown to adopt the shape of the underlying micropattern, with visible impact on the actin filaments cytoskeletal organization. An analysis of the propagation of calcium waves reveals a possible influence of the geometric organization of cell on calcium waves events.

In Chapter 7 the conclusions emerging from this work and the future perspectives are discussed.

CHAPTER 1

Nanomaterials for cell culture

For years and until today, researchers have used standard cell-culture substrates made of flat and hard plasma-treated plastic or glass for a plethora of experimental studies *in vitro*. This approach has been very rewarding in cell biology and it has indeed provided a wealth of information. However, the morphological and mechanical properties of the substrates hardly resemble the physiological environment that cells experience *in vivo* [62], i.e. the neighboring cells and the ECM.

The ECM is the non-cellular component of all tissues that constitutes the physical microenvironment surrounding cells. It is apt at transmitting external forces on the cells, which, in turn, can also apply forces on the microenvironment [63].

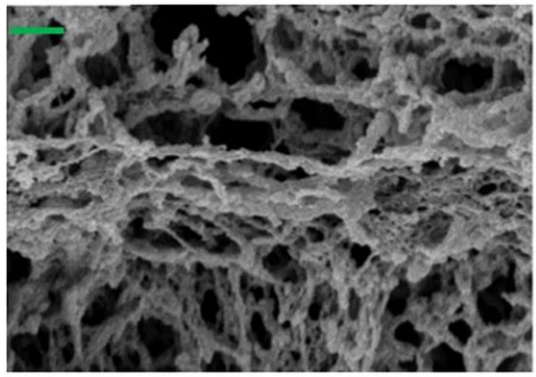

Figure 1.1: Surface scanning electron micrographs of the hippocampal extracellular matrix showing a highly porous and nanostructure topography at the nanoscale (the scale bar is 400 nm). Image adapted from [64]. Copyright ©2018 Tajerian *et al.*

The characteristics of the ECM vary depending on the specific type of tissue, but some transversal structural features can be identified. In fact, the ECM is a combination of cell-secreted nanoscopic components, like proteins and polysaccharides (e.g. glycosaminoglycan, collagen, laminin, elastin, and fibronectin), that self-assemble into a

complex structure of fibrils, fibers, pores, and asperities with spatial organizations and characteristic dimensions of a few to hundreds of nanometers [62, 65–67], see Fig. 1.1. The building blocks of the ECM are comparable in every tissue, but their spatial organization, arrangement, and size of the fibrous networks vary depending on their physiological function [62]. Also, the mechanical properties change accordingly and there is a great variability [68], e.g. the stiffest tissues, like bone, have an elastic modulus $\geq 10^9$ Pa, whereas the softest are lung and brain with and elastic modulus $\leq 4 \times 10^2$ Pa.

In the last couple of decades, the importance of these biophysical ECM cues for the regulation of cell functioning and fate via mechanotransductive processes (see Fig. 1.2) was increasingly disclosed. In this chapter, the principal mechanisms of cellular mechanosensing and mechanotransduction will be outlined. Also, the most widespread nanoengineering approaches that attempt at providing substrates with the morphological cues mimicking those encountered by cells *in vivo* will be presented. In the second part of the chapter, the focus will be on the properties of nanostructured zirconia, the biomaterial used in this thesis, and its applications in biology.

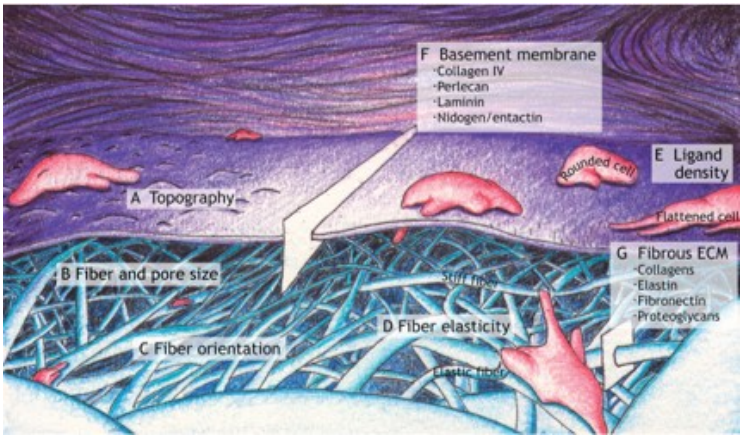

Figure 1.2: Examples of the morphological cues of the extracellular matrix. (A) Topography. (B) Varying fiber diameters and sizes of pores between ECM fibers. (C) Differences in fibers orientation, oriented and non-oriented fibers. (D) Fibers elasticity. (E) Differences in ligand density affecting cells shape. (F-G) Different types of ECMs, basement membrane and fibrous ECM. Image adapted from [69]. Copyright ©2021 The Company of Biologists.

1.0.1 Interaction between cells and microenvironment

The idea that cell development and functioning is governed by biochemical factors alone has been overcome. In living systems, cells are constantly exposed to a variety of biochemical but also biophysical cues provided by the surrounding microenvironment [70]. These biophysical cues can be sensed with receptors in the cell membrane that are often enriched in exploratory protrusive structures that translate the microenvironmental

information into appropriate cellular responses [71].

Cells perceive biophysical stimuli and convert them into a modulation of their physiological response, which, in turn, affects their phenotype [70, 72]. Forces play an essential role for the interaction between cells and ECM. They can be propagated to different cellular organelles and the nucleus, thus resulting in altered gene expression and cell functioning [73]. This process, called mechanotransduction, has several repercussions in a range of biological processes, such as migration, proliferation, differentiation, embryogenesis, and tissue homeostasis and repair [74].

The major components that initiate mechanotransduction are integrin adhesion complexes (IAC), which function as relay station of the signals between the cellular outside and inside by modulating the cytoskeletal organization [61]. IAC are composed of integrins, transmembrane proteins that have distinct binding specificities to ligands present in the components of the ECM. These features allow them to perceive the information from the extracellular domain and transfer it to the cell [75, 76]. Integrins undergo an "activation" process that consists in a conformational change between a low and high ligand affinity state, respectively characterized by an inactive closed-bent or active open-extended form (and several intermediate states). Integrin activation can either be induced and/or stabilized by integrin ligand binding itself (outside-in signaling), by intracellular events (inside-out signaling) [77, 78], or by modulation of the membrane tension [79–81]. Regardless of the nature of the activation, the integrins are then linked via adaptor proteins (such as talin and vinculin) to the filaments of the actin cytoskeleton, engaging in the so-called molecular clutch, which links the forces generated through actin polymerization and actomyosin contraction (resulting in a retrograde actin flow) to the integrins [82]. The fate of the initial adhesion structure depends on the level of force loading within the molecular clutch. At sufficient force loading the integrins are maintained in their activated conformation and their ECM/ligand binding is strengthened [83]. This force-dependent mechanism allows the extension of talin, the recruitment of further IAC components and thus the maturation of the IAC, potentially up to the generation of focal adhesions (FAs), i.e. stable adhesion sites. The IAC composition is highly dynamic and very complex, potentially comprising more than 200 different protein constituents [84–86]. Alterations in the IAC composition modulate cellular signaling and can induce a remodeling of the cytoskeleton. This complex signal propagation eventually reaches the nucleus, since the chromatin therein is connected to the cytoskeleton by the Linker of Nucleoskeleton and Cytoskeleton complex (LINC complex) [72, 77, 81, 84] which can induce mechanical hotspots for genome regulation [88]. Altogether, these mechanotransductive processes mediate the impact on cellular behavior and fate. Although many details remain still elusive, these processes were found to be strongly in-

volved in virtually all cell biological processes, in particular, in cell differentiation and migration. It is important to highlight that the regime of force transmission and force loading within the molecular clutches are regulated by the mechanisms by which the cells pull on the ECM through contraction of the actomyosin cytoskeleton. Therefore, the complex dynamics of cell–matrix bond formation and rupture is essentially governed by the different mechanical and structural factors of the microenvironment. Substrate rigidity and the spatial distribution of integrin ligands together regulate therefore force transmission and force loading and subsequently the cell behavior [81, 89–92].

The cartoon in Fig 1.3 recapitulates the changes that a cell undergoes when plated on a substrate with mechanical/morphological properties that favor loose (A) or strong (B) cell adhesion.

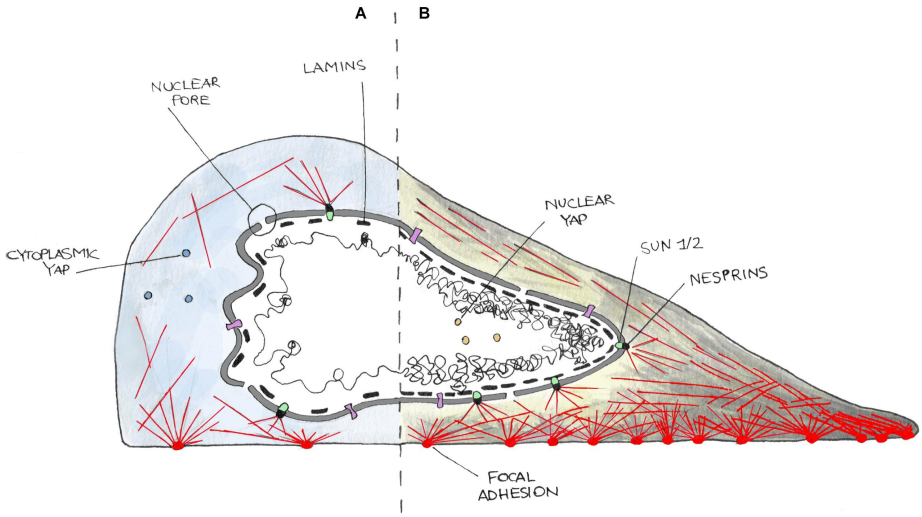

Figure 1.3: Cartoon representing the extracellular matrix–cytoskeleton–nucleus connections in a cell weakly adherent (A) and highly adherent (B) to the substrate, with associated modulations in the nuclear features. In (A), the cell develops few and small focal adhesion and thin stress fibers (red lines). In (B), the cell forms more and bigger focal adhesion as well as thick stress fibers. This leads to nuclear invagination disappearance and nuclear translocation of YAP and a reorganization of the chromatin (black line). Adapted and reproduced with permission from Ref.[73]. Copyright ©2021 Pennacchio *et al*.

In the first case, the cell develops few focal adhesions and thin stress fibers. On the other hand, in the high-adhesion scenario, there is a higher internal tension caused by the larger quantity of focal adhesions and thick stress fibers. These differences in the cytoskeleton are translated in variations of the conformation of the nuclear envelope and of the chromatin (depicted as a black, twisted line in the figure). Moreover, highly adherent cells display an increased nuclear content of the yes-associated protein (YAP), that functions as a transcriptional regulator [91] and has a major role in cancer [93], tissue

shape [94] e and organ size control [95].

1.1 Fabrication of biomimetic substrates

The requirement to study cell behavior in a more realistic *in vivo*–like environment and the pursuit to control cell behavior by appropriate substrates prompted material scientists to develop a new generation of cell-culture substrate materials that mimic the physiological, structural and biophysical environment of cells. In this context, biomaterials with modifiable mechanical properties [62, 96–99] or substrates with nanotopographic features [71, 100, 101] have become increasingly interesting for research and biomedical applications based on tissue engineering, due to their potential in providing a reproducible control over cellular functions and behavior.

To mimic the biomechanical properties of the ECM, a range of materials with different stiffness have been developed. The most common are based on different types of hydrogels, naturally derived (e.g. collagen, fibrin), synthetic (e.g. polyacrylamide, polyethylene glycol) or hybrid materials that combine elements of synthetic and natural polymers (e.g. hyaluronic acid, polypeptides) [96]. Other strategies include the use of silicones, like PDMS, with tunable elastic modulus [102, 103]. Direct effects of substrate stiffness were observed on cell differentiation [104], as well as cell shape and motility [105]. Gels that are moderately stiff like muscle have been found to optimize myogenesis [104], and gels that are firm, like precalcified bone, optimize osteogenesis in 2D and 3D [104, 106, 107]. Moreover, when stem cells interact with substrates that possess brain-like rigidity, neuronal viability is favored [108] and cell differentiation is biased towards the neuronal phenotype [36, 109, 110].

On the other hand, nanotopographic signals have been shown to instruct the behavior of stem cells. Direct effects were registered in e.g. the regulation of cells shape [111–113], cytoskeletal tension [72, 114], integrin mediated adhesion signaling [115] and nuclear mechanics [116, 117]. Also, the impact of micro- and nanotopographic features has been widely demonstrated on neuronal cell behavior, e.g. in neurite and axon outgrowth, gene expression and differentiation [118–121]. The nanotopographic features of the ECM were reproduced developing surfaces or scaffolds for *in vitro* cell research with various nanoengineering techniques and synthesis methods. The most widespread fabrication methods include either top-down approaches, like lithographic patterning and pattern transfer, or bottom-up techniques, based on surface roughening and material synthesis. Fig. 1.4 reports several examples of nanostructured surfaces obtained with a variety of techniques. A complete review providing a several examples of synthetic nanotopographic surfaces, with a discussion on the advantages and drawbacks of each technique can be found in Chen *et al.* [71].

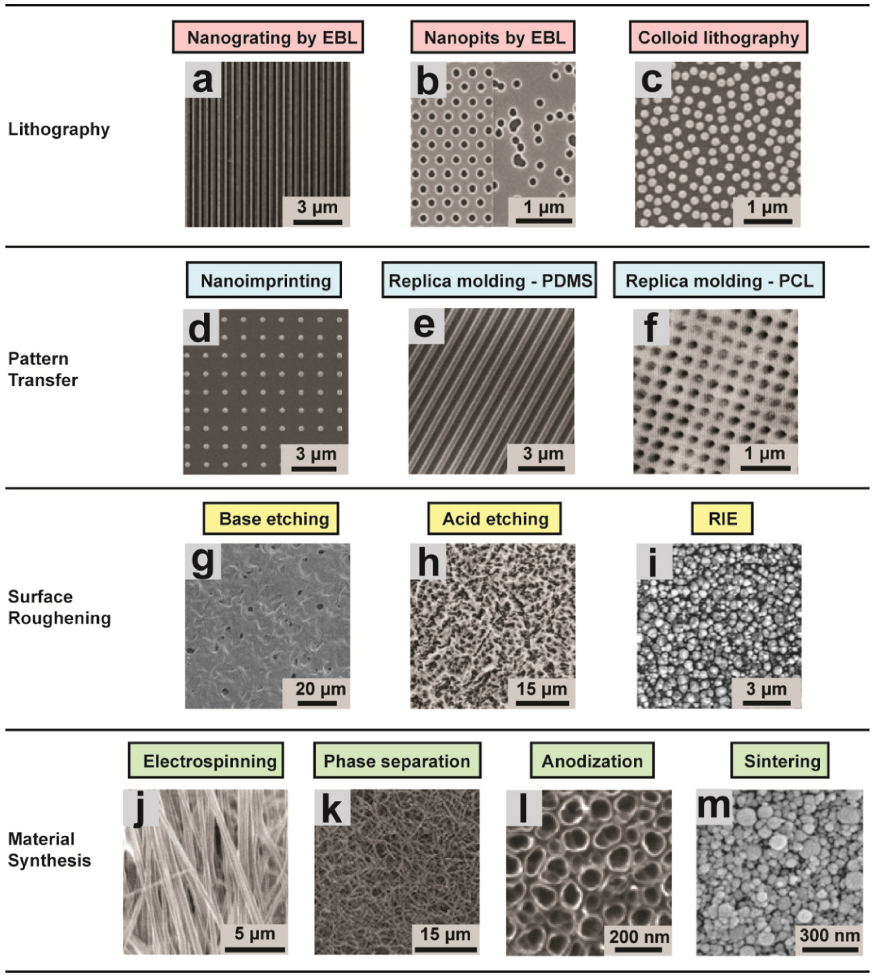

Figure 1.4: Fabrication of nanotopographic surfaces. Reproduced with permission from Ref. [71]. Copyright ©2014 Elsevier Ltd. Lithography for patterning: (a) Nanogrooved silicon substrates with 70 nm wide ridge and 400 nm pitch (e-beam lithography) [110]. Copyright ©2003 Biologists Ltd. (b) Regular (left) and random (right) arrays nanopits (diameter 120 nm, depth 100 nm) on silicon substrates (e-beam lithography) [122]. Copyright ©2007, Nature Publishing Group. (c) Self-assembly nanoparticles (diameter of 110 nm) [123]. Copyright ©2003 IEEE. Pattern transfer: (d) Nanostructured polyurethane acrylate with a patterned array of nanopillars, diameter 300 nm, spacing 900 nm (nanoimprinting) [120]. Copyright ©2013, American Chemical Society (e) PDMS nanograting (replica molding) [124]. Copyright ©2005 Elsevier Ltd. All rights reserved. (f) Polycaprolactone surface with nanopits (replica molding) [125]. Copyright ©2002 IEEE Surface roughening: (g) Nanostructured PCL with feature dimensions of 50 – 100 nm (NaOH etching) [126]. Copyright ©2003 Wiley Periodicals, Inc (h) Nanoroughened Ti surface (surface roughness < 1 µm) (acid etching) [127]. Copyright ©1998 John Wiley & Sons, Inc. (i) Glass surfaces with surface roughness of 100 nm (reactive ion etching) [128]. Copyright ©2012, American Chemical Society Material synthesis: (j) Aligned nanofibrous hydroxybutyl chitosan (electrospinning) [129]. Copyright ©2007 WILEY-VCH Verlag GmbH & Co. KGaA, Weinheim (k) Nanofibrous PLLA matrix, average fiber diameter of $\sim$ 148 nm (phase separation) [130]. Copyright ©2009, Mary Ann Liebert, Inc. (l) Self-aligned TiO_2 nanotubes, diameter 100 nm (Ti sheets anodization at 20 V) [131]. Copyright ©2021 National Academy of Sciences (m) Nanostructured alumina with 24 nm grain-like structures (sintering) [132]. Copyright ©2008 Wiley Periodicals, Inc. All the figures are reproduced with permission from the indicated references.

In most cases, these techniques were originally developed for different purposes, like the manufacturing of micro-mechanical systems, and they have been adapted to this cell culture application. Often, this introduces technical limitations hampering the translation to the necessities of cell biology. In particular, biological experiments require a large number of replicates of the same sample, so the fabrication issues mainly concern scale-up capacities, cost-efficiency, and/or ability to control and tune finely the nanometric feature size and dimensionality [59].

In this framework, SCBD [133] represents a technology with the potential to fabricate, at a large scale, nanostructured surfaces with controlled morphological properties at the nano- and mesoscale, mimicking the nanotopographic features of extracellular matrices [60]. This bottom-up approach produces nanogranular films by randomly stacking clusters that create a nanoscale topography that can be accurately controlled and varied in a reproducible manner [134].

In the last decades, at CIMaINa, where this thesis was carried out, SCBD (see Chapter 3.1.1) was exploited to fabricate nanostructured thin films based on zirconia, a biocompatible material suitable for cell-culture and biological analysis [135]. They have been used in a variety of experimental studies [55, 59–61, 135–137] where nanostructured zirconia has been applied to provide cellular microenvironments with controllable and reproducible biomimetic nanotopographies to unravel the impact of nanotopographic features on the mechanisms underlying mechanotransduction and to guide and control cellular behavior. The focus was directed on neuronal cells, that have been demonstrated to be affected by mechanotransductive processes during neurogenesis, neuronal migration, differentiation, and maturation [82]. In the following sections, a description of the main structural and morphological properties at the nanostructure that make zirconia a suitable biomaterial for cell growth will be reported. Then, the most recent and relevant studies concerning nanostructured zirconia films in the context of biology and mechanotransduction will be discussed. These, in fact, constitute the basis of this thesis.

1.2 Nanostructured Zirconia assembled by Supersonic Cluster Beam Deposition

1.2.1 Structural and morphological properties of the films

With SCBD (the technique is described in section 3.1.1), nanocrystalline building blocks are assembled on a substrate. When they are deposited, the clusters maintain their individuality and do not undergo fragmentation [138]. The result is a granular, porous film, with a high number of defects (e.g. grain boundaries and grain-grain junctions) and a large volume fraction [139, 140]. See, for example, the scanning electron mi-

croscopy (SEM) images of the surface of a nanostructured ZrO_x film reported in Fig. 1.5 (a) and (b). The image in (c), instead, is the lateral view of the same film, from which we can appreciate the typical rough profile resulting from the random stacking of clusters.

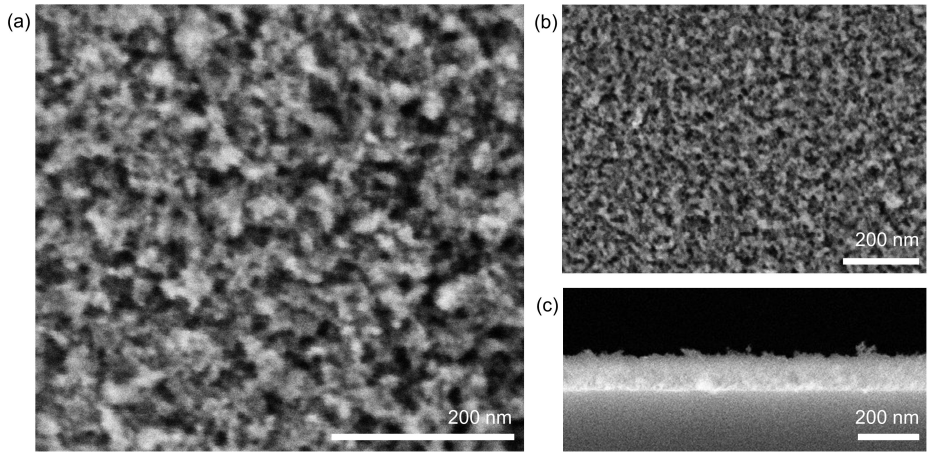

Figure 1.5: SEM images of a nanostructured zirconia thin film with a RMS roughness of 10 nm, deposited on a silicon substrate. (a,b) top view of the same film at different magnifications. The highly porous, cluster assembled surface is clearly visible. (c) Lateral view of the film. The film has a thickness of $\sim$ 130 nm and is characterized by a rough surface profile at the nanoscale. The images were acquired with a SEM model Zeiss Supra 40, operated at 5-7 kV accelerating voltage.

ZrO_x films, deposited with argon as gas carrier (see section 3.1.1) are composed of crystalline clusters in the cubic phase with an average diameter of 6.0 $\pm$ 1.7 nm and [58]. The chemical composition of as deposited zirconia clusters, as revealed by a XPS analysis, is that of sub-stechiometric zirconium oxide, i.e. ZrO_x, with x = 1.9 [58]. The interface properties of ZrO_x films fabricated with SCBD can be finely tuned and reproduced [134]. In fact, the assembling of clusters with a well-defined and stable mass distribution produces films with a surface morphology that evolves according to simple scaling laws, known as the Family-Vicsek scaling relations, which describe a variety of growing interfaces [141–143]. A parameter that describes the average nanoscopic features of a cluster assembled film is the roughness R of the surface. Given a topographic map of a film, R is defined as the standard deviation of the film heights. Fig. 1.6 shows the surface profile $h(x)$ of a nanostructured film with the average height h_0 and the parameter R highlighted.

All the deposited clusters contribute to the growth of the film thickness and the roughness. In a ballistic deposition regime, where clusters stick upon landing [141, 143], the film roughness scales with the film thickness h (as long as the deposition rate is constant, so $h \sim$ time) according to the following law

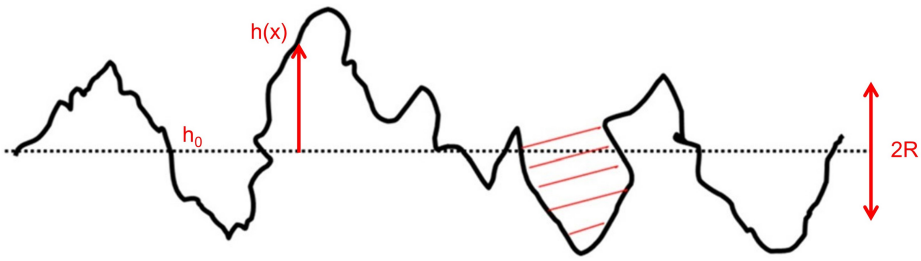

Figure 1.6: Schematic representation of a topographic one-dimensional profile $h(x)$ of a cluster assembled film, with relevant geometrical properties highlighted: the surface roughness R and the mean height h_0. A surface pore is shaded in red. Adapted and reproduced with permission [134]. Copyright ©2015 AIP Publishing LLC.

$$R \sim h^{\beta} \tag{1.1}$$

where the scaling exponent β can be extracted experimentally [134]. In the case of Zr clusters with Ar as gas carrier, $\beta = (0.37 \pm 0.05)$ nm [57]. Therefore, the knowledge of the parameters of the function relating the film roughness to its thickness enables the fabrication of nanostructured films with very reproducible surface morphologies. Similar scaling laws apply to the evolution of specific area as well as the correlation length, that is the lateral dimension of the largest morphological features [134]. Compatible values of surface roughness, specific area and correlation length can be obtained over large, macroscopic areas (up to hundreds of cm^2) and a high number of samples.

1.2.2 Nanostructured zirconia as biomaterial for cell culture

Among the possible materials that can be used as substrates for the study of the interactions with cells, zirconia is particularly attractive as it is already widely used in implantology (in particular, dentistry and orthopedics) for its favorable biocompatible characteristics [144, 145].

Furthermore, nanostructured ZrO_x substrates were shown to possess structural and functional properties highly significant for interactions at the biotic/abiotic interface [55, 60, 61, 135, 136, 146, 147]. Note that ZrO_x substrates can be used for cell culture as deposited, with no further functionalization before cell seeding, for example with poly-L-ornithine and matrigel, [61]. Nanostructured zirconia films produced by SCBD are interesting for their morphology. They display nanotopographic features that resemble those observed *in vivo* in the ECM, moreover the randomly distributed nanoscopic asperities on the surface have been shown to modulate integrin-dependent mechanotransductive processes and signaling [59, 60, 148]. In Fig. 1.7 the topographic map of a native ECM is

compared with the topographic map of a nanostructured zirconia film with roughness 25 nm. The maps have comparable lateral dimensions and both display a complex and disordered structure at the nanoscale, characterized by peaks and valleys.

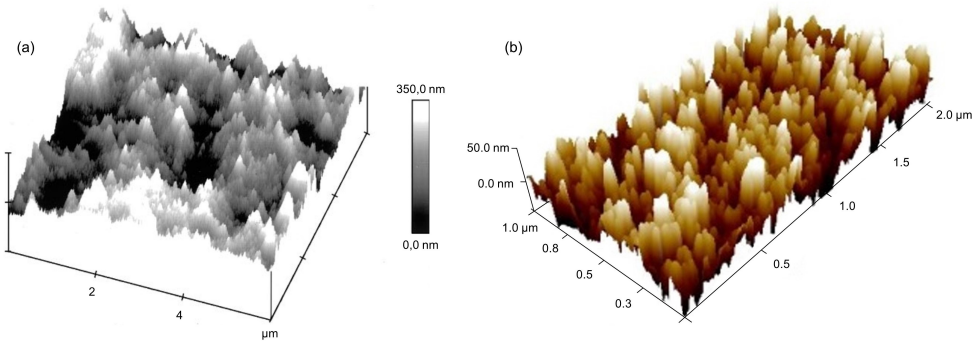

Figure 1.7: Comparison between atomic force microscope (AFM) topographic maps of an ECM and a nanostructured zirconia film. (a) An example of a native ECM, the basement membrane of a rhesus macaque corneal epithelium. Reproduced (adapted) with permission [56]. Copyright ©1999, Springer-Verlag. (b) Cluster-assembled zirconia film with a RMS roughness of 25 nm. Reproduced (adapted) with permission [60]. Copyright ©2016, Schulte *et al.*

From the chemical point of view, cluster-assembled ZrO_x films have a lower isoelectric point than flat surfaces, due to perturbations of the electrostatic interfacial double layer determined by the peculiar geometry of the interface [149]. This may impact on the surface adsorption properties, which is relevant in the scenario of biological environments where the proteins from the culture medium and those secreted by cells mediate the interaction between biomaterial and cells [135]. Indeed, rough surfaces were shown to be more efficient in adsorbing proteins than flat surfaces, beyond what could be expected by the increased specific area [135].

Initial studies with various cell types from diverse biological backgrounds confirmed that cell lines (MG-63 [147], immortalized fibroblasts [145]) and primary cells (human melanocytes [145], human myogenic CD133 progenitors [150], rat microglia [151]) are able to adhere and grow on nanostructured surfaces produced with SCBD.

Moreover, an ultrastructural analysis of the interface between cells and nanostructured zirconia films [60] demonstrated that the asperities have dimensions with the potential to influence integrin mediated adhesion. In fact, for PC12 cells (a neuron-like cell line) the cells-surface interactions were found to be restricted to the apical part of the asperities of surfaces with a roughness of 15 nm. The corresponding adhesion sites at the nanoscale have a width of (53.2 ± 48.0) nm in average, compared to (90.2 ± 93.2) nm on flat zirconia surfaces. This dimension is in the range of integrin clusters, the modular units of cell adhesion sites (50-100 nm) that assemble in focal adhesions[152]. Also the

distance between these integrin adhesion sites on the nanostructured substrate (average: 99.1 $\pm$ 101.4 nm, median: 60.4 $\pm$ 33.4 nm) oscillates around the threshold values shown in literature to be critical for the formation of focal adhesions ($\sim$ 60-70 nm) [77, 92, 101, 148]. This is relevant because the focal adhesions that are formed during cell spreading constitute the cytoskeletal organizing centers [148], dictating the biomechanical properties of the cell [77, 81] and ultimately the cellular functioning and fate.

1.2.3 Effects of nanostructured zirconia on neuronal cell mechanotransduction and behavior

Albeit many details remain elusive, it is evident that the ECM configuration and integrin-mediated mechanotransduction participate in the control of neuronal cell differentiation ad maturation. This requires coordinated and dynamic cytoskeletal actions and cell/microenvironment interactions [36] [153–155]. Also, mature neurons with an axon, several dendrites and synapses, maintain a remarkable plasticity to enable the processing of incoming information. This plasticity is highly dependent on integrin-mediated interaction with the microenvironment [154, 155].

In this context, the identification of biomaterials able to control neuronal differentiation and maturation by mechanotransductive processes [82] is interesting e.g., for the fabrication of neural circuits or interfaces [36, 156, 157], for the reproduction of *in vitro* neurodegenerative disease models [158] or for the regeneration of damaged neural tissue [159–161].

Fig. 1.8 summarizes the results regarding modulations along the mechanotransductive sequence on PC12 cultured on nanostructured films (i.e. cell-substrate interaction, cytoskeletal organization and biomechanical properties) crucial in determining the physiological properties of the cells [60]. Schulte *et al.* in [60], demonstrated a significant potential of nanostructured cluster-assembled substrates in influencing essential cellular functions in particular by inducing neuronal differentiation processes in PC12 cells. The cell/nanotopography interaction was reported to affect the focal adhesion formation and the cytoskeletal organization, which thereby modulate the general biomechanical properties by decreasing the rigidity of the cell. These alterations were found to modify the activation dynamics of transcription factors relevant for neuronal differentiation (e.g. CREB). Furthermore, a detailed proteomic analysis revealed that nanostructure induced the differential expression of proteins that are known to be involved in mechanotransductive processes and that directly affect cellular activities [36, 100, 162, 163].

Maffioli *et al.* [59] conducted an extensive proteomics of PC12 cells interacting with diverse nanotopographies. Many of the proteins found to be altered were associated with cell/substrate interaction, cellular mechanics, nuclear organization and transcrip-

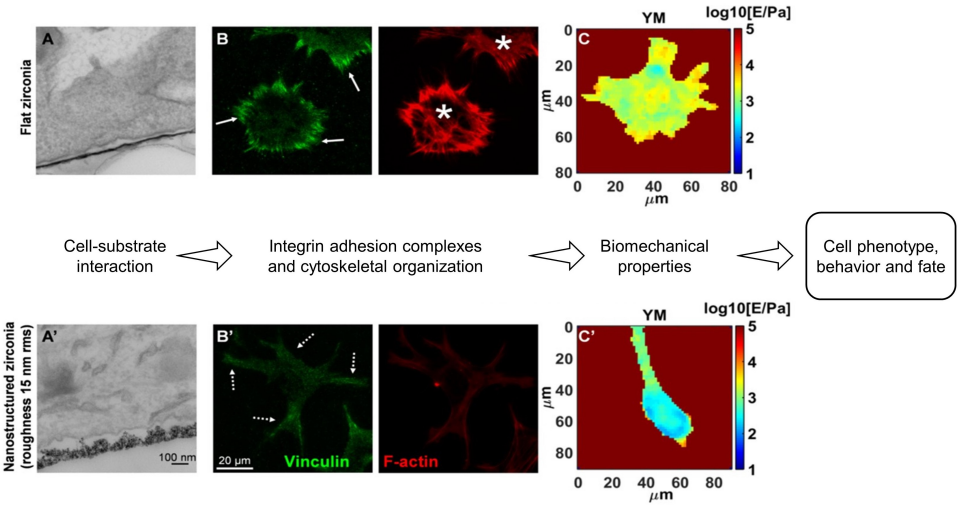

Figure 1.8: Mechanotransductive response to cluster-assembled nanostructured materials. (A, A') TEM images demonstrate the interface between PC12 cells and (A) flat zirconia or (A') nanostructured zirconia surfaces with 15 nm RMS roughness. Cells interact only with the upper part of the surface asperities. (B, B') The staining of vinculin in green (a crucial component of integrin adhesion complexes) recorded by TIRF microscopy shows (B) focal adhesion formation, highlighted with arrows, on flat zirconia, compared to smaller structures in (B') indicated by the dashed arrows on the nanostructured surface. On the right, the corresponding epifluorescence images of the actin cytoskeleton are reported in red. The asterisks indicate stress fibers on flat zirconia, which are absent on the nanostructured zirconia. (C, C') Young's modulus (YM) maps of the cells on (C) flat or (C') nanostructured zirconia. Cells are softer on the nanostructure. Altogether, the modulation of the nanoscopic features of the substrates determines the phenotype, behavior and fate of the cells, via a mechanotransductive process. Reproduced (adapted) from [135]. Copyright ©2017 American Chemical Society

tional regulation. In the context of mechanotransduction, these alterations revealed a complex nanotopography-sensitive network potentially important in the promotion of neuronal differentiation by nanotopographic cues.

In another work, Schulte *et al.* [55] used primary hippocampal neurons, a standard model to study neurogenesis and the functional synaptic network integration [164, 165], to evaluate the potential outcomes of nanotopographic features on the development of neuronal morphology, synaptogenesis, and network maturation. As Fig. 1.9 shows, they found that on substrates with the roughness of 25 nm RMS neurons exhibited a mature phenotype with an increase in neurite outgrowth already after 3 days *in vitro* (DIV), compared to flat substrate conditions. Also, a large fraction of neurons was found to be excitable at 7 DIV and the presence of spontaneous synaptic currents (with frequency significantly higher with respect to the control) indicated that active synapses were fully formed, which was not the case for the flat substrates. In the canonical culture condi-

tions, the formation of a mature synaptic network with excitable cells usually requires 1–2 weeks [166, 167]. In the same work, the proteomic data confirmed a fundamental

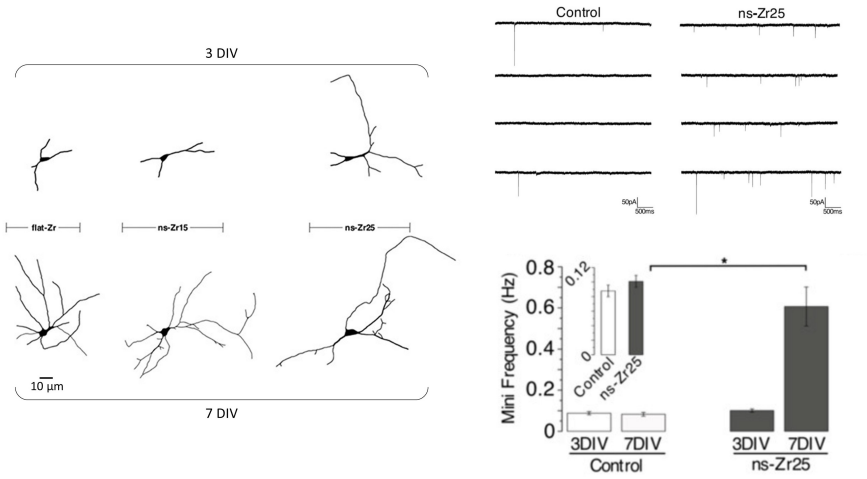

Figure 1.9: On the left, representative examples of morphology of neurons plated on flat and nanostructured substrates. In the case of substrates with 25 nm roughness, neurons display a more pronounced mature neuronal phenotype already after 3 DIV and with axons specification after 7 DIVs. The graphs on the top-right show exemplary miniature current traces recorded from neurons plated on control or nanostructured surfaces after 3 DIV. The corresponding mean frequency is reported in the bar graphs on the bottom-right. At 3 DIV no significant difference between control (white bars) and nanostructured substrates (gray bars) is highlighted, even if a trend (see the inset) of an increased frequency in the nanostructured films condition emerges. This tendency stands out at 7 DIV, where there is significant increase in frequency in neurons grown on the nanostructure. Reproduced (adapted) with permission from [55]. Copyright ©2016 Schulte *et al.*

change of the cellular program in the hippocampal neurons after 3 days in contact with nanorough surfaces, with an upregulation of markers typical of developing neurons and neurite/axon outgrowth. Consistently, also proteins involved in integrin adhesion complexes and the cytoskeletal organization were found to be differentially expressed, confirming an involvement of the mechanotransductive machinery.

Altogether, the last ten years of research at CIMaINa demonstrate multiple impacts along the whole mechanotransductive sequence and on differentiative processes of neuronal cells that can be induced by nanotopographic cues. These works highlighted the potential of cluster-assembled nanotopographic films as materials for brain cell biological studies. The applications of these nanostructured materials are manifold and versatile, e.g. in future they could be used as platforms with differentiation-promotive properties for cell culture, tissue engineering, organ-on-a-chip approaches or for drug testing.

1.2.4 Micropatterned nanostructured zirconia

With simple hardware modifications, SCBD can be adapted to produce nanostructured zirconia films with micropatterned features. Lateral dimensions down to tens of micrometers can be achieved, as it was demonstrated by previous works exploiting stencil masks carried out at CIMaINa [168, 169].

This technology has interesting potential applications in biology, and in particular in neurobiology. Stencil-assisted SCBD combined with methods for surface modification, based for example on chemical functionalization processes, opens the possibility to fabricate substrates that can restrict the adhesion of cells to defined spatial locations determined in advance.

Spatial control over cell network geometry and topology, with micrometric resolution, has been applied to different research fields, e.g. drug testing experiments [170, 171], in fundamental studies covering various biological areas [172, 173], or in the fabrication of cell-based biosensors for the functional characterization and detection of drugs, pathogens, toxicants, and odorants [174]. Also, cell patterning enables the control of the geometrical shape of the culture, thus the reproduction of specific anatomical structures or the conditions encountered in certain tissues. For example, different nanofabrication techniques have been employed to produce fibers with the same length and diameter of axons [175]. These artificial structures were used in interaction with glial cells to study the process of myelination [176].

Another major field of application is the replication of simplified networks of neural cells *in vitro*. As discussed in the introduction (section 0.1.1), the scientific community has still an incomplete understanding of how interconnected elementary circuits of cells ultimately forming the connectome, are at the basis of the emergent complex computational abilities of the brain. A strategy to answer some questions related to this topic is to adopt a bottom-up approach and start with the characterization of simple networks *in vitro*, moving onto more complex structures step by step. The construction of brain circuitry *in vitro* can be used to study basic mechanisms of information processing in the brain [177, 178]. To reach this goal, it is necessary to achieve a spatial control over the adhesion of individual living neurons on predefined substrate areas and make them follow specific connectivity designs, in conditions where the number and subtypes of brain cells and their connectivity patterns are precisely determined a priori, see for example [9, 179, 180].

In this context, at CIMaINa, Schulte *et al.* developed substrates allowing to restrict cell adhesion over controlled portions of the surfaces, while the cells interface with a material whose morphological properties at the nanoscale resemble those of the ECM [61]. SCBD was here applied to pattern micro-dots of nanostructure zirconia on glass sub-

strates previously functionalized with an antifouling cell-repellent surface treatment. The substrates were tested with neuron-like PC12 cells and rat neonatal primary hippocampal neurons. With both cell types, a stable confinement of cell adhesion in the destined zones of the micropatterns was observed. In Fig. 1.10 illustrative images show PC12 cells on micrometric patterns. Electrophysiology and calcium imaging experiments provided evidence of the development of functional networks on the hippocampal neurons on the same patterned zirconia dot.

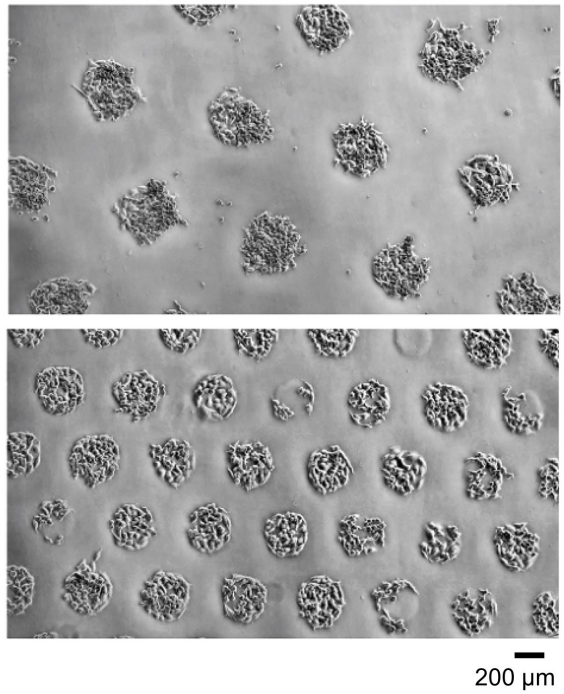

Figure 1.10: Representative phase contrast images of PC12 cells at 1 DIV on two different fabricated micropatterns, composed of dot of diameter 300 µm placed on a hexagonal matrix with interaxial distance of 500 µm (top) and 300 µm (bottom). Reproduced (adapted) with permission [61]. Copyright ©2018 American Chemical Society

This work was further expanded during my PhD. In fact, more complicated nanostructured zirconia patterns were fabricated by adding micro-bridges connecting the adhesive dots. The developments that will be presented here provide the essential elements that enable the reproduction of solid artificial cell networks *in vitro*, where a control of the connectivity can be achieved. The details can be found in Chapters 4 and 6.

CHAPTER 2

Astrocytes: an overview

Astrocytes are a type of brain cell found in the mammalian CNS. Contemporary literature suggests that they are able to perceive the mechanical cues of the microenvironment that surrounds them through mechanotransductive processes. Specifically, these cells adapt to the physiological or pathological context and have been demonstrated to play a significant role in tissue remodeling and pathogenesis [175]. Moreover, it has recently been suggested that astrocytes are active participants of the brain circuitry as they form astrocytic networks that contribute to the modulation of neural activity [181, 182]. Astrocytes should therefore be studied as organized cell networks and their interactions should be observed in a controlled environment.

In this work we chose astrocytes as cellular model because rather little is known about the influence of the microenvironmental nanotopographic cues and geometry on these cells and their functioning. The substrates developed in the framework of this thesis represent a valuable tool, as they provide both a morphologically authentic ECM-like substrate (Fig. 1.7), enabling the analysis of cellular responses (e.g., in terms of cellular morphology, cytoskeletal organization and calcium signaling), and the possibility to confine cells into patterns of simple astrocytic network with an anatomically relevant shape. From a technical point of view, these cells represent also an interesting challenge, as astrocytes are hard to confine because they adhere to most surfaces and are highly mobile cells [181].

This chapter will delineate both the main well-known features of astrocytes and the recent findings which made this cell type a hot topic in research. This will provide a solid biological framework for the results of this thesis.

In the second part of the chapter, I will give an overview of the current research on astrocytes using biomaterials as tools to investigate the interesting biological properties here presented.

2.1 Glial cells

Neurons and neuroglia are the two types of cells constituting the building blocks of the brain. In the last century, the universally accepted assumption was that neurons were responsible for all the major brain functions - encoding and processing information from external stimuli and generating behavior. This concept originated from the fact that neurons are electrically excitable and propagate complex current signals to other cells. Moreover, neurons form intricate networks where every cell can establish synaptic connections with up to thousands other neurons in the brain [4]. On the other hand, glial cells had been thought to fulfill a mere supportive role to neurons, providing a metabolic and physical substrate.

The concept of neuroglia was first introduced by Rudolph Virchow in 1856, who identified a connective tissue filling the interstices among the nerve cells in the brain [183]. The idea of glial cells as passive, ancillary elements remained virtually unquestioned for more than a century. Today, we know that glial cells are as abundant as neurons and take active part in almost every physiological and pathological function of the brain [184].

In the central nervous system of vertebrates, three types of glial cells can be distinguished, namely oligodendrocytes, microglia and astrocytes. Additionally, in the peripheral nervous system there are Schwann cells. Oligodendrocytes and Schwann cells form the myelin sheath that insulates the axons of neurons by enveloping it with their membranous processes, thereby, enabling a high conduction velocity within the axons [185]. Microglial cells are the immune system cells of the brain and are activated during injury, infection or degenerative diseases [186]. Astrocytes are by far the most studied among glial cells. Since the nineties, it has been established that astrocyte may exercise a strong modulatory influence over neuronal signaling [22, 24]. Astrocytes are the most abundant glial cell type and fulfill a plethora of different tasks such as providing guiding structures during development, controlling homeostasis of the extracellular space, providing an energy substrate for neurons, controlling blood flow and modulating synaptic transmission [4, 187]. Taken together, brain function is determined by the collaborative action of neurons and astroglia.

2.2 Astrocytes

With the discovery of several mechanisms by which astrocytes modulate neuronal synaptic activity, the understanding of the role of these cells and their consequences on brain function has changed. Astrocytic calcium signaling has been proposed to link neural information over different spatio-temporal domains, which might enable communication at a brain-wide level [188]. This new complexity raised many questions that still need to

be resolved [189].

In the following sections a short introduction will be reported of the main properties of astrocytes regarding structure, physiology and function. The current knowledge on this cell type will be presented, with a focus on the questions that are still open.

2.2.1 Structural and physiological properties of astrocytes

General morphology

Astrocytes are an extremely heterogeneous cell type. Variability is not only associated with different brain areas, but also to the same region. Differences among astrocytes involve morphology, development and physiology [190, 191]. The name *astrocyte* refers to the irregular shape of the roughly star-like cell bodies typical for this cell type. Astrocytes, *in vivo*, have a small soma (about $10\,\mu\mathrm{m}$ diameter) from which multiple fine processes create an intricate and extensive star-like arborization. We can identify two main classes of astrocytes: fibrous astrocytes of the white matter, and protoplasmic astrocytes of the grey matter. Protoplasmic astrocytes have a complex morphology with numerous fine processes, and are distributed uniformly within cortical gray matter. Fibrous astrocytes, instead, have a simpler shape with less filaments and are organized along white matter tracts, with a longitudinal orientation in the plane of the fiber bundles [192]. A schematic depiction of the typical shape of protoplasmic and fibrous astrocytes is reported in Fig. 2.1.

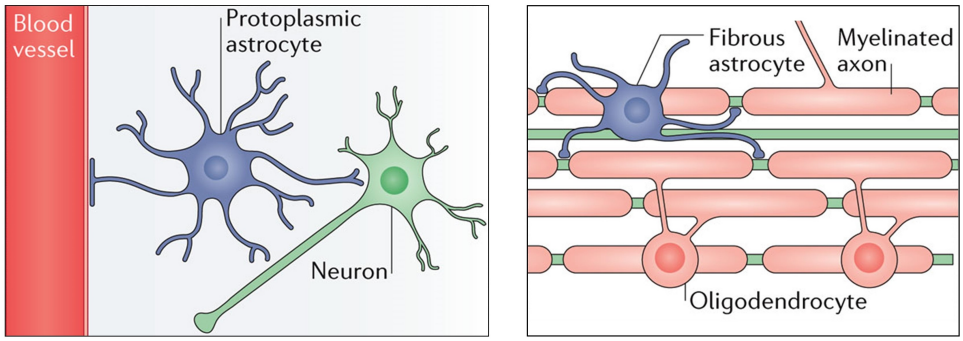

Figure 2.1: This scheme illustrates the morphology of protoplasmic and fibrous astrocytes. Protoplasmic astrocytes of the grey matter have a radial shape and contact neuronal synapse and blood vessels. Fibrous astrocytes in the white matter have a more elongated morphology and are in close contact with axon tracts. Adapted and reproduced with permission from Ref. [191]. Copyright ©2021 Springer Nature Limited.

In addition to these two classes, specialized astrocytes within different areas of the brain can also be identified: the Bergmann glia of the cerebellum, and the Muller glia of the retina. Nearly every astrocyte forms end-feet processes with at least one blood

vessel. Blood vessels influence the overall morphology of astrocytes, prompting some astrocytes to develop decidedly longitudinal forms, in an attempt to reach a vessel [193]. The fine processes of protoplasmic astrocytes penetrate all areas of the local neuropil, encompassing synapses and the microvasculature. At the ultrastructural level, the bulk of astroglial morphology is indeed a complex spatial meshwork of protrusions with a thickness below $50\,\mathrm{nm}$ [194, 195]. It has been estimated that within the domain of a single hippocampal astrocyte, there are approximately 10^5 synapses [193]. Thus, single astrocytes contact and may control large sets of synapses as well as the vascular bed regulating blood flow to those synapses. This architecture places the astrocyte in a prime position to coordinate synaptic activity.

The elongated geometries of these *in vivo* structures (i.e., blood vessels and axon tracks) that astrocytes and their processes adhere to and orientate along, inspired the approach adopted in this thesis to study astrocytes *in vitro* on the micropatterned substrates providing microbridges.

2.2.2 Tripartite synapse

The fact that information processing in the brain relies not only on synaptic communication between neural cells, but involves also nearby astrocytes, prompted the conceptualization of the "tripartite synapse" [23]. This model is based on the notion that there is a bidirectional, rapid communication between astrocytes and neurons at the synaptic level. Indeed, as demonstrated in *in vitro* cultures [20], astrocytes can express receptors for all kinds of neurotransmitters, depending on the brain region. On the one hand, astroglia takes up neurotransmitters such as glutamate, from the synaptic cleft, and communicates with other cells via calcium (Ca^{2+}) signaling. More in detail, Ca^{2+} influx through the astrocyte plasma membrane is mediated by ionotropic and metabotropic receptors, the astrocytic machinery for sensing neuronal activity and changes in the extracellular environment. Na^+/Ca^{2+} exchangers can increase the concentration of intracellular Ca^{2+}. In turn, Ca^{2+} elevations may induce the activation of inositol triphosphate (IP_3) receptors that trigger Ca^{2+} release from intracellular stores (endoplasmic reticulum and mitochondria). Ca^{2+} events then may propagate beyond single astrocytes and form complex spatiotemporal patterns of Ca^{2+} activity. The frequency of calcium transients is modulated by neuronal activity [196], and provokes changes in local tissue oxygenation [197, 198], and other factors [199]. On the other hand, astroglia also may release gliotransmitters into the synaptic cleft, such as GABA, D-serine, and glutamate, as well as vasoactive metabolites [189, 200]. The result is that astrocytes perform a plethora of different functions, which include regulation of synaptogenesis, synaptic maturation [201] and activity-dependent synaptic elimination [201]. Therefore, the perisynaptic astroglial

comportment has a strong impact on shaping the neural connectome.

2.2.3 Gap junctions

The active participation of astrocytes in brain function implies that they must be equipped for the integration and transmission of signals to other cells, ensuring an efficient way to communicate. Astrocytes typically occupy non-overlapping domains, however they form a syncytium-like network, where individual cells are interconnected through gap-junctions allowing direct exchange of substances from the cytosol [202]. Gap-junctions are channels originating from the juxtaposition of the hemichannels (or connexons) of two neighboring cells. Each connexon is composed of six identical transmembrane proteins called connexins [203], see Fig. 2.2. A single hemichannel connects the cell to the extracellular space. Connexin mediated channels allow the cell to exchange ions or small molecules up to 1.5 kDa, including secondary messengers such as calcium and inositol triphosphate, as reviewed in [204]. Gap-junction and hemichannel mediated signaling is believed to coordinate the action of adjacent astrocytes in terms of electrical and biochemical activity and equalizes their intracellular ion concentrations [205].

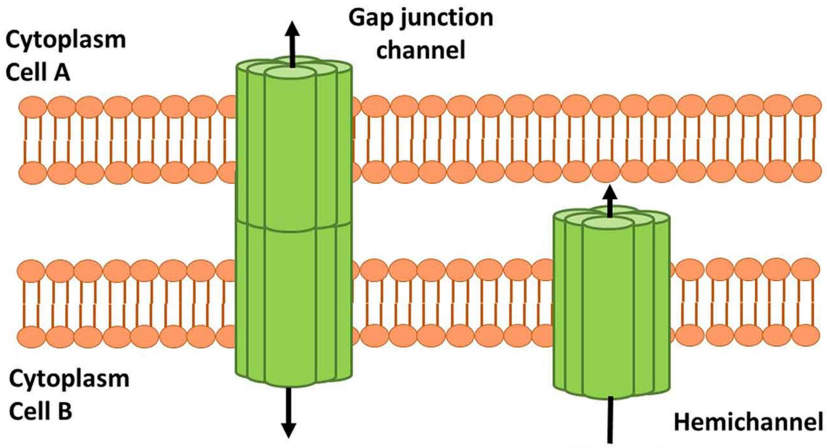

Figure 2.2: Schematic representation of a gap-junction and a hemichannel, formed by connexins in cell membranes. Hemichannels are transmembrane proteins composed of six connexin subunits that allow flow of several molecules and gliotransmitters from astrocyte to the extracellular space. Adapted and reproduced with permission [203]. Copyright ©2018 Mayorquin *et al.*

It is therefore appropriate to define "astrocytic networks" the groups of cells which can exchange information either through gap-junction or exchange of extracellular messengers. In the rat hippocampal CA1 each astrocyte is coupled via gap-junctions with 15.3 ∓ 2.8 other cells, as demonstrated in Ref. [206].

2.2.4 Calcium Signaling

Unlike neurons, astrocytes are not electrically excitable as they cannot generate action potentials. In contrast, they are chemically excitable, meaning that they can provide a biochemical response to stimuli from the environment, especially ions and neurotransmitters. The membrane of astrocytes is hyperpolarized [207] and the resting membrane potential is regulated by a rich variety of ion channels (both voltage dependent and independent). Among the mechanisms underlying the integration and modulation of synaptic transmission cited in the previous paragraphs, many involve calcium signaling [208, 209]. This communication strategy has also been linked to the control of the cerebral blood flow performed by astrocytes [210]. In this section, I will present a few interesting aspects of Ca^{2+} signaling that are a hot topic in current research, highlighting what is relevant for the work presented in this thesis.

When astrocytes *in vitro* are simulated chemically with neurotransmitters or mechanically with micropipettes equipped with piezoelectric actuators, variations of the cytosolic Ca^{2+} concentration are triggered, either in the form of transients or oscillations. Additionally, astrocytes have the capability to increase intracellular Ca^{2+} spontaneously, with no chemical/mechanical stimuli, i.e. without the influence of neuronal activity [211–213]. Most likely, these spontaneous events are triggered by stochastic Ca^{2+} influx in astrocytes through multiple pathways, such as Ca^{2+}-permeable receptors, Ca^{2+}-channels and Na^{+}/Ca^{2+} exchangers located at the plasma membrane [199].

The first observation of glutamate induced intracellular Ca^{2+} elevations and subsequent Ca^{2+} wave propagation in cultured astrocytes goes back to the early nineties [214]. The discovery that focal stimulation of astrocytes generates Ca^{2+} waves traveling over the astroglial syncytium promoted the idea that this is a form of long-range communication to achieve a higher level of brain integration. A comprehensive discussion on the topic can be found in the following references [21, 188].

The propagation of Ca^{2+} was characterized both *in vitro* [214, 215] and *in vivo* [216, 217]. In fact, two main mechanisms for wave propagation were elucidated. Ca^{2+} waves can be mediated by the intercellular diffusion of second messengers like IP_3 through gap-junctions [218, 219] or by the regenerative extracellular ATP-mediated signaling [220, 221] or by a combination of both [222]. In Fig. 2.3, a schematic representation summarizes the main functions of astrocytes connected to Ca^{2+} signaling.

Ca^{2+} influx in astrocytes displays different spatiotemporal characteristics with regards to amplitude, shape and propagation. These differences may be associated to the distinct transduction pathways cited above [224]. There are two major types of Ca^{2+} signals in astrocytes that include intrinsic Ca^{2+} oscillations within single cells and Ca^{2+} waves propagated from one cell to others. Both mechanisms can take place sponta-

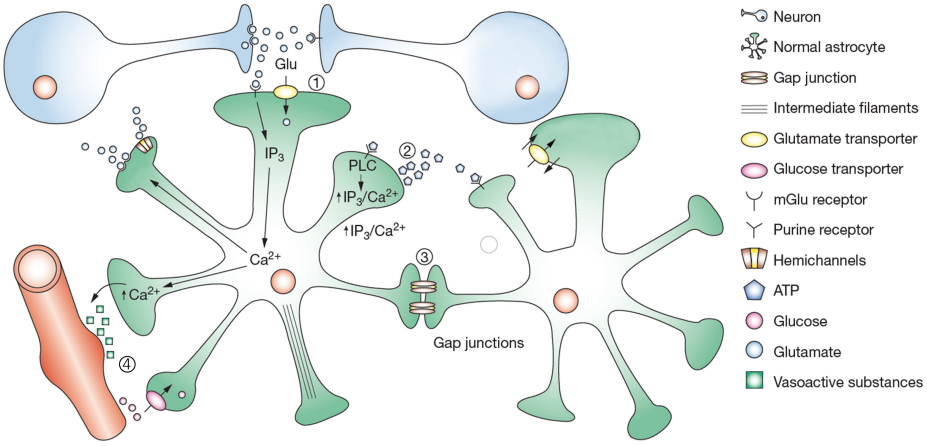

Figure 2.3: Physiological functions of astrocytes. (1) Modulation of synaptic function via glutamate transporters (2) Communication between astrocytes via extracellular ATP release and binding to receptors on adjacent astrocytes. ATP binding results in activation of IP_3, which in turn triggers calcium release from intracellular stores. (3) Gap junctions connect astrocyte to form a syncytium-like network for the exchange of small molecules and cell–cell communication. (4) The regulation of blood flow is modulated by astrocyte end-feet apposing blood vessels, with vasodilation being mediated through release of vasoactive substances. Adapted and reproduced with permission from Ref. [223]. Copyright ©2021 Springer Nature Limited.

neously or can be elicited by external stimuli. As defined by Scemes in [222], a Ca^{2+} wave is a "localized increase in cytosolic Ca^{2+} that is followed by a succession of similar events in a wave-like fashion. These Ca^{2+} waves can be restricted to one cell (intracellular) or transmitted to neighboring cells (intercellular)". Ca^{2+} oscillations, instead, are asynchronous events occurring in individual cells and display a random and repetitive intracellular Ca^{2+} concentration pattern as a function of time [225, 226]. One hypothesis is that Ca^{2+} waves are mediated by IP_3, whereas Ca^{2+} oscillations are mediated primarily by Ca^{2+}-induced Ca^{2+} release. Release of Ca^{2+} induced by elevations of intracellular Ca^{2+} has been suggested in a number of cell types [227], and Ca^{2+} oscillations that are independent of IP_3 have been demonstrated [228].

Astrocytes of different types or localized in different areas of the brain present variations in intracellular Ca^{2+} dynamics. For example, gray matter protoplasmic astrocytes rely mainly on gap-junction for wave propagation. In fact, Haas *et al.* demonstrated in [229] that in a slice preparation of mice lacking the gap-junction protein connexin 43, there was no Ca^{2+} wave propagation. Instead, astrocytes in the white matter of corpus callosum exploit extracellular ATP to spread Ca^{2+} waves, so a gap-junction coupling de-

ficiency does not affect them [229, 230]

At the single astrocyte level, Ca^{2+} events can be restricted to small portions of the cell, and not necessarily propagate to the whole cell soma. Events occurring at the fine astrocytic processes, in particular the perisynaptic ones, are described as microdomains [196]. These events exhibit fast kinetics, with a time scale which is compatible with synaptic modulation [196] and are more frequent than transients localized at the soma or primary branches [231]. The Ca^{2+} transients at the fine branches are mainly sustained by influx from plasma membrane channels. This is due to a favorable surface-to-volume ratio but also because peripheral branches are too small to host organelles that can support Ca^{2+} exchange with intracellular stores. Therefore, the Ca^{2+} influx may spread in the whole cell only if it takes place close enough to the endoplasmic reticulum and can trigger IP_3 release [232]. Ca^{2+} signaling mechanisms are therefore strongly dependent on the morphological parameters of the cell.

In addition to cell shape, Houades *et al.* [233] reported that a second level of spatial organization in astrocytic networks may be important in defining their functional status and their Ca^{2+} propagation properties. In their work, they demonstrated that the functional syncytium of astrocytes is not borderless, as the distribution of connexins in not spatially homogeneous. The morphological boundaries typical of certain brain regions can impose constraints in the astrocytic network shapes. For example, in the pyramidal cell body layer of the hippocampus, the astrocytes are in small number and are localized intercalated between tightly organized neurons [233]. These differences in connexin distribution and shape of the network may have significant impact with respect to Ca^{2+} signals, resting membrane potentials, glutamate metabolism as well as their ability to exchange second messengers between different cells [234].

Altogether, the presented mechanisms for calcium communication in astrocytic networks evidence that astrocytes may be important players in many processes related to brain computational functions. The understanding of the astrocytic involvement in neural processes is still incomplete, and more is required to elucidate the specific role of these cells and their mechanisms of action. Thus, new investigation tools designed specifically to study astrocytic networks must be developed, that may help resolve many of the current controversies [188, 235]. It is clear that astrocytes signaling takes place over different spatial scales of interaction, producing higher order information processing (see Fig. 2.4): at the nanodomain, with a direct impact on synaptic communication and remodeling; at the micrometric scale of the single astrocyte, that can exert an influence over different synapses; at the syncytium level, where astrocytic networks form functional domains; and at the mesoscale, where a long-range interaction between astrocytes from multiple brain regions direct to the activity of neuronal fibers [236].

The traditional techniques to investigate network activity, such as pharmacological blocking or genetic knockout, do not allow the control of a single cell or small ensembles [237]. In this work, cell-patterning tools were developed to physically restrict astrocytic interactions to small networks, with a controlled geometrical shape. The patterns limit the typically highly connected intertwined structure of astrocytic networks to one where cells are only able to interact with a small number of neighboring cells. This technological platform facilitates the study of astrocytes from the single cell level to the network level to improve knowledge and understanding of how communication links to spatial organization over multiple spatial scales, and further *in vitro* research in this area with clinical applications.

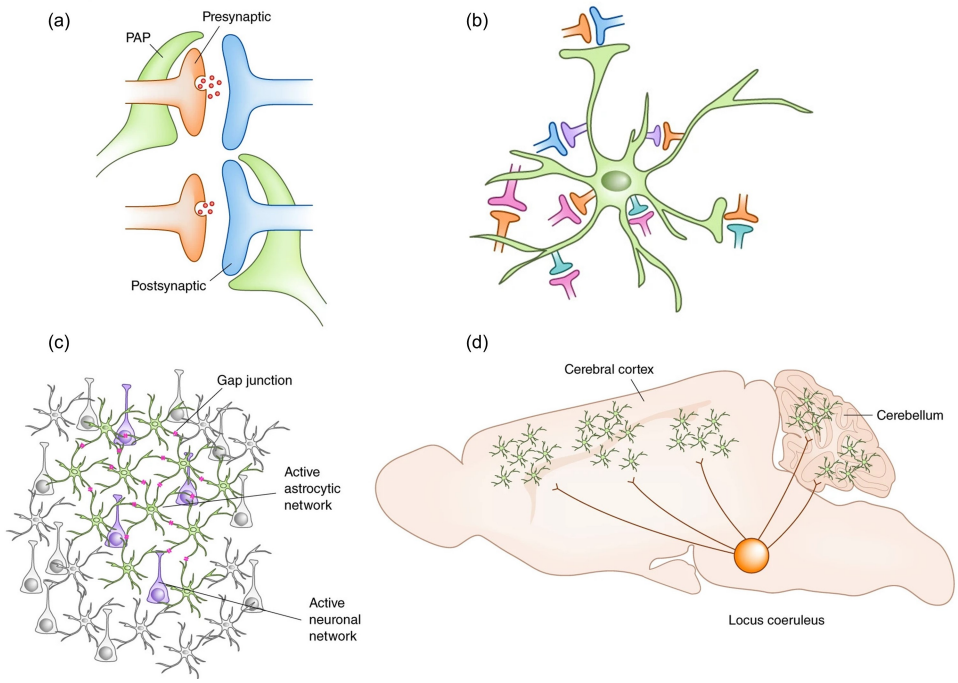

Figure 2.4: Astrocytes communicate over various spatial scales (a) At nanoscale, local signaling in perisynaptic astrocytic processes (PAPs) target synapses. (b) At the microscale level, an individual active astrocyte can affect coordinately multiple synapses. (c) At a syncytium scale, groups of astrocytes can form dynamic networks via gap-junction connectivity to match domains of highly active neurons and support or regulate their function. (d) At the mesoscale level, populations of astrocytes in different brain areas can respond in concert to activity of long-range neuronal projections. Adapted with permission from [236], copyright ©2021 Springer Nature Limited.

2.2.5 Astrocytes in pathology or injury

The observations that astrocytes in the diseased brain undergo transformations in morphology and histology, like changes in shape, size or number, date back to the 19th century [238]. Today, there is consensus that astrocytes respond to and have a prominent role in a variety of pathological events in the CNS, like neurodegenerative and demyelinating diseases, epilepsy, trauma, ischemia, infection, and cancer [239]. Nevertheless, different and often conflicting observations have been reported, as the astrocytic responses are heterogeneous and strictly dependent on the particular pathology [238]. This is further complicated by the plasticity of healthy astrocytes, which can be triggered also by physiological signals in the CNS. Moreover, in the case of spatially confined CNS lesions, astrocytes display a severe to mild response depending on the distance from the core of the injury, with a topographic heterogeneity [240], for example proliferative astrocytes are only found near the injury [241, 242].

A commonly accepted and broad definition for astrocytes that are involved in pathology and brain injury was proposed by Escartin *et al.* [238]. They are, in fact, astrocytes that

> "sense and respond to an abnormal situation in the brain. They change at the morphological, biochemical, transcriptional, and functional levels. These changes are maintained while the pathological stimulus is present but some aspects may resolve. Reactive astrocytes are heterogeneous and may have various effects on disease progression."

These astrocytes may be referred to with the umbrella term *reactive astrocytes* [239] and they show some common features that are observed in different brain injuries or diseases. In general, reactive astrocytes undergo changes in morphology, molecular expression and proliferation.

Morphology

Variations in morphology typically consist in hypertrophy of the soma and of the main processes. Also, astrocytes tend to polarize their processes along the lesion [243] or change their degree of ramification [244]. Loss of primary and secondary astrocyte branches has been reported in mouse models of Alzheimer's Disease[245] and amyotrophic lateral sclerosis [246], and in patients with multiple sclerosis (MS) [247]. In more severe diseases like epilepsy, astrocytes may also retract their fine peripheral processes and overlap more with their neighbors[248, 249].

Molecular changes

Reactive astrocytes display an over-expression of intermediate filament proteins like GFAP or vimentin. GFAP, in particular, is one of the most useful reactivity marker, as its expression increases globally at the population level, in a wide range of brain diseases [250–253]. However, a wide variability in the level of expression between different conditions is observed [254], so to define reactivity, it should be considered also with other markers.

Proliferation

Although the very first observers of astrocytes have noticed increased numbers of nuclei in diseased brains, these phenomena have been shown to occur mainly when there is disruption of the blood–brain barrier [239]. Immunofluorescence studies in patients confirmed that only a small percentage of reactive astrocytes undergoes proliferation [255]. These proliferative astrocytes are in direct contact with a lesion in spinal cord injury [242], they are exposed to blood-borne substrates following invasive injury [256], or their cell bodies are in apposition to blood vessels [243].

So, to summarize, the term *astrocyte reactivity* emphasizes the capacity of these cells to adopt distinct states, i.e., transient or long-lasting conditions characterized by a specific morphology, molecular profile, functions, and distinct impact on diseases that result in a specific phenotype [239].

It is now well known that neural diseases are invariably associated with variations of the physical properties of tissues [175], in particular the progression of disease distorts tissue stiffness and the composition of the ECM [257]. For instance, tissue stiffening is prevalent in traumatic injuries [258], dementia [259] and Alzheimer's disease [260, 261]. On the other hand, soft mechanical signature of glial scars has been recorded in the CNS [262] for multiple sclerosis [263] and glioma [264]. Instead, biophysical modifications of the ECM were observed in demyelinating diseases [263] and in dementia - in particular Alzheimer's disease [175]. These variations of the ECM, in turn, are sensed by the cells via mechanotransductive processes, as discussed in chapter 1. Astrocytes have the ability to perceive the mechanical signals driven by microenvironmental changes [175], and adapt to the physiological or pathological context [265]. Thus, emphasis has been placed on understanding the mechanotransductive relation between astrocytes and tissue mechanics as it may help developing strategies for restoring brain homeostasis [175].

A rewarding approach in this framework is to plate cells onto substrates that mimic *in vitro* the natural microenvironment of astrocytes, taking into consideration the biophysical and structural properties associated with a physiological or pathological condition.

Various nano-fabrication techniques have been developed with the ability to recapitulate the complex features of the ECM that can be used to study the reactivity of astrocytes in culture.

2.3 Biomaterials and astrocytes

A full characterization of the different types of astrocytes, their morphology, development and behavior, is of paramount importance for the understanding of the development of the nervous system, function of neural circuitry and brain pathology.

Studies of the morphological and functional properties of astrocytes are difficult to carry out *in vitro*, as standard 2D cell-culture substrates do not recapitulate the complex topography of the ECM and this leads to a reduction in the heterogeneity of the cells. In fact, astrocytes cultured on standard substrates display a reactive-like phenotype and morphology, similar to that of cells involved in an injury to the CNS [266], with a dramatic change in astrocytic gene expression, proliferation, morphology, and physiology [267].

An important way by which astrocytes adapt to the physiological or pathological context is through mechanotransduction. For example, the biophysical cues provided by the cell-substrate stiffness and by the nano-topography affect the cell membrane tension and can result in ion influx and signaling pathways activation [268–270], as it has been discussed in the previous sections.

Therefore, emphasis has been placed on studying the astrocytic response to changes in the biophysical and structural properties of the cellular microenvironment, by exploiting surface culture substrates that reproduce as faithfully as possible the physical constraints associated with physiological and pathological development. Over the past decades, biomaterial scientists have developed several platforms mimicking the mechanical and topographic properties of the ECM and studied their influence on astrocytic form and function. In the following sections, I will report about the most widespread and rewarding methods for the fabrication of cell-culture substrates engineered with the objective to replicate major properties of the ECM and that are able to provide biophysical and structural cues to astrocytes inducing phenotypes more similar to the *in vivo* situation.

2.3.1 Soft substrates

Hydrogels can be used as substrates to simulate the mechanical properties of the ECM, e.g., to match the softness of the CNS. The three-dimensional environment presented by hydrogels makes them attractive since astrocytes can grow in a context that is similar to

their *in vivo* milieu. This leads to the development of cell cultures with properties that resemble those found in the brain. For example, primary rat cortical astrocytes cultured in 3D collagen hydrogels are less reactive than those cultured on 2D surfaces [271]. Also, a reduction of glial fibrillary acidic protein (GFAP) expression was observed. Similar results were obtained with 3D alginate hydrogels [272] and a peptide hydrogel [273] onto which astrocytes exhibit stellate morphologies and extensive processes outgrowth. These results show that the shape that astrocytes take on when cultured onto hydrogel substrates better mimics astrocyte physiology observed *in vivo*.

2.3.2 Ligand Patterned Substrates

It is well-known that ECM components impact the function of astrocytes [274]. This has led researchers to study how surface chemistry and surface patterning with ECM ligands impact astrocyte growth *in vitro*. Chitosan and gelatin films supported greater astrocyte viability and proliferation compared with the standard cell-culture substrates [275]. Hsiao *et al.* in [276] showed that surface patterning of collagen hydrogels fibrinogen, aggrecan, and laminin lowered chondroitin sulfate proteoglycan (CSPG) expression, a molecule that has been shown to inhibit neuronal regeneration [277]. Also, they demonstrated that fibrinogen, aggrecan, fibronectin, and laminin induced aligned growth of astrocytes, an additional feature that has been shown to control astrocyte reactivity [278].

2.3.3 Substrates with a nano-topographic complexity

The ECM is composed of a complex meshwork of macromolecules, whose assembling results in a anisotropic and irregular environment, with pores and asperities at the nanoscale [56, 279]. With a focus on the interaction of the cells with the surrounding environment and the neighboring cells, nanoengineered surfaces that mimic the nanoscopic topographic features of the ECM have been used to control cell behavior via mechanotransductive processes [62, 100, 101, 280]. The most common fabrication techniques are polymer fiber electrospinning [176, 281] and photolithography [43, 278]. The topographic features must have dimensionalities that cells are able to sense and that influence mechanotransductive processes, which has been demonstrated to be between $100\,\mu\mathrm{m}$ to roughly $1\,\mathrm{nm}$ [282].

Astrocytes grown on substrates topographically defined at the nanoscale undergo several changes, for example they display an *in vivo*-like stellate morphology and extend processes more closely resembling protoplasmic astrocytes compared with those cultured on regular substrates[283, 284]. Also, astrocytes downregulate GFAP expression to a level that is typically associated with a less reactive astrocyte phenotype [283, 285,

286]. Lastly, glutamate transporter expression has also been shown to increase, with a consequent increased glutamate uptake and a neuroprotective effect on cocultured neurons [285, 287].

In this work, I propose a fabrication technique based on SCBD (see section 3.1.1) of zirconia clusters to create reproducible nanostructured films that can be used as cell-culture substrates that resemble *in vivo* nanotopographic ECM features. In chapter 5, I will show how different cellular parameters of astrocytes (cell morphology, cytoskeletal organization and cell functioning in terms of calcium signaling) astrocytes are affected by the distinct levels of nanoroughness of the zirconia surfaces, produced with SCBD.

2.3.4 Micropatterned Substrates

As mentioned previously, properties of astrocytic networks can be investigated with surface modification techniques affecting cell patterning. The surface properties of cell-culture substrates are manipulated to enable control over the spatial configuration of cells and cell/cell interaction. Several methods for patterning consist on the selective modification of the substrate interface to obtain distinct cell adhesive or repelling areas. To my knowledge, the only example in literature of astrocytic cell patterning were carried out by Unsworth group [181, 182] where substrates based on parylene-C/SiO_2 were exploited. In these works, human astrocytes were confined onto squared patterns (75 $\times$ 75 µm) and it was demonstrated that the calcium activity is influenced by the spatial organization of cells. They showed that onto patterned substrates, groups of clustered cells exhibit simultaneous Ca^{2+} transients, which are typically observed *in vivo* or in slices, but not in standard cultures.

In Chapter 4, a list of patterning techniques that were used with different cell types is reported. Moreover, the patterning technique developed in the context of this thesis based on cluster assemble zirconia films is described at length. Also, astrocyte confinement and the possibility to carry out calcium imaging studies is demonstrated. In chapter 6, the analysis of the effect of astrocytic confinement on cell morphology, density, cytoskeletal organization and calcium activity is reported.

CHAPTER 3

Experimental methods

3.1 Fabrication of the substrates

3.1.1 Supersonic cluster beam deposition

SCBD is a bottom-up technique to fabricate thin films, assembled by neutral clusters produced by condensation in the gas phase and accelerated by a supersonic expansion. This approach produces nanostructured films with a nanoscale topography whose roughness can be accurately controlled and varied in a reproducible manner [57]. The precise control over nanoscale topography can be easily obtained over macroscopic areas as required for the large number of experiments typical of in vitro biological assays [55, 59].

A schematic representation of a typical SCBD apparatus is reported in Fig. 3.1 The

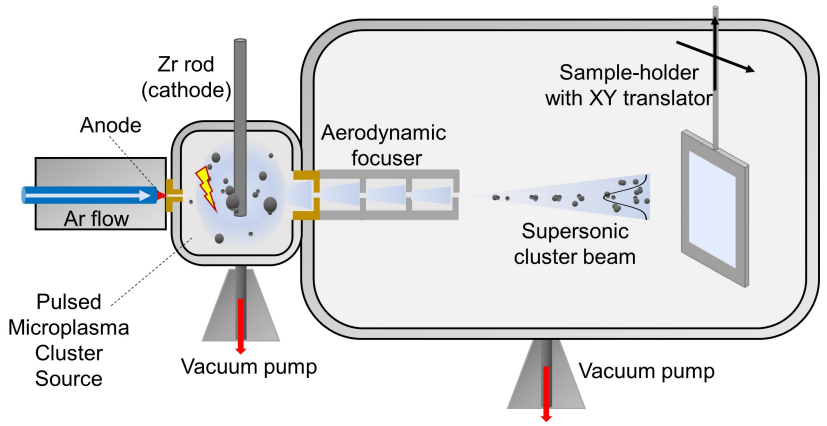

Figure 3.1: Scheme of the SCBD experimental apparatus. The clusters are produced in the pulsed microplasma cluster source (PMCS), that hosts a ceramic body with a cavity where argon is injected by a pulsed valve. The anode is inserted between the ceramic body and the valve. The cathode, a zirconium rod, is inserted into the cavity through a lateral aperture. The clusters are extracted into the deposition chamber through the aerodynamical focuser. The clusters are deposited on substrates mounted on a sample-holder equipped with a translator.

details of the deposition technique can be found in Ref. [133]. Here, I will provide a brief explanation of the functioning principle of SCBD. The source consists of a ceramic body with a cylindrical cavity which hosts a metallic rod, the target. The latter is connected to the negative pole of a power source, thus acts as a cathode. The anode is a copper disc placed near the ceramic cavity. A solenoid valve injects a high-pressure noble gas (He or Ar), from which a plasma is formed via the application of a high voltage discharge between the anode and the cathode. The plasma is confined in the source cavity where it ablates the metallic rod. The species resulting from the ablation condense through collision with the inert gas atoms to form clusters. Then the gas-cluster mixture is extracted from the source following a pressure gradient, generating a supersonic seeded beam. Fig. 3.2 shows a schematic depiction of the main steps of the working principle of the PMCS.

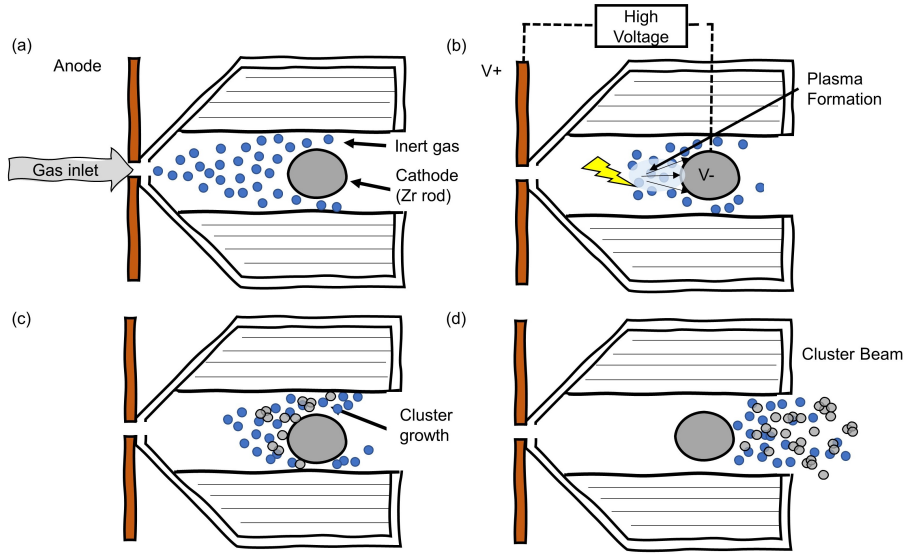

Figure 3.2: Working stages of the PMCS. (a) The injection of an inert gas into the cylindrical chamber. (b) A high voltage is applied between anode and cathode (the rod). An electrical discharge ionizes a small gas volume. (c) Atoms are extracted from the rod surface through the sputtering process and the cluster growth starts. (d) The seeded beam is extracted from the source chamber to the adjacent one, thanks to a pressure gradient. Adapted from Ref. [288]

Before reaching the deposition chamber, the gas-cluster mixture passes through an aerodynamic lenses system which performs both a focusing of the supersonic beam and a cluster mass selection [289]. The resulting beam has a cluster distribution profile that is approximately Gaussian, with larger particles concentrated at the beam center The nanoparticles diameter decreases, going from the beam center to the periphery [290]. By controlling the working parameters of the PMCS, the aerodynamic filters, and the

portion of the beam intercepting the substrate, the nanoparticles distribution can be precisely tuned and reproduced. The average diameter size of clusters deposited with argon as carrier gas is (6.0 ± 1.7) nm [58].

Once reached the deposition chamber, the cluster beam impinges on a sample holder, where clusters are deposited onto a substrate. The sample-holder is moved during the deposition by automated manipulators which enable to cover large surfaces with a rastering process. The cluster beam periodically intercepts a quartz microbalance which monitors the amount of material deposited and deposition rate. The Zr clusters partially oxidize in the cluster source, and in the deposition chamber. Oxidation further proceeds upon exposure of the film to air, resulting in cluster-assembled nanostructured ZrO_x films with x $\sim$ 1.9 [58]. A description of the structural characteristics nanostructured zirconia film can be found in section 1.2.1.

3.1.2 Surface micropatterning

Aerodynamically focused supersonic cluster beams have a high degree of collimation and directionality, which makes them well suited for stencil-assisted patterning (SAP). The large lateral resolution enables the replication of micrometric patterns with features as small as $10\,\mu m$.

Previously, SCBD associated with stencil masks has been used to fabricate three-dimensional nanostructured objects [168] or to integrate nanostructured films onto top-down fabricated platforms, like micro-electromechanical systems (MEMS) [291]. Also, Marelli *et al.* [169] used lift-off masks to deposit nanostructured microresistors on SU-8.

In this thesis, starting from the seminal work of Schulte *et al.* [136], I developed a protocol for the fabrication of cell-culture substrates with complex nanostructured micropatterns, able to confine the adhesion of cells. Microstructures as small as $20\,\mu m$ were routinely obtained exploiting stencil masks.

Here, I will provide a brief description of the fabrication protocol. A more complete explanation is reported in Previdi *et al.*, reprinted in Chapter 5.

Our methodology consists of two steps

- the functionalization of glass coverslips with an anti-fouling molecule which prevents cell adhesion;
- the deposition of cell-adhesive ZrO_x nanostructured micropatterns over the functionalized glass coverslip with SAP-SCBD.

The result is a substrate with cell-adhesive regions surrounded by an anti-fouling area.

The substance selected for the functionalization is the anti-fouling copolymer PAcrAm-g-(PMOXA, NH_2, Si) which can be bound covalently to the hydroxylated surface of a

glass coverslip [292] without affecting its roughness.

For the deposition of micropatterned ZrO_x, we exploited silicon stencil masks fabricated with photo-resist lithography (PRL), which ensure high precision and reproducibility. The stencil masks were not in contact with the deposition substrate, but a dedicated sample-holder guaranteed correct positioning and a small distance between the stencil mask and the substrate, necessary for achieving high lateral resolution. In Chapter 5, I provide a full discussion on the criticalities and potential working solutions for every step of the process. In particular, the functionalization procedure is reported in detail in the supplementary information.

3.1.3 Fabrication of flat zirconia films

The flat ZrO_x films are fabricated with a physical vapor deposition technique based on ion beam sputtering, details can be found in [293]. The sputter deposition setup is schematically depicted in Fig. 3.3.

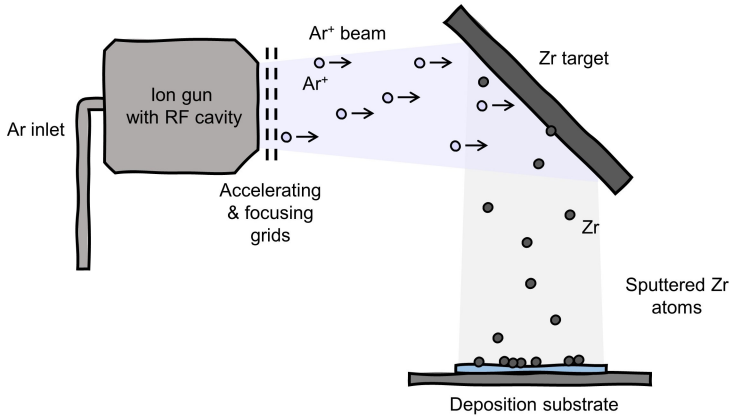

Figure 3.3: Schematic representation of the Zr sputtering apparatus. The ion gun, equipped with a RF cavity generates the Ar^+ beam, which is then accelerated and focused by a series of grids. The Ar^+ ions impinge on the negatively biased Zr target and dislodge Zr atoms, which are then intercepted by a deposition substrate, thus forming a Zr thin film.

In brief, an argon ion beam is generated with an beam ion source (Roth & Rau - RF Ion Beam Source - Cyberis 40) that incorporates a radio frequency plasma cavity [294]. A multi aperture grid system ensures ion extraction and then acceleration and focusing into an ion beam, which then impinges on a negatively charged Zr target, initiating the sputtering process: the incident particles impact the surface or near-surface atoms of the Zr target with sufficient energy to break bonds and dislodge atoms. A part of them, impinge on a deposition substrate placed at a specific angle that maximizes the sputtered

atom flux. A thin film of Zr atoms is formed on the deposition substrate. The sputtering rate is monitored with a microbalance, so that the deposition can be interrupted when the correct film thickness is reached. The Zr atom partly ionize inside the vacuum chamber during the deposition, partly when the samples are brought at atmospheric pressure. Measurements with the AFM confirmed that the resulting films have roughness < 1 nm.

3.2 Characterization of the substrates

3.2.1 Morphological Characterization

The surface morphology of nanostructured ZrO_x thin films was characterized using a Multimode 8 AFM produced by Bruker. Several $2\,\mu\mathrm{m} \times 1\,\mu\mathrm{m}$ images of the ZrO_x surfaces were acquired. The AFM device was operated in air in peak-force tapping mode, using silicon nitride cantilevers mounted onto single-crystal silicon tips with a nominal radius $< 10\,\mathrm{nm}$, and a resonance frequency in the range of 50 - 90 kHz, a scan rate of 1 Hz, and a sampling resolution 2048 $\times$ 512, a scan rate of 1 Hz, and a sampling resolution 2048 $\times$ 512 points. The images were flattened by line-by-line subtraction of first- and second-order polynomials in order to remove artifacts, because of sample tilt and scanner bow. From flattened AFM images, the root-mean-square surface roughness R was calculated as the standard deviation of surface heights.

We verified the roughness of every substrate used in this work. When we refer to, for example, $15\,\mathrm{nm}$-substrates, it means that the mean roughness of the substrate $\pm$ standard error (SE) is compatible with 15 nm.

AFM was also used to measure the thickness of the micropatterned features deposited with SAP. The thickness was calculated by imaging across the step at the edge of the micropattern, and by using a stylus profilometer (Model P-6, KLA-Tencor, Milpitas, CA, USA). For the sake of comparison, during the depositions aimed at producing patterns, nanostructured ZrO_x films were also deposited on monocrystalline silicon substrates (5 mm $\times$ 5 mm) by partially masking the substrate in order to produce a sharp step, and subsequently their thickness was measured. The thickness values measured under different conditions were compatible.

To evaluate the reproducibility of the patterns, we also performed optical characterization of the micropatterned samples. We took phase contrast images with a microscope (Axiovert 40 CFL, Zeiss, Oberkochen, Germany) equipped with 20$\times$/0.3 ph1, CP-ACHROMAT 10$\times$/0.25 Ph1, 5$\times$ /0.12 CP-ACHROMAT objective and with a high definition photo camera (True Chrome HD II, TiEsselab) operated by ISCapture imaging software.

3.3 Cell culture and characterization

3.3.1 Culture of primary astrocytes

We cultured primary astrocytes derived from the hippocampus of neonatal Sprague-Dawley rats (Charles River Laboratories Italia). All the procedures were performed according to the research and animal care procedures approved by the institutional animal care and use committee for good animal experimentation of the Scientific Institute San Raffaele complying with the code of practice for the care and use of animals for scientific purposes of the Italian Ministero della Salute (Ministry of Health) - IACUC Number 728. After extraction, the cells were maintained in MEM medium supplemented with 10% fetal calf serum, 33 mM of glucose, 2 mM of Glutamax, and 2 U/mL of Penicillin- Streptomycin (all reagents were obtained from Thermo Fisher Scientific, Gibco Massachusetts, USA, if not stated otherwise). Cells were grown on standard culture substrates for 12 DIV at 37°C and 5% CO_2, and every 3 days, the culture medium was replaced. Cells were then detached with a trypsin/EDTA solution and, after centrifugation (1000 rpm, 4°C for 5 min), the pellet was resuspended. The cells were subsequently seeded on the patterned substrates with a density of 12500 cells/cm^2. On these substrates, cells were kept in the same culture medium described above for 1 day, replacing the medium the day after. At day 2, the medium was replaced with one with a 1% concentration of fetal calf serum.

3.3.2 ImmunoFluorescence Imaging

All the reagents were purchased from Merck KGaA, Darmstadt, Germany, if not stated otherwise. For the immunofluorescence imaging, we used astrocytes grown on nanostructured films and patterned substrates (dots and micrometric bridges, produced with silicon stencil masks) for 3 days. We fixed them with 4% paraformaldehyde (PFA)/phosphate buffered salin (PBS) for 10 min. We then permeabilized the cell membranes with 0.2% Triton X-100/PBS for 3 min and blocked with 3% bovin serum albumin (BSA)/PBS. Phalloidin, tetramethylrhodamine (TRITC) conjugated was used to stain the actin cytoskeleton of the cells and Hoechst 33,342 for the nucleus. They were incubated for 45 min in a humid environment at room temperature. After the staining, the cells were mounted with ProLong® Gold antifade (MolecularProbes). Images were taken with a SIM confocal microscope (Nikon A1R) with objectives 4×, 10×, and 2× at the UNI^{TECH} NOLIMITS Imaging facility of the University of Milano.

3.3.3 Calcium Imaging

Hippocampal astrocytes grown for 6 days onto nanostructured films and micropatterned substrates were loaded with 2 µL Fluo-4 AM (Thermo Fisher Scientific, Invitrogen, Waltham, MA, USA) for 30 min at 37°C, 5% CO_2. During the experiment, the cells were kept in air, at room temperature, and submerged in Tyrode. This solution contains 119 mM NaCl, 5 mM KCl, 2 mM $CaCl_2$, 2 mM $MgCl_2$, 25 mM HEPES (4-(2-hydroxyethyl)-1-piperazineethanesulfonic acid), and 30 mM D-glucose, the pH was adjusted to 7.4 with NaOH, and the osmolarity was adjusted to 300 mOsm. O_2 was bubbled into the solution for the duration of the experiment. The sample was mounted on a customized holder with tubes enabling constant replacement of the Tyrode solution. We recorded several 5-min time-lapse fluorescence videos with a microscope (Axiovert 135, Zeiss, Oberkochen, Germany), equipped with a standard filter set for fluorescein isothiocyanate (FITC) and a digital camera (Orca-ER, Hamamatsu). Images were taken every 0.4 s.

3.3.4 Characterization of Cell Properties

The phase contrast images were taken with a microscope (Axiovert 40 CFL - Zeiss, Oberkochen, Germany) equipped with 20×/0.3 ph1, CP-ACHROMAT 10×/0.25 Ph1, 5×/0.12 CP-ACHROMAT objective and with a high-definition photo camera (TiEsseLab TrueChrome HD II) operated by ISCapture imaging software.

Cell density

We monitored surface cell density of P1 or P2 astrocytes cultured on flat and nanostructured substrates with a roughness of $10\,\mathrm{nm}$ and $15\,\mathrm{nm}$. We repeated the experiment three times, and for every experiment we had at least 2 replicates for every type of substrate. We carried out the culture for 5 DIV, and took phase contrast images at day 1, 3 and 5. Initial seeding density was the same for every sample. Cell density was calculated manually selecting the cells. The analysis was carried out on at least 10 images for every condition.

Cell morphology

We cultured P1 or P2 astrocytes on flat and nanostructured substrates with a roughness of $10\,\mathrm{nm}$ and $15\,\mathrm{nm}$. We repeated the experiment three times, and for every experiment we had at least 2 replicates for every type of substrate. We carried out the culture for 5 DIV, and took phase contrast images at day 1, 3 and 5. Initial seeding density was low enough to guarantee that the culture would not be confluent at day 5, so to be able to analyze the shapes of independent cells. The cell contour was manually extracted using

the Image Processing Toolbox from MATLAB (2020b, The MathWorks Inc., Natick, MA, USA), and in particular the Image Segmenter App. Then, with custom made scripts developed in MATLAB, we calculated the following parameters:

- the cell area
- the cell complexity
- the cell shape index (CSI) parameter

The cell area was calculated as the number of pixels inside the cell contour, then converted to μm^2.

To calculate the complexity, we first skeletonized the images of a filled cell contour, that means we extracted the centerline while preserving the topology of the object. To do it, we used the built-in MATLAB function *bwskel*, that reduces all objects in a 2D binary image to 1-pixel wide curved lines, without changing the essential structure of the image. The complexity was the number of endpoints of the cell skeleton, which corresponded to the number of cell protrusions.

The CSI parameter was defined as

$$CSI = \frac{p^2}{4\pi A} \tag{3.1}$$

where p is the cell perimeter, i.e. the number of pixels in the cell contour, and A is the cell area, i.e. the number of pixels inside the cell contour. The CSI parameter is $= 1$ for perfectly round cells, and > 1 for elongated or ramified cells.

Actin cytoskeleton

We converted the immunofluorescence 3D stacks to a single 2D image by performing a maximum z-projection, using imageJ (NIH, New York, USA, New York). This function associates to every pixel, the maximum intensity of that pixel over all the images in the stack. We then used custom scripts developed in MATLAB to calculate the actin coverage and the width of the actin fibers.

The actin coverage was calculated in the following way. We defined a unique gray scale intensity interval to which every image was mapped, so to allow comparison between images. The range boundaries were taken as the highest and lowest gray scale intensities among the range boundaries of all the images analyzed. We then set a threshold to 25% of the maximum intensity registered, and we binarized the images by setting to 1 the pixels whose intensity was higher than the threshold. We calculated the number of ones per cell in every image: that was the defined as the actin intensity. We used the Image Segmenter tool (MATLAB) to manually extract the cell borders and to calculate

the pixel area of every cell. The actin coverage was calculated as the percentage of the actin intensity over the cell area.

To extract the width of actin fibers, we extracted 1D intensity profiles of the actin cytoskeleton and a profile of the background intensity. We defined a baseline value as the mean value of the background profile. From the actin profiles, actin fibers were identified as peaks with prominence higher than 3 times the baseline value. The actin fibers widths corresponded to the width at half prominence of the peak (extracted with the MATLAB function *findpeaks*). We extracted 3 profiles for every cell image analyzed.

For the quantification of both the actin coverage and the actin fiber widths, we analyzed 10 cells for every condition. The experiment was repeated twice.

3.3.5 Analysis of calcium imaging data

We analyzed the calcium imaging videos with custom-made scripts developed in MATLAB (2020b, The MathWorks Inc., Natick, MA, USA). The fluorescence traces were extracted as a sum of the intensity of pixels within circular regions of interest (ROI) of equal radius, with the center corresponding to the most responsive cell somas, located manually. Each trace was normalized by the baseline intensity value, and an exponential background was subtracted. We also performed a 10-point box-smoothing of the traces to reduce the high-frequency noise.

Calcium wave events detection

The fluorescence traces displayed peaks and modulation in correspondence to intracellular calcium elevations. Modulations in traces were identified as significant calcium elavations only if their fluorescence intensity was higher than a threshold, defined as the standard deviation of the baseline noise multiplied by 10. We associated to every peak detected a time t_I at which the intracellular calcium elevation begins. We defined t_I as the instant of time at which the fluorescent trace has an intensity equal to half the maximum peak intensity. In fact, peaks typically display a plateau at the time corresponding to the maximum intensity values, thus it is difficult to extract a unique time instant for the peak maximum. The initial calcium elevation instead, is fast with respect to the video-sampling rate, so a unique time instant corresponding to the half height can be extracted more easily. Here, we define a calcium wave event as a set of peaks, identified on different cell traces, which have space-time properties that are compatible with calcium propagation. Experimentally observed calcium waves in cultured astrocytes and slices have a velocity of propagation between 15-27 μm/s and a maximal propagation range of 200-350 μm [295–298]. Therefore, two cells were considered to participate in a calcium wave event if their mutual distance smaller than $350\,\mu\mathrm{m}$ and within a time interval of

$23\,\mathrm{s}$, which corresponds to the time needed to travel $350\,\mu\mathrm{m}$ at the minimum velocity of 15 μm/s. Also, calcium wave events that traveled at a velocity $>$ 27 µm/s were excluded. We made the assumption that the calcium wave could only travel radially [222] away from the source cell, i.e. the first cell exhibiting a peak. The subsequent cells responding were taken as secondary sources which could propagate signals radially away from the primary source. Since calcium elevations can be propagated extracellularly by diffusion of ATP (see introduction, section 2.2.4), we assumed that also the non-nearest neighbors could exchange signals.

This analysis was performed with custom scripts developed in Igor Pro (Wavemetrics, Lake Oswego, OR, USA).

3.3.6 Statistical analysis

Statistical comparisons were performed using the Kruskall-Wallis test [299] followed by multiple post hoc comparison analyses carried out using Bonferroni's method [300]. The difference was considered statistically significant when the p value was < 0.05, indicated with the symbol *. p value < 0.01 was indicated as **, and p value < 0.001 as ***.

CHAPTER 4

Stencil-assisted additive nanofabrication of micropatterned substrates

Supersonic Cluster Beam Deposition (SCBD) has evolved to a point where it meets the essential requirements for the high-throughput production of cluster assembled films enabling the fabrication of micro- and nanodevices [133]. In the last decade SCBD has been used as an efficient method for the large-scale fabrication of nanostructured interfaces with reproducible morphological and functional properties for cell culture. Cluster-assembled zirconia films are not only biocompatible, but they are characterized by a surface topography which also recapitulates the complex nanoscale features of the ECM. These substrates are of great interest in biology as cells are able of sensing the nanoscale topographic features of their microenvironment. The details of the mechanisms ruling this effect are still unknown (see Chapter 1).

Due to the high collimation of supersonic cluster beams, it is possible to exploit stencil masks for the fabrication of patterned films and reproduce features as small as tens of micrometer. The deposition of zirconia patterns on glass surfaces previously functionalized to be cell-repelling, allows the fabrication of culture substrates able to confine the adhesion of cells to specific areas and obtain geometrically controlled cell cultures.

Based on this approach, I developed a technique to reproduce simple networks of brain cells *in vitro*, controlling its geometry and connectivity by culturing living cells on zirconia cluster-assembled dots connected by micrometric bridges. The development of such systems represents a promising tool for bottom-up neuroscience, facilitating the study of the chemical and electric signaling between small ensembles of cells on a local and global scale. In the following pages, I report a thorough explanation of the fabrication process of nanostructured micropatterned ZrO_x substrates. The technical issues of this stencil assisted process are presented, highlighting its criticalities and proposing solutions to overcome them. The effectiveness of the approach is demonstrated with astrocytes, that can be precisely confined on the adhesive areas of the micropatterns.

micromachines

MDPI

Article

Micropatterning of Substrates for the Culture of Cell Networks by Stencil-Assisted Additive Nanofabrication

Anita Previdi [1], Claudio Piazzoni [1], Francesca Borghi [1], Carsten Schulte [1], Leandro Lorenzelli [2], Flavio Giacomozzi [2], Alessio Bucciarelli [2], Antonio Malgaroli [3], Jacopo Lamanna [3], Andrea Moro [3], Gabriella Racchetti [3], Alessandro Podestà [1], Cristina Lenardi [1] and Paolo Milani [1,*]

[1] CIMaINa and Dipartimento di Fisica, Università degli Studi di Milano, Via Celoria 16, 20133 Milano, Italy; anita.previdi@unimi.it (A.P.); claudio.piazzoni@unimi.it (C.P.); francesca.borghi@unimi.it (F.B.); carsten.schulte@unimi.it (C.S.); alessandro.podesta@unimi.it (A.P.); cristina.lenardi@unimi.it (C.L.)
[2] Center for Materials and Microsystems (CMM), Bruno Kessler Foundation (FBK), Via Sommarive 18, 38123 Trento, Italy; lorenzel@fbk.eu (L.L.); giaco@fbk.eu (F.G.); bucciarelli@fbk.eu (A.B.)
[3] Center for Behavioral Neuroscience and Communication (BNC), Università Vita-Salute San Raffaele, Via Olgettina 58, 20132 Milano, Italy; malgaroli.antonio@unisr.it (A.M.); lamanna.jacopo@hsr.it (J.L.); andrea.moro@unimi.it (A.M.); racchetti.gabriella@hsr.it (G.R.)
* Correspondence: paolo.milani@mi.infn.it

Abstract: The fabrication of in vitro neuronal cell networks where cells are chemically or electrically connected to form functional circuits with useful properties is of great interest. Standard cell culture substrates provide ensembles of cells that scarcely reproduce physiological structures since their spatial organization and connectivity cannot be controlled. Supersonic Cluster Beam Deposition (SCBD) has been used as an effective additive method for the large-scale fabrication of interfaces with extracellular matrix-mimicking surface nanotopography and reproducible morphological properties for cell culture. Due to the high collimation of SCBD, it is possible to exploit stencil masks for the fabrication of patterned films and reproduce features as small as tens of micrometers. Here, we present a protocol to fabricate micropatterned cell culture substrates based on the deposition of nanostructured cluster-assembled zirconia films by stencil-assisted SCBD. The effectiveness of this approach is demonstrated by the fabrication of micrometric patterns able to confine primary astrocytes. Calcium waves propagating in the astrocyte networks are shown.

Keywords: micropatterns; nanofabrication; nanostructured zirconia; primary cell networks; cell confinement; astrocytes

Citation: Previdi, A.; Piazzoni, C.; Borghi, F.; Schulte, C.; Lorenzelli, L.; Giacomozzi, F.; Bucciarelli, A.; Malgaroli, A.; Lamanna, J.; Moro, A.; et al. Micropatterning of Substrates for the Culture of Cell Networks by Stencil-Assisted Additive Nanofabrication. *Micromachines* **2021**, *12*, 94. https://doi.org/mi12010094

Received: 2 January 2021
Accepted: 13 January 2021
Published: 18 January 2021

1. Introduction

The in vitro fabrication of cell networks able to simulate the basic elements constituting brain circuits and to maintain their native connectivity is of strategic importance for the understanding of brain circuits' physiology. An emerging field is bottom-up neuroscience, in which basic cellular elements of the brain are thoroughly analyzed to understand the functioning mechanism of higher-level circuits and eventually of the brain as a whole [1–3]. This approach is rewarding, but the interpretation of results is not straightforward, because a functional dissection of each single elementary module from its interacting counterparts is needed. One way around it is to assemble tailored cell networks in vitro by culturing cells on substrates specifically engineered to restrict neural cell adhesion to specific areas that match the topology of simple neural networks [4–6]. Such simplified systems of brain cells represent a tool to perform functional studies as it was demonstrated that small cultures on grid networks yield electrophysiological properties similar to random, brain-scale preparations, despite their unique topology and connectivity [5].

Substrates with controlled topography and chemical composition at the micro- and nano-scale are considered very effective platforms for the study of complex behavior such

as neural cell signaling and to develop high-throughput protocols for drug screening and cell-based therapeutic solutions [7–10]. In addition, surfaces with well-defined nanotopographical properties that mimic the ones present in natural extracellular matrix (ECM) are of particular interest, in the field of mechanobiology, to explore mechanotransduction-dependent modulations of cell phenotype development, adhesion, differentiation, motility, and apoptosis [11,12].

Several methods for substrate micro- and nano-patterning are based on the selective modification of the surface chemistry to create cell-adhesive/repelling regions [11–13]. Among the most widespread methods for chemical patterning, micro-contact printing (MCP) [14] relies on the pattern transfer of the ink of interest from a soft stamp, usually made of polydimethylsiloxane (PDMS) or poly(methyl methacrylate) (PMMA) to a substrate. The master mold is usually a silicon wafer microfabricated with photo-resist lithography (PRL). This technique is simple and flexible towards the choice of substrate and of the ink to be patterned. On the other hand, the fabrication of the master mold is expensive, and the complex multi-step process is time consuming [8,12].

An alternative solution to MCP exploits commercial inkjet printers with simple hardware modifications to create fouling/anti-fouling patterns by directly jetting the chemicals of interest on suitable substrate. This is a low-cost solution for large-scale printing, however, only inks with certain fluidic properties can be printed and the smallest lateral resolution achievable is usually 100 μm. Resolutions down to 1 μm can be achieved with complex and expensive hardware modifications [8,12].

An approach transversal to different fabrication methods is stencil-assisted patterning (SAP). Soft or rigid stencil masks can be fabricated with different techniques (e.g., PRL, ion beam milling, laser cut, chemical etching). Different physical, chemical, or physico-chemical techniques are then used to deposit active species through the mask. Advantages and limits depend on the mask fabrication and deposition techniques used to obtain a certain lateral resolution [8,12].

Topographical patterns at the microscale can be obtained by using top-down subtractive technologies typical of silicon-based MEMS production. Fabrication of simple basic motifs such as grooves, pillars, dots with different dimensions, and pitches has been reported in order to reproduce and to recapitulate the elemental topographical cues that may influence the cell behavior [15,16]. In general, these high-precision fabrication methods have the advantage to be scalable, although with some difficulties. On the other hand, they are quite expensive and basically limited to silicon substrates. Most importantly, it is yet to be demonstrated that starting from simple topographical motifs one can realistically reconstruct the ECM topographical complexity that mediates all the interactions between the cell and its environment [16,17] that are of particular importance also in the neuronal context [18]. In fact, ECM topography is based on a very complex and random entanglement of nanoscale fibers and crosslinked reticular structures [19].

During the last decade, we developed an additive method to fabricate surfaces with multiscale controlled disorder quantitatively mimicking the nanoscale topography of biological systems [20–23]. We concentrated on titania and zirconia surfaces, because of their biocompatibility and their widespread use as implant and prosthetic materials [24,25]. Our bottom-up fabrication method is based on supersonic cluster beam deposition (SCBD) to produce nanostructured films with a nanoscale topography whose roughness can be accurately and reproducibly controlled and varied [23,26–28]. This allows us to fabricate substrates that mimic the intricated morphological characteristics of the ensemble of nanoscale components making up the ECM [23]. The precise control over nanoscale topography can be easily obtained over macroscopic areas, as it is required for the large number of experiments typical of in vitro biological assays, and compatible even with exigent (phospho)proteomics-based approaches [29]. SCBD allows to fabricate nanostructured films with a controlled morphology at the nanoscale. Standard physical vapor deposition techniques based on atom assembling for thin film deposition produce microcrystalline

structure with no control on the nanoscale surface morphology, as discussed in detail in References [27,28].

Here, we report the high-throughput fabrication of micropatterned nanostructured substrates based on SAP, which can confine cells. The peculiarity of our approach is that it enables both cell confinement and replication of an ECM-like morphology on the substrate. This methodology essentially consists of two steps: an anti-fouling molecule is applied to a flat substrate, such as silicon or glass, in order to create a cell-repellent monolayer; then, a nanostructured zirconia (ns-ZrO_x) coating is added via SCBD through stencil masks to create the cell-adhesive regions with controlled nanoscale roughness.

We previously showed that this approach is valid in Reference [30], where we successfully confined a neuronal cell line, PC12, and primary hippocampal neurons on ns-ZrO_x dots of 150 μm diameter. In this work, we demonstrate that it is possible to fabricate much more complex patterns formed by interconnected microstructures, with features as small as tens of micrometers. Moreover, we obtained cell confinement with primary astrocytes, a type of glial cells able to grow elongated processes and known to be particularly adaptive [31,32]. We also report the observation and characterization of calcium waves propagating in a confined astrocyte network as a proof-of-principle of the effectiveness of our method.

2. Materials and Methods

2.1. Substrate Fabrication

The main steps for substrate fabrication are summarized in Figure 1: (a) an anti-fouling molecule is grafted to the surface of a glass substrate, (b) a nanostructured zirconia coating is deposited via SCBD through stencil masks, to create the cell-adhesive regions, and (c) the result is a selectively antifouling substrate where cells attach only on the adhesive areas.

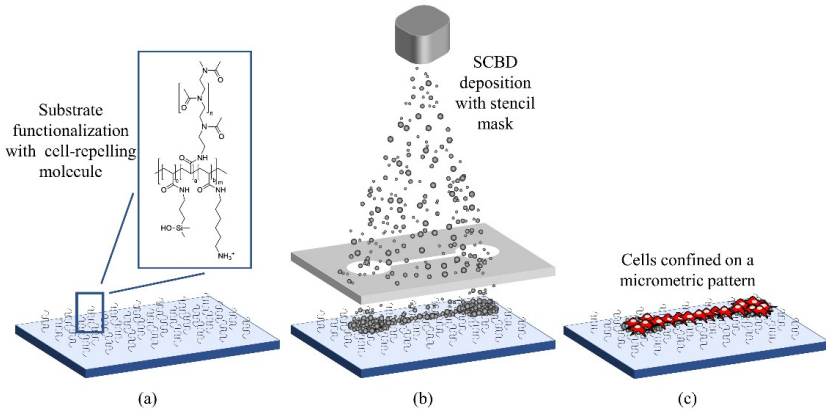

Figure 1. Schematic representation of the fabrication process of substrates for cell confinement.(**a**) The substrate is functionalized with the cell repelling copolymer PAcrAm-g-(PMOXA, NH2, Si). (**b**) A micropatterned film of ns-ZrO_x is deposited via Supersonic Cluster Beam Deposition (SCBD). (**c**) Cells are plated on the substrates and they adhere only to the ns-ZrO_x pattern.

The antifouling molecule is the copolymer PAcrAm-g-(PMOXA, NH2, Si) that binds covalently to the hydroxylated surface [33] without affecting its roughness significantly, see Figure S1 in the Supplementary Information. In the latter, the detailed protocol for the substrate cleaning and functionalization is reported.

Nanostructured zirconia patterns are deposited by a SCBD apparatus equipped with a pulsed microplasma cluster source (PMCS). The details of nanostructured film fabrication process can be found in References [27,28,34].

Figure 2a reports a schematic representation of the SCBD apparatus. In brief, in the PMCS, a zirconium rod is ablated via an aerodynamically confined plasma discharge

ignited after the injection of a high-pressure Ar pulse [35]. The ablated species thermalize with the injected gas and condense to form zirconia clusters inside the source cavity. The latter is connected through a nozzle to a high-vacuum chamber [36]. The cluster/Ar mixture expands into vacuum to form a supersonic seeded beam that impinges on the substrates that are mounted on a sample holder placed at the center of the vacuum chamber (Figure 2a), thus forming a nanostructured zirconia film. Since the nanoscopic roughness of the film is directly proportional to its thickness, we can reproducibly control and tune the surface nano-topographical properties of the cluster-assembled films [27].

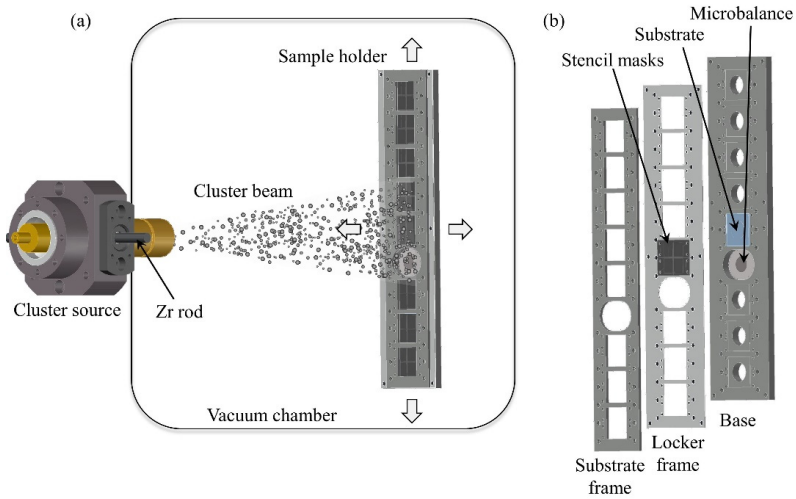

Figure 2. (**a**) Schematic representation of the SCBD apparatus (not to scale): the cluster beam is produced by the pulsed microplasma cluster source (PMCS) equipped with a zirconium rod and it impinges on the sample holder. By rastering the sample holder, a patterned film is deposited on all the samples. (**b**) Design of the sample and stencil mask holder. The three parts ensure the right positioning of the stencil masks with respect to the deposition substrates.

A sample holder hosts the deposition substrates (here glass substrates) and the stencil masks (Figure 2b): the sample holder comprises a base and locker frame, fabricated with mechanical machining of aluminum slabs, holding substrates and stencil masks together, and a substrate frame that ensures the substrates' position. A 4-axis motorized manipulator allows the rastering of the sample holder in order to obtain a uniform deposition over an area of 200 × 40 mm. The holder hosts a quartz microbalance to monitor the deposition rate of zirconia clusters.

2.2. Stencil Mask Fabrication and Characterization

We used stencil masks fabricated with two different techniques: laser cutting (LC) of thin stainless-steel foils and photo-resist lithography (PRL) of silicon wafers. Different pattern designs were evaluated (sub-millimetric dots with or without micrometric channels), and some examples are reported in Figure 3. LC steel masks with dots were purchased from Lasertech Srl (Cernusco sul Naviglio, Milan, Italy), and LC steel masks with dots and micrometric channels were obtained from Kirana Srl (Rovereto, Trento, Italy). The detailed characteristics of the masks with the main features of the stencil patterns are listed in Table S1 of the Supplementary Information.

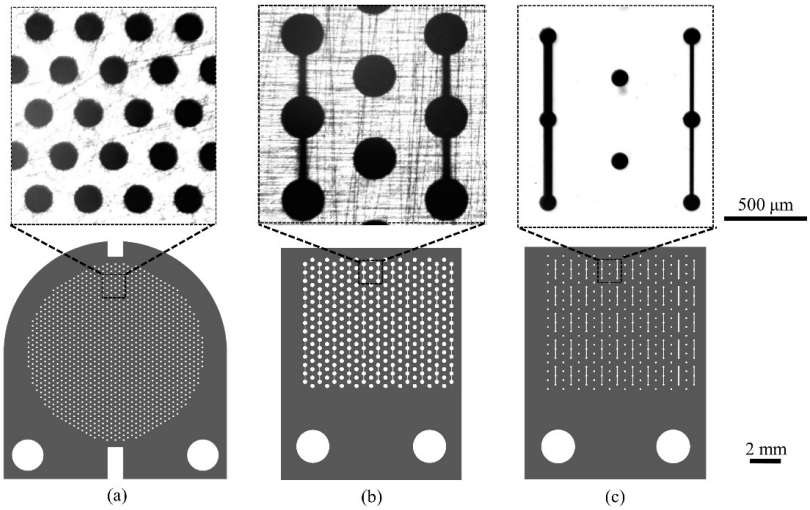

Figure 3. A selection of stencil masks used in this work: design of the mask (bottom) and phase contrast images of details of the pattern (top). (**a**) Stainless-steel mask patterned with dots of diameter 150 µm, interaxial distance 500 µm, 150 µm thin (mask A, Supplementary Table S1). (**b**) Stainless-steel mask patterned with dots and channels. The diameter of the dots is 250 µm, the interaxial distance is 500 µm, and the channels are 20 µm wide. The mask thickness is 50 µm (mask Q13, Supplementary Table S1). (**c**) Silicon mask patterned with dots and channels. The dots' diameter is 100 µm and the interaxial distance is 500 µm. Alternating lines of dots are connected by 20 or 50 µm wide channels. The patterned area is 100 µm thin (mask Q19, see Supplementary Table S1).

LC stainless-steel masks present several advantages: they are cheap, easy-to-handle, and, in principle, reusable indefinitely, provided that an effective cleaning protocol can be established (see the Supplementary Information).

Concerning precision and pattern reproducibility, the LC technique suffers from fabrication defects due to, for example, the re-solidification of drops of metal or loss of planarity of the masks, due to inefficient heat dissipation. Figure 4a,b report optical micrographs of LC stainless-steel masks (the thickness is respectively 150 and 50 µm) with defects like jagged opening borders.

Meanwhile, PRL of silicon allows the manufacture of stencil masks with a high level of precision: features with dimension in the range of a few µm are accurately reproduced. These stencil masks were fabricated starting from a 6" (100) silicon wafer. By using Deep Reactive Ion Etching (DRIE), the features defined by lithography were etched on the silicon frontside, and then, by removing a wider area from the backside, a membrane thickness of 100 µm was obtained. Figure 4c,d show a selection of scanning electron microscope (SEM) images of details of PRL silicon masks. There are no visible fabrication defects in any pattern detail and the openings' borders are smooth. The 20 µm large channel of Figure 4d is produced with no defects. PRL silicon masks are more expensive and much more fragile than LC stainless-steel masks.

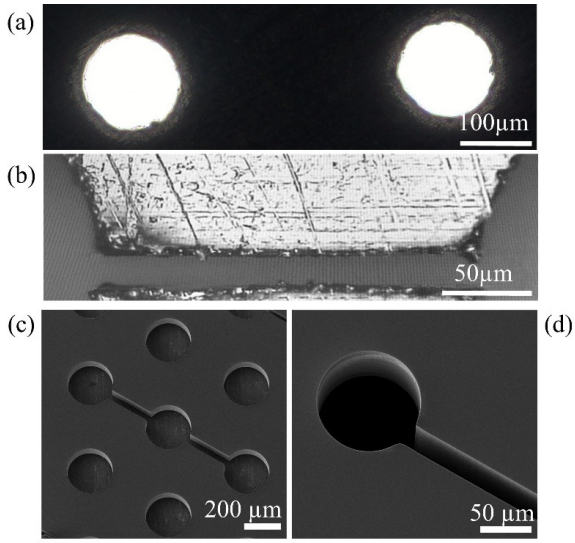

Figure 4. Details of stencil masks produced with LC of stainless-steel foils and with photo resist lithography (PRL) of silicon. (**a**) Optical micrograph of 150 µm wide holes of LC steel mask with jagged borders (mask A, Supplementary Table S1). (**b**) Optical micrograph of a 20 µm wide channel of LC steel mask with a re-solidified drop of metal closing-up the channel opening (mask Q13, Supplementary Table S1). (**c**) SEM image of 250 µm wide dots with an interaxial distance of 500 µm. The channels connecting the dots are 50 µm wide (mask Q19, Supplementary Table S1). (**d**) SEM image of 100 µm wide dot with a 20 µm wide channel (mask Q16, Supplementary Table S1). Images (**c**,**d**) were acquired using a SEM (VEGA3 TESCAN) with a 10 kV electron beam at different magnifications.

2.3. Morphological and Optical Characterization

Atomic force microscopy (AFM) was used to characterize the surface morphology of the substrates and of the films, using a Multimode 8 microscope produced by Bruker. We acquired 5 images of extension 2 × 1 µm of the samples in order to characterize the morphologies of the nanostructured zirconia at the nanoscale. AFM was operated in air in tapping mode, using silicon nitride cantilevers mounted onto single-crystal silicon tips with a nominal radius < 10 nm, a resonance frequency in the range of 250–400 kHz, a scan rate of 1 Hz, and a sampling resolution of 2048 × 512 points. The images were flattened by line-by-line subtraction of first- and second-order polynomials in order to remove artifacts, due to the sample tilt and the scanner bow. From flattened AFM images, the root-mean-square surface roughness (R_q) was calculated as the standard deviation of the surface heights.

The phase contrast images were taken with a microscope (Axiovert 40 CFL, Zeiss, Oberkochen, Germany) equipped with 20×/0.3 ph1, CP-ACHROMAT 10×/0.25 Ph1, 5 × /0.12 CP-ACHROMAT objective and with a high definition photo camera (True Chrome HD II, TiEsselab) operated by ISCapture imaging software.

2.4. Cell Culturing

In this work, we used primary astrocytes derived from the hippocampus of neonatal Sprague-Dawley rats (Charles River Laboratories Italia). All the procedures were performed according to the research and animal care procedures approved by the institutional animal care and use committee for good animal experimentation of the Scientific Institute San Raffaele complying with the code of practice for the care and use of animals for scientific purposes of the Italian Ministero della Salute (Ministry of Health) (IACUC No. 728).

After extraction, the cells were maintained in MEM medium supplemented with 10% fetal calf serum, 33 mM of glucose, 2 mM of Glutamax, and 2 U/mL of Penicillin-Streptomycin (all reagents were obtained from Thermo Fisher Scientific, Gibco Massachusetts, USA, if not stated otherwise). Cells were grown on standard culture substrates for 12 days in vitro (DIV) at 37 °C and 5% CO_2, and every 3 days, the culture medium was replaced. Cells were then detached with a trypsin/EDTA solution and, after centrifugation (1000 rpm, 4 °C for 5 min), the pellet was resuspended. The cells were subsequently seeded on the patterned substrates with a density of 12,500 cells/cm^2. On these substrates, cells were kept in the same culture medium described above for 1 day, replacing the medium the day after. At day 2, the medium was replaced with one with a 1% concentration of fetal calf serum. The following days, the medium was replaced every 3 days. The immunofluorescence images were taken after 3 DIV, whereas the calcium imaging experiments were performed after 6 DIV.

2.5. Immunofluorescence Imaging

All the reagents were purchased from Merck KGaA, Darmstadt, Germany, if not stated otherwise.

For the immunofluorescence imaging, we used astrocytes grown on our patterned substrates (dots and micrometric bridges, produced with silicon stencil masks) for 3 days. We fixed them with 4% paraformaldehyde (PFA)/phosphate buffered salin (PBS) for 10 min. We then permeabilized the cell membranes with 0.2% Triton X-100/PBS for 3 min and blocked with 3% bovin serum albumin (BSA)/PBS. Phalloidin, tetramethylrhodamine (TRITC) conjugated was used to stain the actin cytoskeleton of the cells and Hoechst 33,342 for the nucleus. They were incubated for 45 min in a humid environment at room temperature. After the staining, the cells were mounted with ProLong® Gold antifade (MolecularProbes).

Images were taken with a confocal microscope (Nikon A1R) with objectives 4×, 10×, and 20× at the UNI^{TECH} NOLIMITS Imaging facility of the University of Milano.

2.6. Calcium Imaging

Hippocampal astrocytes grown for 6 days onto a patterned film (100 μm dots connected by 50 and 20 μm wide bridges, produced with a silicon mask) were loaded with 2 μm Fluo-4 AM (Thermo Fisher Scientific, Invitrogen, Waltham, MA, USA) for 30 min at 37 °C, 5% CO_2. During the experiment, the cells were kept in air, at room temperature, and submerged in Tyrode. This solution contains 119 mM NaCl, 5 mM KCl, 2 mM $CaCl_2$, 2 mM $MgCl_2$, 25 mM 4-(2-hydroxyethyl)-1-piperazineethanesulfonic acid (HEPES), and 30 mM D-glucose, the pH was adjusted to 7.4 with NaOH, and the osmolarity was adjusted to 300 mOsm. O_2 was bubbled into the solution for the duration of the experiment. The sample was mounted on a customized holder with tubes enabling constant replacement of the Tyrode solution.

The cells were stimulated with a 100 mM L-Glutamic acid solution (monosodium salt, acquired from Sigma Aldrich, Saint Louis, MO, USA). Droplets of the stimulating solution of volume < 4 pL were delivered with a pressure application device (PDES-01T, npi electronic, Tamm, Germany) equipped with glass micropipettes pulled to have a tip diameter of approximately 3 μm. To wash away the stimulation solution right after its application and limit direct stimulation to few cells located in a restricted area, we used three parallel pipettes of diameter 500 μm filled with Tyrode that ensured a constant flow of solution washing away the glutamate at the stimulated site.

We recorded several 5-min time-lapse fluorescence videos with a microscope (Axiovert 135, Zeiss, Oberkochen, Germany), equipped with a standard filter set for fluorescein isothiocyanate (FITC) and a digital camera (Orca-ER, Hamamatsu).

We analyzed the videos with custom-made scripts developed in MATLAB (2020b, The MathWorks Inc., Natick, MA, USA). The fluorescence traces were extracted as a sum of the intensity of pixels within circular ROIs (Regions of Interest) of equal radius, with the

center corresponding to the most responsive cell somas, located manually. Each trace was normalized by the baseline intensity value, and a linear background was subtracted. We also performed a 10-point box-smoothing of the traces to reduce the high-frequency noise.

3. Results and Discussion

3.1. Replication of Micrometric Stencil Masks' Features

SCBD is particularly effective for the fabrication of micropatterned thin films exploiting stencil masks [37]. The high degree of collimation, typical of supersonic expansions, allows large lateral resolution in the replication of features down to tens of micrometers. The use of aerodynamic lenses allows control on the cluster transverse velocity and mass distribution, with no significant loss in beam flux [38]. The result is a highly focused beam, with a strong intensity gradient decreasing from the center to the periphery, which results in the deposition of films with a relevant radial thickness variation over small areas, typically on the millimetric scale [39].

Films with a homogeneous thickness over large areas can be obtained by rastering the deposition substrates in the plane perpendicular to the beam axis. This allows averaging out the radial intensity dependence. However, rastering reduces the accuracy of reproduction of the stencil mask pattern. In fact, every portion of the deposition substrate will receive clusters impinging with trajectories whose angles with respect to the normal span from zero to the divergence angle of the beam. The penumbra effect around the edges of the patterned deposits causes blurred borders due to clusters overcoming the area located underneath the stencil mask opening.

Figure 5 reports a schematic representation of the deposition process. In the different source–substrate relative positions (Figure 5a), the inclination of the portion of the beam intercepted by each stencil mask opening varies. Figure 5b focuses on one opening of the stencil mask and highlights how the cluster beam overcomes the area under it, due to the non-zero distance between the mask and the substrate and to the inclination of the cluster beam.

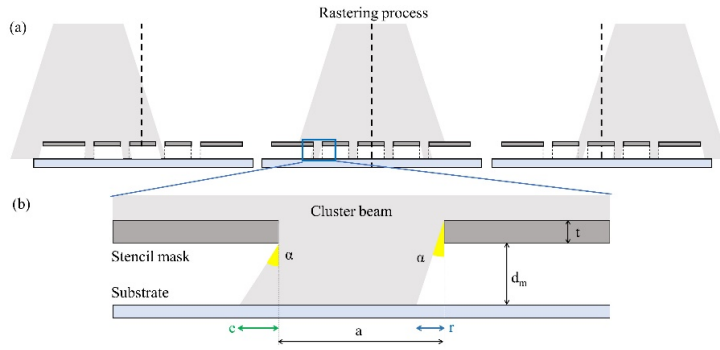

Figure 5. Schematic representation of a beam passing through a stencil mask and impinging on a substrate. (**a**) Rastering process: three different source–substrate relative positions are displayed, in which each opening intercepts a portion of the beam with a different inclination. (**b**) Single mask opening of extension a. A portion of the cluster beam passes through a stencil mask of thickness t with angle α and impinges on a substrate at a distance d_m from the mask. Due to the non-zero inclination of the beam with respect to the normal to the substrate plane and the presence of a gap between the mask and the substrate, the beam overcomes the pattern borders, producing an enlargement e. Also, the right side of the pattern is not completely covered, causing a reduction of extension r in the deposition.

Figure 6 reports the height profile of a patterned film resulting from a perfectly focused cluster beam, where the transverse velocity component of each cluster is negligible (red dotted line), and one resulting from a beam with clusters of different transverse velocities (black, continuous line). The blurring effect consists of both an enlargement of the pattern feature overcoming the borders of the stencil mask holes, in Figure 6 indicated with e, but

also of a reduction in the thickness of the layer deposited close to the borders of the stencil mask holes, indicated by r. The sides of the latter have a shape that reflects the distribution of the transverse velocities of the clusters. The rising width w of the profile is given by the sum of the enlargement e and the reduction r.

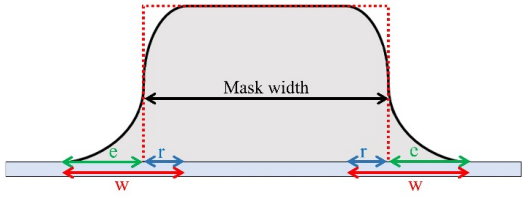

Figure 6. Schematic representation of patterned film height profile obtained with SCBD through a stencil mask, with a non-divergent beam (red dotted line) and with a divergent beam (black continuous line). The cluster beam divergence is responsible for a blurring effect. The lateral sides of the profile rise gradually, with a width w, given by the sum of the enlargement of the mask opening e and the width of the profile that does not reach the maximum height of the film, due to the penumbra effect, r.

The blurring effect can be explained with a purely geometric argument. In fact, with a beam of maximum divergence angle α_{max} and a stencil mask of thickness t at a distance d_m from the deposition substrate, the amplitude of this rising width w can be calculated as:

$$w = e + r = (2\ d_m + t)\ tan(\alpha_{\max}) \quad (1)$$

In order to increase the step sharpness, one should produce a more focused cluster beam, for example, by increasing the supersonicity of the beam [40]. One should also reduce as much as possible the mask-substrate d_m distance and use thin stencil masks (i.e., reduce t). In this specific case, the measured divergence angle of the cluster beam is $\alpha_{\max} = (5 \pm 1)^\circ$, the silicon mask thickness corresponds to $t = (100 \pm 1)$ µm, and the estimated mask–substrate distance is $d_m = (50 \pm 10)$ µm. With these values, according to Equation (1), we expect a rising width $w = (17.5 \pm 5.9)$ µm.

The finite distribution of transverse velocity of the clusters in the supersonic beam is an additional source of pattern distortion. In fact, clusters impinging on the lateral borders of the stencil masks' openings tend to accumulate progressively during the deposition, causing a clogging effect of the stencil mask pattern. Figure 7 schematically shows how the stencil mask opening's diameter gradually decreases as more and more material is deposited on the borders.

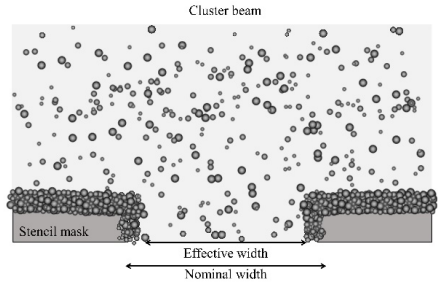

Figure 7. Schematic representation of the clogging effect due to accumulation of zirconia clusters inside the stencil mask's opening: the nominal width of the stencil mask opening is progressively reduced to a smaller effective width as the deposition is carried out.

This produces a progressively conical shape of the deposit. The rising width w is further increased, as the contribution of the clogging effect is summed with the geometric blurring, as described above (Equation (1)). The clogging effect's contribution to w is smaller than the thickness of the deposited film, but it is relevant when the film thickness is comparable to the lateral dimensions of the stencil mask pattern features. In the present work, we deposited films with thickness below 210 nm, and therefore clogging is negligible.

Progressive mask clogging may represent a limit when fabricating patterned films of highly homogenous thickness: the extension of the homogeneous area imposes a limit of the film thickness. On the other hand, as Barborini et al. showed in Reference [40], this effect can be exploited to fabricate nanostructured three-dimensional (3D) objects with controlled geometrical properties, such as nanostructured tips.

Lastly, the quality of the stencil masks is crucial for the accurate reproduction of stencil patterns on substrates. Any defect in fabrication of the stencil mask will be transferred on the patterned film in an amplified manner due to the clogging effect. Among the different approaches available for the fabrication of stencil masks, we tested two different types of masks: LC stainless-steel foils and silicon sheets patterned with PRL. Stencil masks should be as thin as possible and non-deformable to guarantee a constant separation between the mask and the substrate over the whole deposition area.

Due to their fabrication defects, steel stencil masks are suitable for patterns with features of dimensions of the order of 100 μm and when the requirements of pattern transfer concern the extension of the pattern feature areas and not the fine micrometric details of the pattern. The jagged borders of the stencil masks do not compromise the overall pattern topology as they are much smaller than the mean dimension of the pattern features (see Figure S2 in the Supplementary Information).

When the width of LC steel mask's opening is of a few tens of micrometers, the effect of the edge defects becomes more relevant. This is particularly evident, for example, in the pattern given by dots connected by 20 μm wide bridges. The width of the border of the micro-bridges has wiggles of dimensions comparable to the bridge width, therefore the topography is severely affected (see Figure S3 in the Supplementary Information). Defects like consistent wiggles and interruptions in channels were found to affect between 40% and 70% of the channels in each mask.

Higher levels of accuracy in the reproduction of micrometric patterns can be obtained with PRL silicon masks. They present perfectly regular openings, in the micrometric range, so the transferred patterns are only affected by the defects deriving from the beam divergence. The phase contrast images reported in Figure 8a,b show zirconia patterns deposited with PRL silicon masks: the dots are circular, and their borders are smooth, with no wiggles. The bridges present no interruptions, and their width is constant over their whole extension. In Figure 8c, AFM height profiles of micrometric bridges of width 50 μm (blue trace) and 20 μm (red trace) are reported. Both profiles display a plateau area in the central zone of the bridge and a rising width, w, of ~20 μm, compatible with the expected value and irrespective of the channel width. This result is coherent with Equation (1), since the blurring effect does not depend on the width of the mask opening. Although the two height maps were measured on the same sample, the two microbridges have different plateau heights due to the blurring effect at the borders. Here, the width of the channel on the mask is comparable to the rising width of the nanostructured zirconia bridge; therefore, the whole pattern width is affected by blurring. The maximum height of the deposit cannot reach the value expected in an un-patterned area.

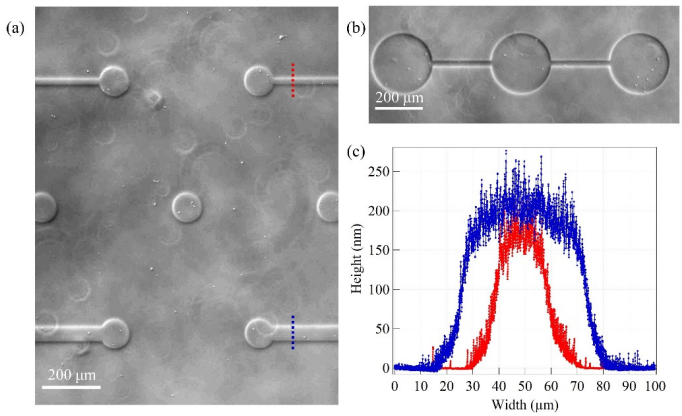

Figure 8. (**a**,**b**) Phase contrast images of ns-ZrO_x patterns obtained with PRL silicon stencil masks. In (**a**) the diameter of the dots is 100 µm, in (**b**) 250 µm (referring to Supplementary Table S1, the labels of the masks are respectively Q16 and Q19). Alternating rows of dots are connected by 20 and 50 µm wide bridges. (**c**) Atomic force microscopy (AFM) height profile maps of ns-ZrO_x micrometric bridges. The blue and red traces correspond to 50 and 20 µm wide bridges, respectively. The profiles were measured on different portions of the same sample: the thickness difference clearly visible in the two profiles can be attributed to the more effective blurring on the smaller mask openings.

3.2. Nanostructured Morphology of the Micropatterns

The possibility of controlling the zirconia morphology at the nanoscale [36] and its homogeneity on the whole patterned sample is of pivotal importance since a small change in the morphological properties of the substrate can determine different functional properties of the thin film and promote specific mechanotransductive signals to the cells [20,21,29,41].

Figure 9 shows the AFM images of the nanostructured zirconia of micrometric bridges characterized by different widths (20 and 50 µm). As mentioned before, when the width of the mask channel is comparable to the dimension of the lateral height gradient of the nanostructured zirconia bridge (as is the case for the 20 µm wide bridge), the highest thickness of the deposited film, characterizing the central plateau, is lowered due to the blurring effect.

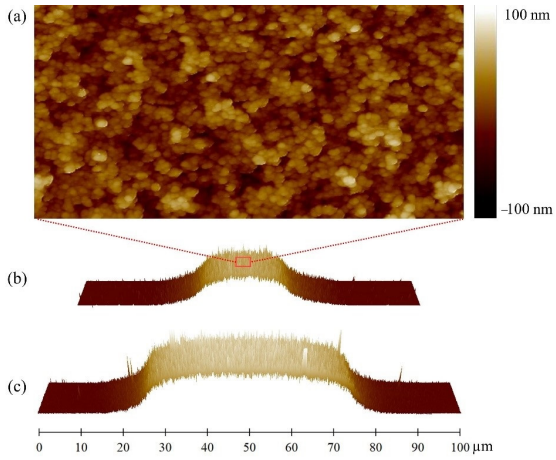

Figure 9. (**a**) Representative AFM topographical map (2 × 1 µm) of nanostructured zirconia in the center of a 20 µm large bridge, z-scale ranges from −100 to 100 nm. (**b**,**c**) Three-dimensional (3D) AFM maps of 50 and 20 µm large bridges, respectively.

The resulting surface roughness, R_q, also decreases, since it depends on the film thickness, t, according to a simple scaling law, $R_q \sim t^{\beta}$ [42], where the growth exponent, β, is 0.4 [36].

The morphological properties of nanostructured zirconia in different regions of the micrometric patterns are summarized in Table 1.

Table 1. Morphological properties of the nanostructured zirconia in different pattern features on the sample.

Geometry of the Pattern	Thickness (nm)	Roughness (nm)
Dot (250 μm diameter)	205 ± 5	19.5 ± 0.7
Bridge a (50 μm wide)	192 ± 5	19.0 ± 0.8
Bridge b (20 μm wide)	162 ± 4	16.5 ± 0.1

In biological applications, it was demonstrated that substrates with different nanoroughness provide distinct biophysical stimuli that can have a direct impact on mechanotransducive cellular structures (such as the integrin adhesion complexes and the cytoskeleton) and eventually cell development and functioning [18,20,21,29].

3.3. Cell Confinement

The effectiveness of our approach in cell confinement with patterned substrates has already been demonstrated with a neuronal cell line, PC12, and with primary hippocampal neurons [30].

Here, we use primary hippocampal astrocytes, a type of brain cells whose biological function has recently been demonstrated to be closely related to neuron signaling [31]. Previously believed to have a mere supportive role in the central nervous system, there is now evidence that astrocytes participate actively in synaptic transmission. The concept of tripartite synapse has been developed to describe the spatial proximity but also functional relation between pre- and post-synaptic neurons and astrocytes at the synaptic level [43].

On standard culture substrates, astrocytes grow in unorganized, interwoven monolayers, in which it is challenging to discriminate the functional connections between adjacent cells. Also, a uniform layer of cells hardly compares to the complex anatomical structures in which astrocytes are found in vivo.

Confining these primary astrocytes is particularly challenging as they can grow elongated processes and express a wide variety of cell adhesion molecules [32,44]. Astrocytes accordingly display a remarkable adaptive plasticity and adhere to many different substrates, allowing, e.g., the interaction with the brain interstitial matrix and the basement membrane in the vicinity of brain capillaries, or to enwrap neuronal components' surfaces [31,44]. Substrates must be fabricated exploiting a combination of materials with robust and stable in time cell-adhesive/repelling properties. Here, we show that the patterned cluster-assembled zirconia substrates represent an effective platform to constrain adhesion of astrocytes onto specific areas and make them follow specific designs determined a priori. We underline that the zirconia films are used in their original state, with no further functionalization to enhance adhesion (such as poly-L-ornithine and matrigel) prior to cell plating.

We tested the patterns with micrometric resolution comprising zirconia bridges connecting dots, fabricated with the procedure described above and using PRL silicon masks. The immunofluorescence images of Figure 10 display the staining of the actin cytoskeleton (red, phalloidin TRITC conjugated) and of the nuclei (blue, Hoechst 33,342) of astrocytes at 3 DIV confined on patterns of dots connected by bridges of different dimensions.

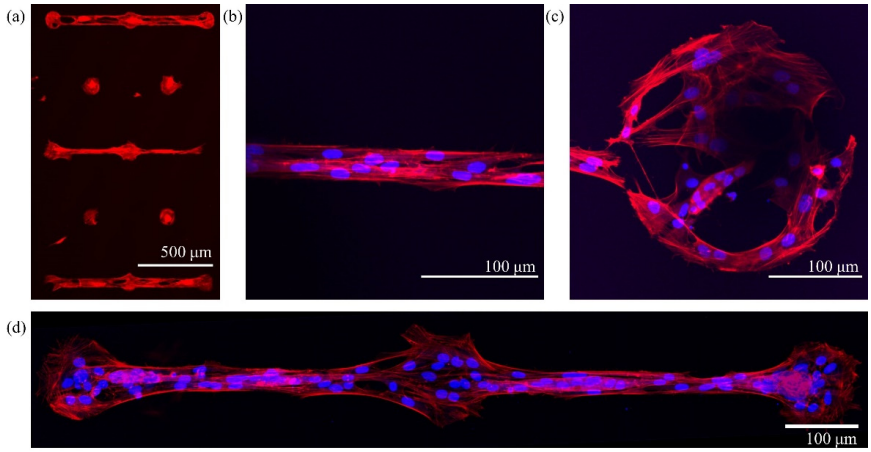

Figure 10. Immunofluorescence images of primary hippocampal astrocytes confined on patterned zirconia substrates, fixed and stained after 3 DIV. The actin cytoskeleton was stained with phalloidin, tetramethylrhodamine (TRITC)- conjugated, red) and the cell nucleus with Hoechst 33,342 (blue). (**a**) Actin cytoskeleton of astrocytes plated on alternating rows of isolated dots and dots connected by microbridges. In the first and fifth row, the microbridge is 50 µm wide, and in the third row, 20 µm. The dots have a diameter of 100 µm. (**b**) Focus on a 20 µm wide microbridge. (**c**) Focus on a dot of diameter 250 µm. The shapes of the cells adapt to the geometry of the portion of the pattern that they occupy, cells on bridges have an elongated shape and processes, oriented parallel to the direction connecting the dots. (**d**) A triplet of 100 µm diameter dots connected by a 20 µm bridge. This image was obtained by combining several 10× images.

In Figure 10a, a low-magnification image shows the actin cytoskeleton of cells in different confinement configurations, i.e., on triplets of dots connected by 20 and 50 µm wide bridges, and on isolated dots. Astrocytes grow only on the adhesive patterned areas and remain confined both on the single dots and on the interconnected triplets of dots. The images in Figure 10b, c show details of pattern features, a 20 µm bridge and a dot of 250 µm diameter, respectively. The image in Figure 10d was obtained by stitching together several 10× images (using the grid stitching plugin of ImageJ, NIH, New York, NY, USA).

Interestingly, cells tend to take on the shape of the underlying pattern: cells on the borders of the dots adapt to their circular shape, whereas cells on the micrometric bridges are elongated toward the direction connecting the dots. On the micrometric bridge, an alignment of the cytoskeleton actin components in the direction parallel to the bridge is clearly visible.

Astrocytes are homogeneously distributed on the adhesive area of the samples, and very few cells adhere on the cell repelling area. A statistical analysis of the images, carried out by counting the nuclei of the cells (average over 5 images), showed that 93% of the cells adhering on the sample surface can be found on the ns-ZrO_x adhesive area portions, occupying only 6% of the total surface available. In more detail, 85 % of the cells are strictly inside the nominal dimension of the pattern feature, 7% are on the border, in contact with the cells within the patterned area, and only 7% of the cells actually adhered on the cell-repelling surface, with no contact with the cells on the ns-ZrO_x areas.

We are thus able to guarantee an optimum level of cell confinement and to determine a priori the geometry of the astrocyte network; potentially, we can also control the shape of the single cells. This is a particularly relevant result from the biological point of view: cells of the same type acquiring different shapes can show relevant physiological differences [45,46]. There is evidence suggesting that astrocytes do not have a homogeneous morphology throughout the brain, with potential implications regarding brain ageing and neurodegenerative diseases [47,48]; however, it is still not understood how astrocyte shape could be physiologically relevant. The possibility of controlling cell shape by fabricat-

ing ad hoc patterned substrates can provide a platform for a rich variety of experiments concerning cell morphology with astrocyte ensembles mimicking anatomical structures.

3.4. Testing the Functionality of the Network

Astrocytes can propagate signals in the form of calcium waves, mediated by channels called gap junctions. Moreover, synchronized calcium activity in astrocyte ensembles has been observed: this provides a mechanism for signal transmission in an organized functional network [49–51].

Cell patterning represents a viable strategy to assemble topologically controlled networks of astrocytes in vitro with a physiologically relevant geometrical shape. These specific platforms represent an important tool that enables the systematic study of calcium wave propagation in astrocytic networks, thus allowing a better understanding of the role of these cells in synaptic signaling in the central nervous system.

We tested the functionality of the astrocyte network on our patterned substrates with calcium imaging, exploiting the Fluo-4 fluorescent indicator. This molecular probe signals the variation of intracellular calcium concentrations. We observed the propagation of calcium waves through neighboring cells both occurring spontaneously and elicited by the application of 100 mM glutamate solution droplets (volume < 4 pL). Astrocytes are known to respond to glutamate, inducing the opening of ion channels and the subsequent rise in cytoplasmic free calcium, which can propagate to neighboring cells [47].

In Figure 11a, we report a fluorescence image of the calcium signal from astrocytes seeded on a patterned substrate. Here, two dots of 100 μm diameter connected by a 50 μm wide bridge are depicted, the third dot is out of the field of view. The border of the zirconia pattern is highlighted with a blue line, and each ROI, corresponding to a cell, is signaled with a red circle and labelled with an index. The indexes are assigned so that ROIs labelled with a lower number correspond to cells closer to the micropipette, whereas "a" and "b" refer to cells on the right and left with respect to the micropipette. The light blue triangle represents the micropipette delivering the glutamate-stimulating solution. In Figure 11b,c, the fluorescent intensity time traces measured from each ROI are reported, with no stimulus (spontaneous activity) and with stimulus (elicited activity), respectively.

The stimulus consisted in the delivery of a droplet of glutamate solution every 30 s (the pressure application device was triggered every 30 s for 50 ms, thus delivering droplets of equal volume < 4 pL), and in the graph, this is indicated by the red triangular markers. In both graphs, the traces are ordered following the position of each ROI with respect to the direction parallel to the bridges, from left to right. The triangle representing the micropipette is reported in Figure 11c, between the traces of ROIs 1a and 1b, corresponding to the two cells closer to the stimulus.

The fluorescence intensity traces registered without and with the periodic glutamate stimulus reveal a distinct behavior in the calcium activity of the astrocytic network. When the cells are not stimulated, spontaneous bursts of increasing intracellular calcium concentration take place and propagate to a few adjacent cells, see for example traces 10a, 11a, 12a, and 13a, which all present a peak at approximately 204 s. The burst is localized within 135 μm, the distance projected onto the direction parallel to the bridge between cell 13a and 10a.

Instead, when the glutamate stimulus was applied, we observed a periodical rise in intracellular calcium in non-adjacent cells, and the stimulus propagated through cells on different sites of the bridge, further away from the micropipette opening. Traces relative to cells on both sides of the pipette, more than 370 μm apart (see, for example, 5b and 10a), all displayed peaks at similar times, proving that geometrically confined astrocytes behave as a functional network.

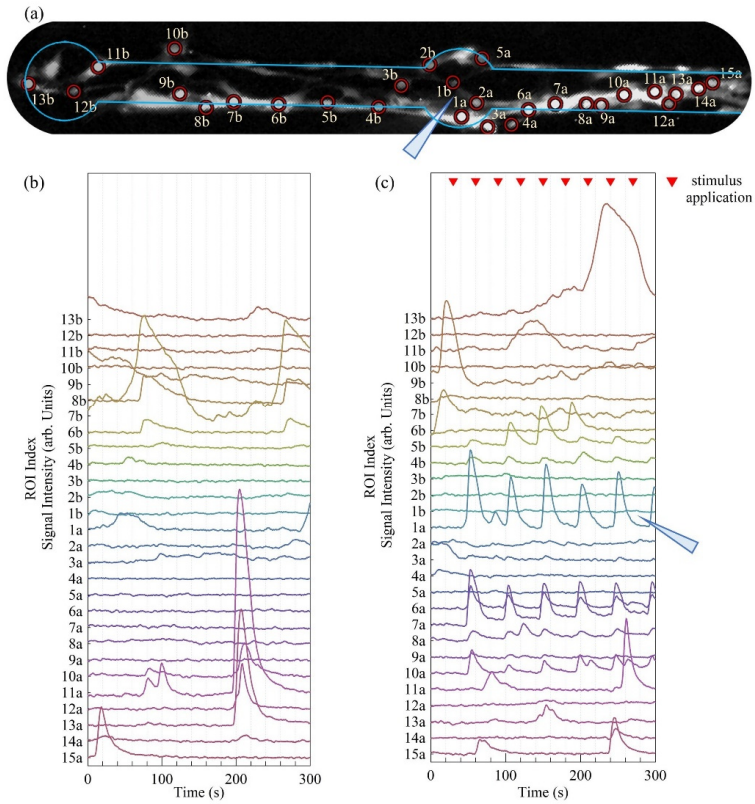

Figure 11. Calcium imaging of astrocytes confined on a micropatterned ns-ZrO_x sample. (**a**) Section of a fluorescent image of the calcium signal from astrocytes seeded on a sample patterned with dots of diameter 100 μm, 500 μm apart and connected by 50 μm wide bridges. Only two dots are included in the field of view. The border of the zirconia pattern is highlighted with a blue line. Red circles include each Region of Interest (ROI), corresponding to a cell. The labels report an index to allow the reader to identify the position of the cell with its calcium trace reported in the graphs below. The light blue triangle represents the micropipette delivering the stimulating solution. (**b**,**c**) Graphs reporting the calcium traces measured from the ROIs reported in image (**a**) when cells are non-stimulated and periodically stimulated with glutamate, respectively. The triangular markers on graph (**c**) indicate the application of the glutamate solution, every 30 s, and the light blue triangle represents the position of the pipette with respect to the cells. The indexes' number increases for increasing distance of the cells from the pipette tip, and the letters a and b indicate whether cells are of the right or left side of the pipette.

This is a proof-of-principle that this approach provides a reliable method for the study of calcium waves in geometrically defined networks of astrocytes. A systematic characterization of the calcium propagation of cells grown of substrates with different nano-roughness or geometrical features of the pattern potentially mimicking the shapes of significant anatomic structures will be provided in future works.

4. Conclusions

We developed a versatile and reliable experimental protocol to produce culture substrates for cell confinement onto different micrometric patterns, with an ECM-mimicking surface nanotopography. The nanostructured micropatterned zirconia films are deposited with the SCBD through stencil masks on glass substrates prepared with an anti-fouling treatment. Compared to other micro-fabrication techniques, this method provides cell con-

finement by exploiting a biocompatible material, with a nanoscale topography reproducing the natural environment of cells. Compatibly with the need of a large number of samples typical of biological experiments, our method is suitable for production on a large scale.

In this work, we showed a strategy that enables to reproduce patterns with controlled topographical features both at the nanoscale (surface roughness) and at the microscale (micrometric pattern). Stainless-steel masks fabricated with the LC technology provided accurate results for patterns with features larger than 50 μm, whereas PRL silicon masks are suitable for the reproduction of patterns with features down to a few micrometers. The patterned zirconia films have a well-defined nano-morphology that can be accurately reproduced and varied to meet the requirements of the particular biological system under research.

The effectiveness of our cell culture substrates was tested with primary hippocampal astrocytes: we found a stable confinement and adhesion of the cells on the predefined zirconia patterned areas with no further cell adhesion-enhancing functionalization. The versatility of the pattern design enables to systematically approach the investigation of the behavior of modular systems of cells, thus providing a platform for the in vitro reconstruction of complex architectures.

Astrocytes grown on our patterned substrates display a rich calcium activity both spontaneous and elicited by glutamate application, as indicated by the propagation of a stimulated calcium wave along a micrometric bridge. This represents an important starting point for a systematic characterization of calcium signals in geometrically predefined astrocytic networks.

Supplementary Materials: The following are available online at https://www.mdpi.com/2072-666X/12/1/94/s1, Figure S1. Morphological AFM maps (2 × 1 μm) of glass coverslips, Table S1. Summary of the different types of masks tested in this work, Figure S2. Nanostructured zirconia dots, phase contrast image, and morphological AFM map, Figure S3. nanostructured zirconia pattern reproduced with a LC steel stencil mask, Figure S4. The clogging effect.

Author Contributions: Conceptualization: P.M., C.S., A.M. (Antonio Malgaroli), J.L., A.P. (Alessandro Podestà), and C.L.; methodology—sample fabrication: A.P. (Anita Previdi) and C.P., methodology—cell culture and preparation: A.P. (Anita Previdi), A.M. (Andrea Moro), C.S. and J.L., and G.R.; methodology—AFM-characterization: F.B. and A.P. (Alessandro Podestà); methodology—etching of silicon masks: L.L., F.G., and A.B.; data curation and analysis: A.P. (Anita Previdi) and C.P.; writing—original draft preparation, C.P., A.P. (Anita Previdi) and F.B.; writing—review and editing, A.P. (Anita Previdi), C.S., C.P., F.B., A.P. (Alessandro Podestà), P.M. and A.M. (Antonio Malgaroli); visualization, A.P. (Anita Previdi), C.P. and F.B.; supervision, P.M.; project administration, P.M.; funding acquisition, P.M. and A.M. (Antonio Malgaroli). All authors have read and agreed to the published version of the manuscript.

Funding: This research received no external funding.

Institutional Review Board Statement: All the procedures were performed according to the research and animal care procedures approved by the institutional animal care and use committee for good animal experimentation of the Scientific Institute San Raffaele, complying with the code of practice for the care and use of animals for scientific purposes of the Italian Ministero della Salute (Ministry of Health) (IACUC No. 728).

Informed Consent Statement: Not applicable.

Data Availability Statement: Data is contained within the article or Supplementary Material.

Acknowledgments: F.B. thanks Centro Universitario Cattolico (CUC) for partially supporting this work and Roberto Presilla and Alessandro Tredicucci for stimulating discussions. C.P. thanks Daniele Viganò and Federico Pezzotta for their technical assistance in sample holders' machining. C.S. thanks Francesco Mario Esposito for his contribution in the development of the protocol for the antifouling functionalization of the substrates. C.S. thanks the support of the UNI^{TECH} NOLIMITS Imaging facility at the University of Milan for the confocal microscopy imaging.

Conflicts of Interest: The authors declare no conflict of interest.

References

1. Bargmann, C.I.; Marder, E. From the Connectome to Brain Function. *Nat. Methods* **2013**, *10*, 483–490. [CrossRef] [PubMed]
2. Blankenship, A.G.; Feller, M.B. Mechanisms Underlying Spontaneous Patterned Activity in Developing Neural Circuits. *Nat. Rev. Neurosci.* **2010**, *11*, 18–29. [CrossRef] [PubMed]
3. Lerner, T.N.; Ye, L.; Deisseroth, K. Communication in Neural Circuits: Tools, Opportunities, and Challenges. *Cell* **2016**, *164*, 1136–1150. [CrossRef] [PubMed]
4. Marconi, E.; Nieus, T.; Maccione, A.; Valente, P.; Simi, A.; Messa, M.; Dante, S.; Baldelli, P.; Berdondini, L.; Benfenati, F. Emergent Functional Properties of Neuronal Networks with Controlled Topology. *PLoS ONE* **2012**, *7*, e34648. [CrossRef] [PubMed]
5. Shein-Idelson, M.; Ben-Jacob, E.; Hanein, Y. Engineered Neuronal Circuits: A New Platform for Studying the Role of Modular Topology. *Front. Neuroeng.* **2011**, *4*, 1–8. [CrossRef] [PubMed]
6. Wheeler, B.C.; Brewer, G.J. Designing Neural Networks in Culture. *Proc. IEEE* **2010**, *98*, 398–406. [CrossRef]
7. Jung, D.R.; Kapur, R.; Adams, T.; Giuliano, K.A.; Mrksich, M.; Craighead, H.G.; Taylor, D.L. Topographical and Physicochemical Modification of Material Surface to Enable Patterning of Living Cells. *Crit. Rev. Biotechnol.* **2001**, *21*, 111–154. [CrossRef]
8. Martinez-Rivas, A.; González-Quijano, G.K.; Proa-Coronado, S.; Séverac, C.; Dague, E. Methods of Micropatterning and Manipulation of Cells for Biomedical Applications. *Micromachines* **2017**, *8*, 347. [CrossRef]
9. Park, T.H.; Shuler, M.L. Integration of Cell Culture and Microfabrication Technology. *Biotechnol. Progress* **2003**, *19*, 243–253. [CrossRef]
10. Wong, J.Y.; Leach, J.B.; Brown, X.Q. Balance of Chemistry, Topography, and Mechanics at the Cell–Biomaterial Interface: Issues and Challenges for Assessing the Role of Substrate Mechanics on Cell Response. *Surf. Sci.* **2004**, *570*, 119–133. [CrossRef]
11. Chen, C.S.; Mrksich, M.; Huang, S.; Whitesides, G.M.; Ingber, D.E. Geometric Control of Cell Life and Death. *Science* **1997**, *276*, 1425–1428. [CrossRef] [PubMed]
12. Falconnet, D.; Csucs, G.; Michelle Grandin, H.; Textor, M. Surface Engineering Approaches to Micropattern Surfaces for Cell-Based Assays. *Biomaterials* **2006**, *27*, 3044–3063. [CrossRef] [PubMed]
13. Thomas, C.H.; Collier, J.H.; Sfeir, C.S.; Healy, K.E. Engineering Gene Expression and Protein Synthesis by Modulation of Nuclear Shape. *Proc. Natl. Acad. Sci. USA* **2002**, *99*, 1972–1977. [CrossRef] [PubMed]
14. Perl, A.; Reinhoudt, D.; Huskens, J. Microcontact printing: Limitations and achievements. *Adv. Mater.* **2009**, *21*, 2257–2268. [CrossRef]
15. Chen, W.; Shao, Y.; Li, X.; Zhao, G.; Fu, J. Nanotopographical Surfaces for Stem Cell Fate Control: Engineering Mechanobiology from the Bottom. *Nano Today* **2014**, *9*, 759–784. [CrossRef]
16. Dalby, M.J.; Gadegaard, N.; Oreffo, R.O.C. Harnessing Nanotopography and Integrin-Matrix Interactions to Influence Stem Cell Fate. *Nat. Mater.* **2014**, *13*, 558–569. [CrossRef]
17. Young, J.L.; Holle, A.W.; Spatz, J.P. Nanoscale and Mechanical Properties of the Physiological Cell–ECM Microenvironment. *Exp. Cell Res.* **2016**, *343*, 3–6. [CrossRef]
18. Chighizola, M.; Dini, T.; Lenardi, C.; Milani, P.; Podestà, A.; Schulte, C. Mechanotransduction in Neuronal Cell Development and Functioning. *Biophys. Rev.* **2019**, *11*, 701–720. [CrossRef]
19. Gasiorowski, J.Z.; Murphy, C.J.; Nealey, P.F. Biophysical Cues and Cell Behavior: The Big Impact of Little Things. *Ann. Rev. Biomed. Eng.* **2013**, *15*, 155–176. [CrossRef]
20. Schulte, C.; Ripamonti, M.; Maffioli, E.; Cappelluti, M.A.; Nonnis, S.; Puricelli, L.; Lamanna, J.; Piazzoni, C.; Podestà, A.; Lenardi, C.; et al. Scale Invariant Disordered Nanotopography Promotes Hippocampal Neuron Development and Maturation with Involvement of Mechanotransductive Pathways. *Front. Cell. Neurosci.* **2016**, *10*, 1–22. [CrossRef]
21. Schulte, C.; Rodighiero, S.; Cappelluti, M.A.; Puricelli, L.; Maffioli, E.; Borghi, F.; Negri, A.; Sogne, E.; Galluzzi, M.; Piazzoni, C.; et al. Conversion of Nanoscale Topographical Information of Cluster-Assembled Zirconia Surfaces into Mechanotransductive Events Promotes Neuronal Differentiation. *J. Nanobiotechnol.* **2016**, *14*, 1–24. [CrossRef] [PubMed]
22. Schulte, C.; Podestà, A.; Lenardi, C.; Tedeschi, G.; Milani, P. Quantitative Control of Protein and Cell Interaction with Nanostructured Surfaces by Cluster Assembling. *Acc. Chem. Res.* **2017**, *50*, 231–239. [CrossRef] [PubMed]
23. Schulte, C. 10—Cluster-assembled nanostructured materials for cell biology. In *Frontiers of Nanoscience*; Milani, P., Sowwan, M., Eds.; Cluster Beam Deposition of Functional Nanomaterials and Devices; Elsevier: London, UK, 2020; Volume 15, pp. 271–289.
24. Manicone, P.F.; Rossi Iommetti, P.; Raffaelli, L. An Overview of Zirconia Ceramics: Basic Properties and Clinical Applications. *J. Dent.* **2007**, *35*, 819–826. [CrossRef] [PubMed]
25. Yin, Z.F.; Wu, L.; Yang, H.G.; Su, Y.H. Recent Progress in Biomedical Applications of Titanium Dioxide. *Phys. Chem. Chem. Phys.* **2013**, *15*, 4844–4858. [CrossRef] [PubMed]
26. Barborini, E.; Kholmanov, I.N.; Piseri, P.; Ducati, C.; Bottani, C.E.; Milani, P. Engineering the Nanocrystalline Structure of TiO2 Films by Aerodynamically Filtered Cluster Deposition. *Appl. Phys. Lett.* **2002**, *81*, 3052–3054. [CrossRef]
27. Borghi, F.; Sogne, E.; Lenardi, C.; Podestà, A.; Merlini, M.; Ducati, C.; Milani, P. Cluster-Assembled Cubic Zirconia Films with Tunable and Stable Nanoscale Morphology against Thermal Annealing. *J. Appl. Phys.* **2016**, *120*, 055302. [CrossRef]
28. Wegner, K.; Piseri, P.; Tafreshi, H.V.; Milani, P. Cluster Beam Deposition: A Tool for Nanoscale Science and Technology. *J. Phys. D Appl. Phys.* **2006**, *39*, R439. [CrossRef]

29. Maffioli, E.; Schulte, C.; Nonnis, S.; Grassi Scalvini, F.; Piazzoni, C.; Lenardi, C.; Negri, A.; Milani, P.; Tedeschi, G. Proteomic Dissection of Nanotopography-Sensitive Mechanotransductive Signaling Hubs That Foster Neuronal Differentiation in PC12 Cells. *Front. Cell. Neurosci.* **2018**, *11*, 417. [CrossRef]
30. Schulte, C.; Lamanna, J.; Moro, A.S.; Piazzoni, C.; Borghi, F.; Chighizola, M.; Ortoleva, S.; Racchetti, G.; Lenardi, C.; Podestà, A.; et al. Neuronal Cells Confinement by Micropatterned Cluster-Assembled Dots with Mechanotransductive Nanotopography. *ACS Biomater. Sci. Eng.* **2018**, *4*, 4062–4075. [CrossRef]
31. Verkhratsky, A.; Nedergaard, M. Physiology of Astroglia. *Physiol. Rev.* **2018**, *98*, 239–389. [CrossRef]
32. Liddelow, S.; Hoyer, D. Astrocytes: Adhesion Molecules and Immunomodulation. *Curr. Drug Targets* **2016**, *17*, 1871–1881. [CrossRef] [PubMed]
33. Weydert, S.; Zürcher, S.; Tanner, S.; Zhang, N.; Ritter, R.; Peter, T.; Aebersold, M.J.; Thompson-Steckel, G.; Forró, C.; Rottmar, M.; et al. Easy to Apply Polyoxazoline-Based Coating for Precise and Long-Term Control of Neural Patterns. *Langmuir* **2017**, *33*, 8594–8605. [CrossRef] [PubMed]
34. Podestà, A.; Bongiorno, G.; Scopelliti, P.E.; Bovio, S.; Milani, P.; Semprebon, C.; Mistura, G. Cluster-Assembled Nanostructured Titanium Oxide Films with Tailored Wettability. *J. Phys. Chem. C* **2009**, *113*, 18264–18269. [CrossRef]
35. Tafreshi, H.V.; Piseri, P.; Benedek, G.; Milani, P. The Role of Gas Dynamics in Operation Conditions of a Pulsed Microplasma Cluster Source for Nanostructured Thin Films Deposition. *J. Nanosci. Nanotechnol.* **2006**, *6*, 1140–1149. [CrossRef]
36. Borghi, F.; Podestà, A.; Piazzoni, C.; Milani, P. Growth Mechanism of Cluster-Assembled Surfaces: From Submonolayer to Thin-Film Regime. *Phys. Rev. Appl.* **2018**, *9*, 1–14. [CrossRef]
37. Barborini, E.; Vinati, S.; Leccardi, M.; Repetto, P.; Bertolini, G.; Rorato, O.; Lorenzelli, L.; Decarli, M.; Guarnieri, V.; Ducati, C.; et al. Batch Fabrication of Metal Oxide Sensors on Micro-Hotplates. *J. Micromech. Microeng.* **2008**, *18*, 055015. [CrossRef]
38. Piseri, P.; Podestà, A.; Barborini, E.; Milani, P. Production and Characterization of Highly Intense and Collimated Cluster Beams by Inertial Focusing in Supersonic Expansions. *Rev. Sci. Instrum.* **2001**, *72*, 2261–2267. [CrossRef]
39. Chiappini, C.; Piseri, P.; Vinati, S.; Milani, P. Supersonic Cluster Beam Deposition of Nanostructured Thin Films with Uniform Thickness via Continuously Graded Exposure Control. *Rev. Sci. Instrum.* **2007**, *78*, 066105. [CrossRef]
40. Barborini, E.; Piseri, P.; Podesta', A.; Milani, P. Cluster Beam Microfabrication of Patterns of Three-Dimensional Nanostructured Objects. *Appl. Phys. Lett.* **2000**, *77*, 1059–1061. [CrossRef]
41. Chighizola, M.; Previdi, A.; Dini, T.; Piazzoni, C.; Lenardi, C.; Milani, P.; Schulte, C.; Podestà, A. Adhesion Force Spectroscopy with Nanostructured Colloidal Probes Reveals Nanotopography-Dependent Early Mechanotransductive Interactions at the Cell Membrane Level. *Nanoscale* **2020**, *12*, 14708–14723. [CrossRef]
42. Family, F. Dynamic Scaling and Phase Transitions in Interface Growth. *Phys. A Stat. Mech. Appl.* **1990**, *168*, 561–580. [CrossRef]
43. Haydon, P.G. Glia: Listening and Talking to the Synapse. *Nat. Rev. Neurosci.* **2001**, *2*, 185–193. [CrossRef] [PubMed]
44. Hillen, A.E.J.; Burbach, J.P.H.; Hol, E.M. Cell Adhesion and Matricellular Support by Astrocytes of the Tripartite Synapse. *Prog. Neurobiol.* **2018**, *165–167*, 66–86. [CrossRef] [PubMed]
45. Vogel, V.; Sheetz, M. Local Force and Geometry Sensing Regulate Cell Functions. *Nat. Rev. Mol. Cell Biol.* **2006**, *7*, 265–275. [CrossRef]
46. McBeath, R.; Pirone, D.M.; Nelson, C.M.; Bhadriraju, K.; Chen, C.S. Cell Shape, Cytoskeletal Tension, and RhoA Regulate Stem Cell Lineage Commitment. *Dev. Cell* **2004**, *6*, 483–495. [CrossRef]
47. Cornell-bell, A.H.; Finkbeiner, S.M.; Cooper, M.S.; Smith, S.J. Glutamate Induces Calcium Waves in Cultured Astrocytes: Long-Range Glial Signaling. *Science* **1990**, *247*, 2–5. [CrossRef]
48. Matias, I.; Morgado, J.; Gomes, F.C.A. Astrocyte Heterogeneity: Impact to Brain Aging and Disease. *Front. Aging Neurosci.* **2019**, *11*, 59. [CrossRef]
49. Allen, N.J.; Barres, B.A. Glia—More than Just Brain Glue. *Nature* **2009**, *457*, 675–677. [CrossRef]
50. Araque, A.; Carmignoto, G.; Haydon, P.G.; Oliet, S.H.R.; Robitaille, R.; Volterra, A. Gliotransmitters Travel in Time and Space. *Neuron* **2014**, *81*, 728–739. [CrossRef]
51. Volterra, A.; Liaudet, N.; Savtchouk, I. Astrocyte Ca2+ Signalling: An Unexpectedunexpected Complexity. *Nat. Publ. Gr.* **2014**, *15*, 327–335. [CrossRef]

micromachines

MDPI

Supplementary Information: Micropatterning of Substrates for the Culture of Cell Networks by Stencil-Assisted Additive Nanofabrication

Anita Previdi [1], Claudio Piazzoni [1], Francesca Borghi [1], Carsten Schulte [1], Leandro Lorenzelli [2], Flavio Giacomozzi [2], Alessio Bucciarelli [2], Antonio Malgaroli [3], Jacopo Lamanna [3], Andrea Moro [3], Gabriella Racchetti [3], Alessandro Podestà [1], Cristina Lenardi [1] and Paolo Milani [1,*]

[1] CIMaINa and Dipartimento di Fisica, Università degli Studi di Milano, Via Celoria 16, 20133 Milano, Italy; anita.previdi@unimi.it (A.P.); claudio.piazzoni@unimi.it (C.P.); francesca.borghi@unimi.it (F.B.); carsten.schulte@unimi.it (C.S.); alessandro.podesta@unimi.it (A.P.); cristina.lenardi@unimi.it (C.L.)

[2] Center for Materials and Microsystems (CMM), Bruno Kessler Foundation (FBK), via Sommarive 18, 38123 Trento, Italy; lorenzel@fbk.eu (L.L.); giaco@fbk.eu (F.G.); bucciarelli@fbk.eu (A.B.)

[3] Center for Behavioral Neuroscience and Communication (BNC), Università Vita-Salute San Raffaele, Via Olgettina 58, 20132 Milano, Italy; malgaroli.antonio@unisr.it (A.M.); lamanna.jacopo@hsr.it (J.L.); andrea.moro@unimi.it (A.M.); racchetti.gabriella@hsr.it (G.R.)

* Correspondence: paolo.milani@mi.infn.it

Citation: Previdi, A.; Piazzoni, C.; Borghi, F.; Schulte, C.; Lorenzelli, L.; Giacomozzi, F.; Bucciarelli, A.; Malgaroli, A.; Lamanna, J.; Moro, A.; et al. Micropatterning of Substrates for the Culture of Cell Networks by Stencil-Assisted Additive Nanofabrication. *Micromachines* **2021**, *12*, 94. https://doi.org/10.3390/12010094

Received: 2 January 2021
Accepted: 13 January 2021
Published: 18 January 2021

AFM Analysis for the Assessment of Substrates and Anti-Fouling Treatment Protocol

Our approach requires glass substrates with low roughness, in order not to affect the nanostructured zirconia film roughness. We carried out an AFM roughness analysis on different commercial glass substrates, whose final surface polishing may differ, in order to select substrates with a roughness value below 1 nm.

Figures S1a,b show AFM images of two different commercial glass coverslips (Imglas and Zeus) with very different surface morphologies. Imglas coverslips (a) do not show significant modulations in terms of surface roughness on the scale of 2 nm and they have an overall roughness corresponding to 0.2 nm, whereas Zeus coverslips (b) have a rough appearance on the 10 nm z-scale and measurements report an overall roughness value of 4 nm. Imglas coverslips (a) were therefore selected.

The glass substrates are preliminary cleaned in an ultrasound bath (ultrasonic cleaning tank, purchased from Beta Professional tools, Sovico (MB), Italy) with an Alconox® detergent solution and then rinsed with ultrapure water (milli-Q). A further cleaning step with Piranha solution (H_2SO_4:H_2O_2 (3:1)) ensures the removal of any organic contaminant and allows the complete hydroxylation of the glass surface. Subsequently, the coverslips are thoroughly rinsed with ultrapure water and dried under pure N_2. All chemicals were purchased from Merck KGaA, Darmstadt, Germany.

After the cleaning procedure, three different anti-fouling protocols were tested for surface passivation:

(i) silanization by evaporation of dimethyldichlorosilane and subsequent deposition of Pluronic (3.5% for 1h) by drop-casting;
(ii) functionalization with the copolymer PAcrAm-g-(PMOXA, NH_2, Si) (produced by SuSoS AG 151 - Dubendorf, Switzerland [30,40]), by evaporation in static vacuum;
(iii) functionalization with the copolymer PAcrAm-g-(PMOXA, NH_2, Si), by immersion in a diluted solution (0.1 mg/mL in HEPES, pH 7.4) for 30 minutes.

The antifouling coating can influence the zirconia deposition, in particular if its roughness is not negligible with respect to the deposited film roughness.

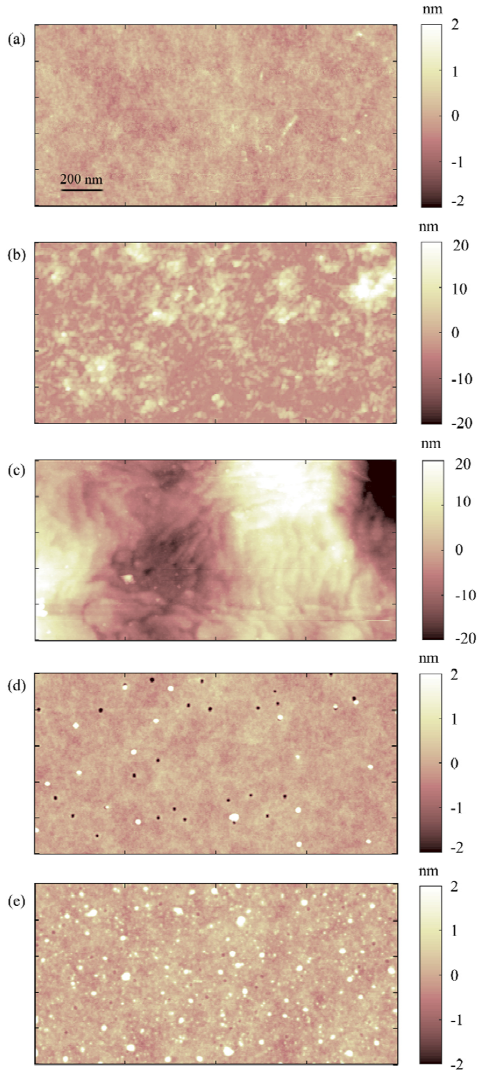

Figure 1. Morphological AFM maps (2μm × 1μm) of glass coverslips. (**a**) Pristine Imglas coverslip; (**b**) pristine Zeus coverslip; (**c**) Imglas coverslip passivated with Pluronic (method i); (**d**) Imglas coverslip passivated with evaporated copolymer PAcrAm-g-(PMOXA, NH_2, Si) (method ii); (**e**) Imglas coverslip passivated by immersion in solution of the copolymer PAcrAm-g-(PMOXA, NH_2, Si) (method iii).

In Figure S1c–e we show the AFM morphologies of coverslips treated with the three antifouling protocols described above. The pictures evidence a striking morphological difference between the glass surface treated with Pluronic (method i, Figure S1c) and those treated with PAcrAm-g-(PMOXA, NH_2, Si) (method ii and iii, Figure S1d,e). The measured R_q values reflect this difference: method (i) provides a surface with R_q ~10 nm, whereas for method (ii) and (iii) R_q ~ 0.5 nm. The copolymer PAcrAm-g-(PMOXA, NH_2, Si), assembles spontaneously in a monolayer that does not increase the surface roughness significantly. The final value of R_q measured below 1 nm can be neglected as it does not impact on the overall roughness of a nanostructured film.

The effectiveness of the antifouling properties of functionalized coverslips was confirmed by tests with PC12 cells and primary hippocampal neurons [29]. The best adhesion contrast between the patterned zirconia areas and the functionalized glass was obtained with method (iii). A time stability test of the antifouling layer performed with PC12 cells showed that the cell-repelling functionalization is effective for 4 weeks, at least.

Summary of Features of the Stencil Masks

We report a table summarizing the main features of all the different types of stencil masks tested in this work.

Table S1. Summary of the different types of masks tested in this work.

Code	Fabrication Technique	Material	Mask dimension (mm)	Thickness (μm)	Pattern type	Diameter of the dots (μm)	Center-center spacing (μm)
A	LC	Steel	14 × 15	150	dots	150	500
B	LC	Steel	14 ×15	150		150	300
C	LC	Steel	14 ×15	150		75	200
D	LC	Steel	14 ×15	150		50	100
Q10	LC	Steel	10.9 × 14	50	dots & channels (20 μm)	100	500
Q11	LC	Steel	10.9 × 14	50		100	1000
Q12	LC	Steel	10.9 × 14	50		100	1500
Q13	LC	Steel	10.9 × 14	50		250	500
Q14	LC	Steel	10.9 × 14	50		250	1000
Q15	LC	Steel	10.9 × 14	50		250	1500
Q16	PRL	Silicon	10.9 × 14	100	dots & channels (20/50 μm)	100	500
Q17	PRL	Silicon	10.9 × 14	100		100	1000
Q18	PRL	Silicon	10.9 × 14	100		100	1500
Q19	PRL	Silicon	10.9 × 14	100		250	500
Q20	PRL	Silicon	10.9 × 14	100		250	1000
Q21	PRL	Silicon	10.9 × 14	100		250	1500

Pattern Distortions

LC Steel Masks Defects

Fabrication defects in steel stencil masks can hamper the reproduction of micrometric patterns with SCBD.

Steel masks allow the experimenter to set up well defined and separate zirconia areas. In Figure S2a, a phase contrast image of nanostructured zirconia dots 150 μm wide obtained with a steel mask is reported. Figure S2 (b) shows the AFM height profile of one of the zirconia dots. The diameter of the homogeneous height area is only ~100 μm. The lateral rising widths are ~20 μm, consistent with the value expected of (17.5 ± 5.9) μm, calculated with equation (1), in the main text.

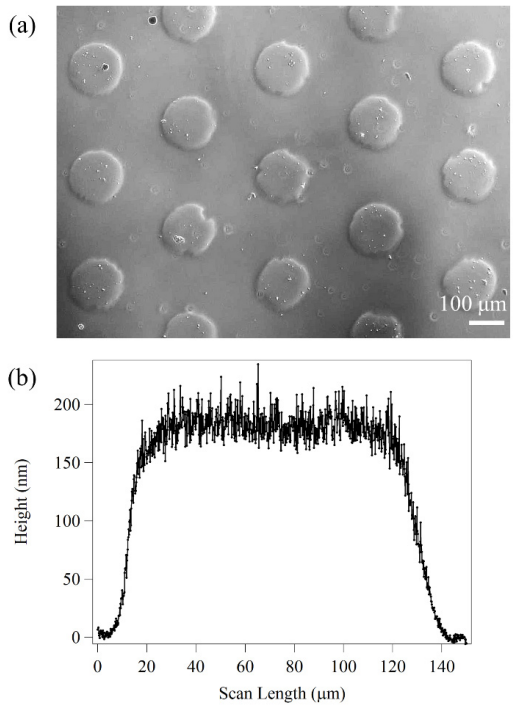

Figure S2. Nanostructured zirconia dots. (**a**) Phase contrast image of a patterned nanostructured zirconia film with 150 μm wide dots on a 300 μm hexagonal grid (mask A, Table S1). (**b**) AFM height profile map of a nanostructured zirconia dot.

With LC steel masks openings of few tens of micrometers, the effect of edge defects is disruptive. This is particularly evident, for example, in the pattern given by dots connected by 20 μm wide bridges reported in the phase contrast image of Figure S3.

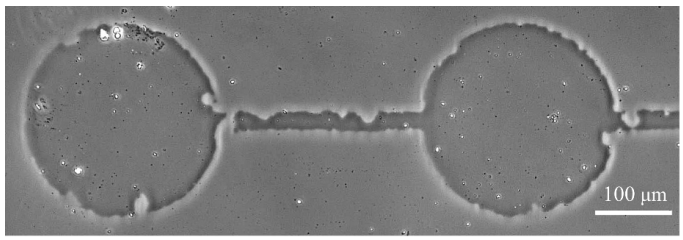

Figure S3. Ns-ZrO_x pattern reproduced with a steel LC mask with 250 μm wide dots and 20 μm wide channels (Q13, Table Scheme 1. The fabrication defects of the mask are transferred and amplified in the patterned film: the borders of the pattern feature are jagged. The micrometric bridge is not continuous since the dimension of the wiggles is comparable to its width.

Clogging—Cleaning of the Masks

The particles sticking on the edges of the openings of the masks can contribute to the distortion of the pattern, via clogging effect. This effect is particularly evident if the stencil mask pattern has features below few tens of micrometers and when the thickness of the deposit is not negligible with respect to the lateral dimensions of the openings. The latter case can be disregarded in the fabrication of zirconia films for biological application, as the typical thickness of the films deposited is below some hundreds of nanometers.

Instead, mask clogging may derive from an ineffective cleaning procedure after a deposition, if cluster aggregates get stuck into the mask openings. This effect may close them completely, compromising the pattern design.

Figure S4a,b reports scanning electron microscope (SEM) images of a poorly cleaned steel mask (ref Table S1, Q11), where the zirconia deposit blocks the mask openings. Figure S4c shows a deposited zirconia pattern obtained with poorly cleaned masks. This affects the pattern transfer: the microchannel is not continuous.

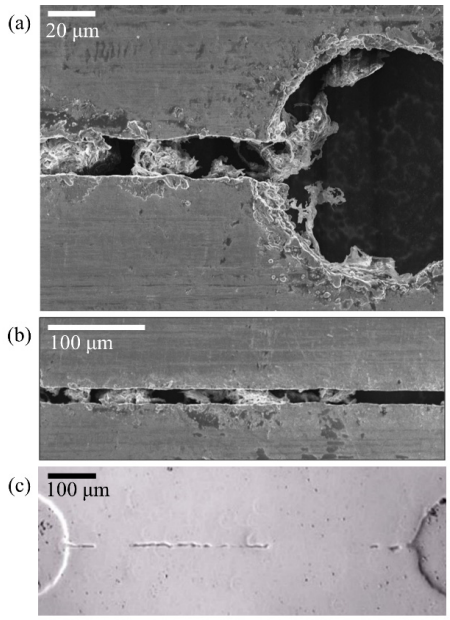

Figure 4. The clogging effect t (**a**,**b**) SEM images of LC stainless-steel masks (Q11, Table S1) not properly cleaned after a SCBD: the zirconia film portions completely block the masks opening, compromising the pattern. The images were acquired using a SEM (Zeiss Supra 40) with a 7 kV electron beam at different magnifications (10×–300×) and with a resolution of 0.5–1 nm/pixels. (**c**) Phase contrast image of a patterned zirconia film obtained with the stencil masks shown above. The result is a poor reproduction of the micrometric channel.

We found that masks can be efficiently cleaned by delicately removing the zirconia layer with wiping paper (Wypall 7300, Kimberly-Clark Professional). Possible leftover zirconia residuals can be completely removed with a 15-minute ultrasonic bath in EtOH. With this cleaning procedure the masks can be reused repeatedly for at least 20 cycles.

CHAPTER 5

Effects of the nanostructure on astrocytes

The brain physiological microenvironment plays a crucial role in regulating astrocyte structure and function. The extracellular space contains a matrix of nanoscale components secreted by the cells, i.e., proteins and polysaccharides [65, 66]. These building blocks self-assemble into a complex meshwork with a topography that is rough on the nanometric scale. As discussed in section 2.3, astrocytes are complex mechanosensitive systems that perceive the biophysical cues of the non-living tissue component, the scaffold for cellular support, and convert them into a coherent cellular program.

Achieving cell cultures where astrocytes have a physiological morphology and maintain a non-reactive state (see section 2.2.5 for the definition) represents a major challenge for brain research. It has been well documented that cellular proliferation, differentiation and development are influenced by the ECM geometry and compliance. Standard cell culture substrates constitute highly artificial environments which do not recapitulate the complexity of the *in vivo* milieu, which leads to altered gene and protein expression, cell morphology, and function [267]. The same issues are relevant for research regarding the development of novel brain implant materials. In fact, astrocyte reactivity is often caused by implantation of medical devices that can lead to the formation of the glial scar [266], that is a layer of reactive astrocytes surrounding a foreign body. The glial scar can have a toxic impact on local neurons and can also act as a physical barrier around the implant [266]. This may produce a gradual impairment of active implanted devices, like electrodes. The formation of the glial scar is not related to the chemical nature of the implant, which is chosen to be inert, rather to its biophysical properties, like stiffness or nanoscale surface morphology. It is therefore of primary importance to develop materials that have interfacial features that resemble the brain ECM and limit astrocyte reactivity [175].

A variety of biomaterials have been tested with the objective to achieve a physiological behavior of astrocytes. For example, rat astrocytes in primary cultures containing

collagen adopt a rounded morphology with short processes and express high levels of GFAP, typical of a reactive phenotype [271]. A similar rounded morphology and high levels of GFAP expression were reported for a human astrocyte cell line in gels by Rao *et al.* [301]. More examples can be found in section 2.3. All these studies highlight the difficulty in recapitulating the characteristic morphology and non-reactive state in cell culture with biomimetic substrates.

In this work, astrocytes were cultured on cluster assembled zirconia substrates fabricated with SCBD that mimic the morphological properties at the nanoscale of the brain ECM [55, 60, 135]. In this chapter we show that the interesting morphological properties of this materials make it a good candidate for the fabrication of cell culture substrates which guarantee a physiological response of astrocytes. In fact, the interaction of astrocytes with these nanotopographic features impacts on astrocyte cell shape, behavior and functioning. In particular, we demonstrate a nanoscale roughness-dependent variation in the astrocytic response in terms of proliferation, morphology, actin cytoskeleton organization and calcium signaling.

5.1 Nanoscale roughness limits astrocytes proliferation

As discussed in chapter 2.2.5, several studies have demonstrated that astrocytes reactivity is often associated with the increase of astrocytic proliferation in damaged areas of the brain when there is disruption of the blood–brain barrier [239, 302]. Also, increase in proliferation is often observed in the surroundings of implanted medical devices. This change in proliferation may be a direct consequence of the variation of the brain tissue's biophysical structure, caused by injury, disease or the presence of a foreign body [175].

We performed experiments to elucidate the impact of nanoscale morphology of the environment astrocytes are in contact with. We used cluster assembled films with controlled nanoscopic RMS roughness as cell culture substrates and evaluated the differences in cell proliferation. In particular, astrocytes were grown on ZrO_x substrates with a roughness of $10\,\mathrm{nm}$ and $15\,\mathrm{nm}$ compared to flat ZrO_x substrates (with roughness $R < 1\,\mathrm{nm}$). In these experiments, we plated cells at the same density on the different substrates and observed the progression of the cell number over 5 days. Phase contrast images taken on day 1, 3 and 5 (before medium replacement) allowed the evaluation of the variation in density over time, by performing a manual selection of the cell somas, as explained in section 3.3.4.

The results of the analysis are reported in the boxplots in Fig. 5.1. The density of cells is larger on the flat substrates compared to the nanostructured substrates, with a 1.5- and 1.6-fold increase respectively on day 3 and 5. Although the median density of cells is larger also on day 1, the observed difference becomes statistically significant only

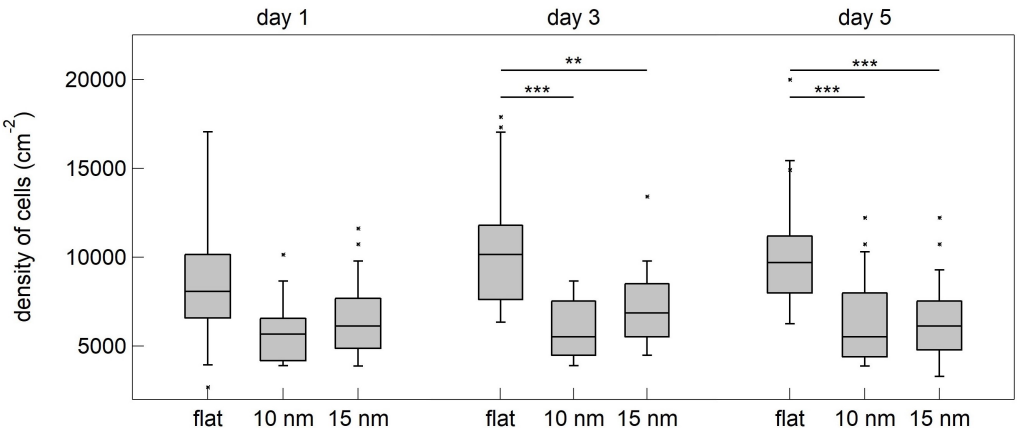

Figure 5.1: Density of cells on zirconia substrates with different nanoscale topography (flat and with roughness of $10\,\mathrm{nm}$ and $15\,\mathrm{nm}$) after 1, 3 and 5 DIV. On day 1, the median density is higher on the flat substrate, but no statistically significant difference is revealed. In the following days, a Kruskall-Wallis test followed by a multiple comparison, confirmed that the rough substrates induce a limited proliferation, compared to the flat ones. The density is in fact 1.5- and 1.6-fold higher on the flat substrates, compared to the nano-rough ones.

starting from day 3. In contrast, no statistical difference is identified in cell density on substrates of different roughness, at any stage of the culture.

As the quantification of the proliferation was based on the analysis of phase contrast images of the astrocytic culture, we cannot exclude effects of differences in cell-adhesion over the different substrates in the initial stages of the culture. In fact, this could determine an effective initial density different from the nominal, with a subsequent overall increase in density on the flat substrates, unrelated to proliferation. Nonetheless, our direct observation of the culture did not highlight significant differences in cell adhesion in the hours after seeding (we did not take images, to guarantee stable incubating conditions). In addition, only a small amount of non-viable, unattached cells was found in the cell medium on day 1. Although we did not quantify this effect, our qualitative observations indicate that the main effect determining differences in density is proliferation.

Similar results are reported in literature and imply the suppressive role of complex nanoscale topography on astrocyte proliferation *in vitro*. For example, reduced proliferation was observed in astrocytes cultured on a variety of substrates with well-defined morphological characteristics at the nanoscale, e.g. on substrates assembled by nanofibers [284, 303] or in nanofiber-based 3D culture systems [283].

Our data, coherently with previous findings, demonstrates that an extracellular environment with features defined at the nanoscale can limit the proliferation of astrocytes. This suggests that a change in brain nanoscopic topography might be one of the potential

contributors to the increase in astrocyte growth in a pathological context.

5.2 Nanostructure-induced morphological differences

Astrocytes are star-shaped glial cells, but this morphology observed *in vivo*, is not reproduced in standard cell cultures. In fact, astrocytes cultured on two-dimensional flat cover glass or tissue culture plastic display a spread morphology that closely resembles the morphology of reactive astrocytes found boarding the lesion [253].

A morphological analysis of astrocytes that were seeded on a variety of topographies was performed to investigate whether these structural features can preserve a more *in vivo*-like, physiological cell shape complexity. Astrocytes were seeded on nanostructured ZrO_x thin films with different roughness (10 nm and 15 nm) and flat zirconia as comparison. The shape of the cells was determined from the phase contrast images, taken at 1, 3 and 5 DIV. Fig. 5.2 shows a selection of exemplary phase contrast images of astrocytes on the different types of substrates at 5 DIV.

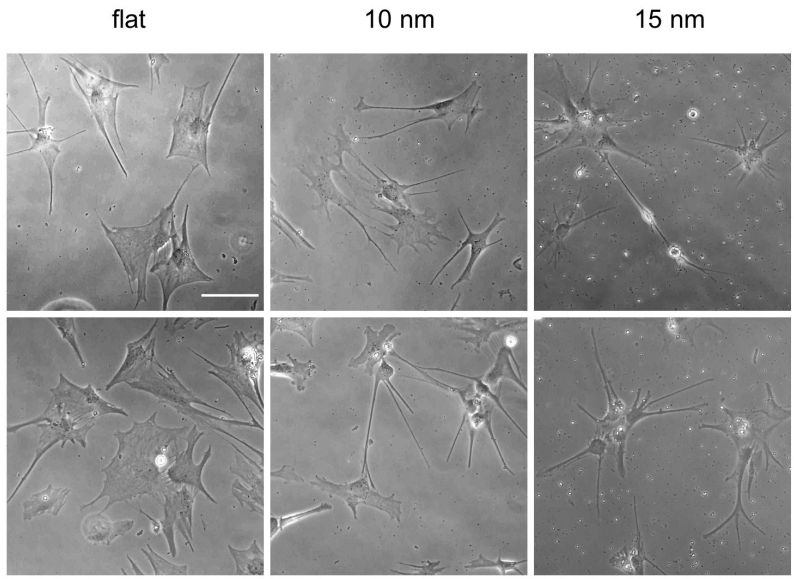

Figure 5.2: Astrocytes cultured on zirconia substrates with flat (first column) or nanorough with R = 10 nm (second column) or 15 nm (third column) surface topography after 5 DIV. The scale bar is 100 µm.

The cell morphology was evaluated as the cell area, the complexity (calculated as the number of distal processes), and the CSI, a parameter that is equal to 1 for perfectly round cells and is larger than one for more ramified or elongated morphologies [271]. In section 3.3.4, details on how the analysis was carried out and the definition of the

parameters are reported.

The astrocyte morphology with respect to substrate topography on day 1 and 5 are illustrated in the boxplots in Fig. 5.3.

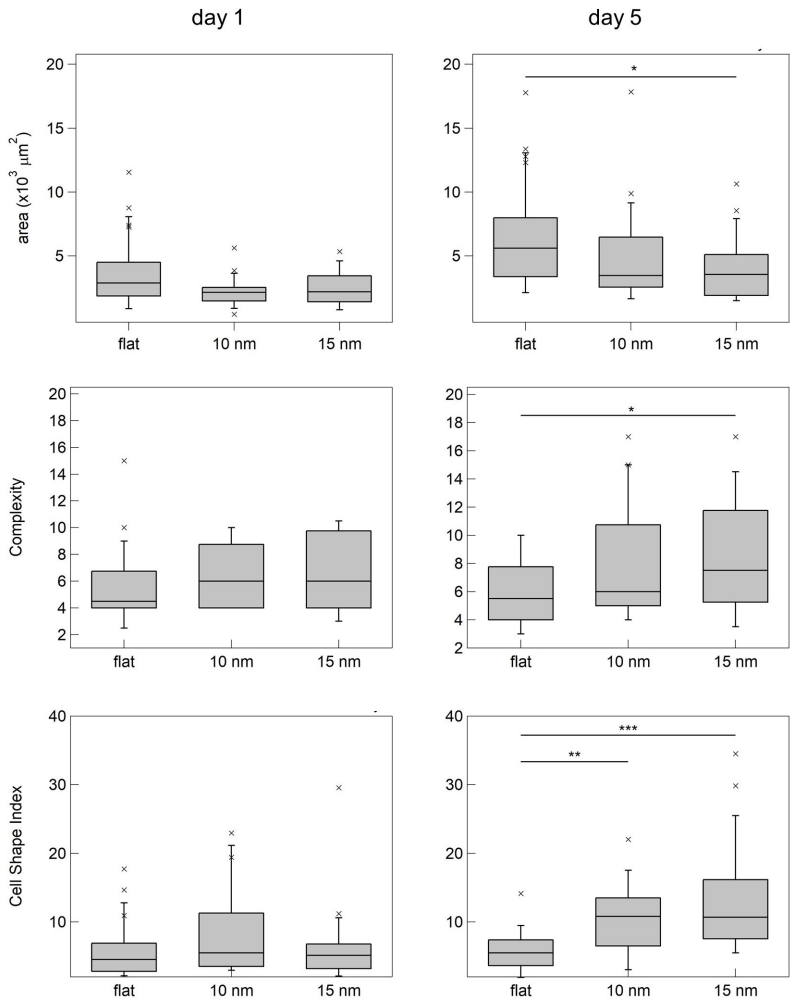

Figure 5.3: Morphology of astrocytes cultured on zirconia substrates with flat or nanorough (R = 10 nm or 15 nm) surface topography. The top boxplots display the cell area, the middle ones the complexity parameter and the bottom ones the CSI (Cell Shape Index, see section 3.3.4 for details). All parameters are analyzed after 1 and 5 DIV. On day 1, the cells have a similar shape on all substrates, the parameters taken in consideration have comparable values in all cases. On day 5, cells on the 15 nm substrate have a smaller area and higher complexity than cells on flat substrates, whereas cells on the 10 nm substrates have an intermediate value, with no statistically significant differences compared to the other substrates. The CSI parameter is significantly larger for cells on nano-rough substrates compared to the flat, testifying a more complex and ramified morphology.

On day 1, no differences are statistically significant, whereas after 5 days all the analyzed parameters display significant differences. On day 3 (not shown in the boxplots) there was an intermediate situation, with only some parameters being significantly different. When cultured on nanostructured ZrO_x substrates, astrocytes possess smaller cell areas and adopt more ramified cell shapes, as confirmed by the increased complexity and CSI parameter. Also, the distribution of the values of complexity and CSI is wider on substrates of roughness $15\,\mathrm{nm}$, testifying a greater cell morphology variability.

The changes in cell shape on nanostructures versus flat films were direct consequences of the variations in surface topography of the material. In particular, the elongated and ramified cell morphology seen on cluster-assembled films resembles more closely the typical astrocyte appearance *in vivo* [253]. This might indicate a more biomimicking nature of nano-roughness compared to flat surfaces, potentially induced via processes related to cell adhesion and the mechanotransductive machinery.

Our findings are coherent with previous studies that demonstrated the promotion of more physiologically relevant phenotypes in astrocytes by substrates assembled by nanoscopic building blocks, like nanofibers [284], nanofiber-based 3D culture systems [283], or water repellent fractal tripalmitin (PPP) surfaces [304]. Morphologies similar to those observed on nanostructured substrates, were also recapitulated by astrocytes cultured on gels, with a stiffness tuned to of the same order as brain tissue [266, 305].

5.3 Actin Cytoskeleton

The process of cellular adhesion is strongly dependent on the biophysical properties of the substrates on which the cell is grown. As discussed in section 1.0.1, the dimension and configuration of IAC change on substrates with different nanoscale roughness and/or stiffness. In turn, alterations in the IAC composition modulate cellular signaling and can induce a remodeling of the cytoskeleton and, subsequently, also the chromatin in the nucleus because they are connected by the Linker of Nucleoskeleton and Cytoskeleton complex (LINC complex). This mechanotransductive sequence can thus change the whole cellular program [61].

To get an idea whether the astrocytic interaction with nanotopographic features might affect an essential component and mediator of the mechanotransductive machinery, we characterized the actin cytoskeleton. We plated cells on flat, and nanostructured ZrO_x (surfaces with roughness $10\,\mathrm{nm}$ and $15\,\mathrm{nm}$) substrates and fixed them with paraformaldehyde after 3 days of interaction with the different substrates cell culture. We then performed a staining of the F-actin and recorded images with the 3D-SIM technique.

The fluorescence images reported in Fig. 5.4 (a), show that cells display a change in cytoskeletal organization on flat (images in the first column) and nano-rough surfaces

(images in the second column correspond to $10\,\mathrm{nm}$ surfaces, those in the third column to $15\,\mathrm{nm}$ surfaces).

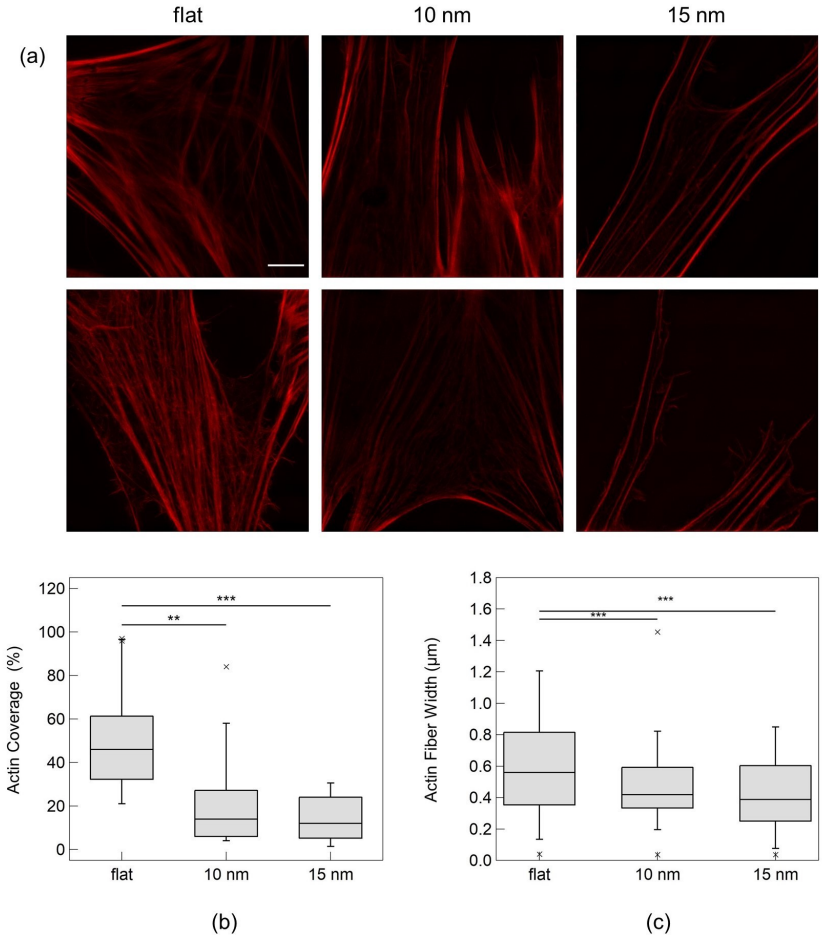

Figure 5.4: The actin cytoskeleton of astrocytes. (a) Immunofluorescence images of primary hippocampal astrocytes cultured on flat and nanostructured zirconia substrates, fixed and stained after 3 DIV. The actin cytoskeleton was stained with phalloidin, tetramethylrhodamine (TRITC)-conjugated, red). The images were taken with a 3D-SIM technique. Here we show the maximum projection of the recorded stacks. Details of actin cytoskeleton are visible in cells cultured on flat substrates first column, on $10\,\mathrm{nm}$ substrates second column, on $15\,\mathrm{nm}$ substrates column. The scale bar is 5 µm. (b-c) Analysis of the actin cytoskeleton in astrocytes plated on flat ZrO_x substrates and nanostructured substrates with R = $10\,\mathrm{nm}$ and $15\,\mathrm{nm}$. Boxplot (a) indicates the actin coverage, measured as the percentage of cell areas occupied by an actin signal higher than 25 % of the maximum signal registered. Boxplot (b) reports the width of actin fibers. Cells on flat substrates have both a higher actin intensity and thicker actin fibers.

Astrocytes cultured on flat surfaces display an intense fluorescence signal of reticulated F-actin and distinct stress fibers. In contrast, the signal is much less intense on rough surfaces and we detect fewer stress fibers.

We quantified the differences in actin organization on astrocytes on the different substrates by measuring the percentage of cell area with an actin fluorescence signal coverage higher than 25% of the maximum intensity measured over all the samples. Moreover, we extracted the width of the stress fibers (see section 3.3.4 for details on the analysis). The results are reported in the boxplot in Fig. 5.4 (b-c). In (b), we see that on flat surfaces, the actin cytoskeleton coverage has a median value of 46%, as opposed to 14% and 12% on substrates of roughness respectively $10\,\mathrm{nm}$ and $15\,\mathrm{nm}$. Astrocytes also display thicker actin fibers on flat substrates compared to the rough ones, as reported in graph (c). This data accentuates decisive differences in the architecture of the actin filaments of the cytoskeleton, in particular astrocytes grown of flat substrates form more stress fibers.

Schulte *et al.* found similar results with neuron-like PC12 cells cultivated on nanostructured ZrO_x substrates [60], they demonstrated that the formation of high order actin filament structures (e.g. stress fibers) were mainly established on flat ZrO_x. A similar trend was shown in human pancreatic β-cells, whose stress fibers were mainly detected on flat ZrO_x, but seldom formed on nanostructured ZrO_x, where actin was organized in bundles at the cell-cell contacts [146].

For PC12 cells, it was revealed that the cells interact mostly with the apical part of the asperities of the nanotopographic surfaces (with a roughness of $15\,\mathrm{nm}$), restricting the width of these adhesion sites to (53.2 ± 48.0) nm in average, compared to (90.2 ± 93.2) nm on flat surfaces [60]. Also, in [82], Chighizola *et al.* demonstrated that the nanotopography modulates the dynamics of force loading and integrin clustering at the level of single binding sites, during nascent adhesion formation. This has a direct impact on the process of formation of IACs. These structures integrate the cues deriving from the nature and configuration of the ECM and regulate concerted and complex cellular actions and signaling cascades accordingly [77, 84]. The maturation of IAC leads to the formation of multiprotein molecular machines attached to actin stress fibers [306]. Alterations in the IAC architecture modulate cellular signaling and can induce a remodeling of the cytoskeleton. Restricted adhesion sites on nanotopographic surfaces can thus directly impact the composition of the actin cytoskeleton, which in turn dictates the biomechanical and morphological properties of cells [230].

The nanostructure-induced effect on the actin cytoskeleton of astrocyte is likely to be related to the geometry of contact between the substrates and the cells. Indeed, a difference in the organization of the actin cytoskeleton was observed also in astrocytes cultured on substrates with controlled stiffness, in particular Georges *et al.* [108] reported

that on soft gels astrocytes showed fewer stress fibers. Further studies on the integrin adhesion complex maturation and the force loading might reveal the astrocyte-specific adhesion dynamics and mechanotransductive processes at the nanoscale in the future.

5.4 Calcium Activity

The cell-surface interaction has been demonstrated to impact on proliferation, cell morphology and actin cytoskeleton organization. The strong nanotopography-induced effects reported in the previous chapters prompted an analysis of substrate-dependent alterations in the astrocyte function which has not been well characterized to date. Astrocytes are known to communicate with calcium signaling, and exhibit excitability with oscillations in intracellular calcium concentrations (see section 2.2.4). As previous studies testify, calcium activity has been shown to be closely related to astrocytic morphology [232]. These observations motivated the investigation on the impact of nanostructure on calcium activity. The results of our experiments are reported below.

A characterization of the calcium activity of astrocyte cultures on flat and nanostructured (R = $15\,\mathrm{nm}$) zirconia was carried out. We registered the spontaneous calcium oscillations on several fields of confluent cells, where every astrocyte was in contact with neighboring cells.

Astrocytes on flat substrates did not display significant oscillations in intracellular calcium. In graph (a) of Fig. 5.5, several fluorescence traces, measured from ROI corresponding to different cells plated on flat substrates are reported. The fluorescence traces are mostly flat, with occasional peaks in isolated cells (not shown here). In general, no wave propagation was observed. Conversely, astrocytes on $15\,\mathrm{nm}$-ZrO_x substrates show modulations attributable to calcium influx. A selection of traces from cell ROIs on a nanostructured substrate is shown in graph (b) of Fig. 5.5. Several traces display peaks and oscillations in fluorescence intensity whose trend appears to be unrelated to that of the neighboring cells. No wave propagation events are registered, only single cell uncorrelated activity is present.

We measured the mean integrated intensity per cell on the different substrates and we extracted a significantly larger value for cells on substrates with roughness $15\,\mathrm{nm}$. The mean intensity per cell was 7.1 $\pm$ 3.7 (arb. Units) on nanostructured ZrO_x with a roughness of $15\,\mathrm{nm}$ compared to a mean intensity compatible with zero, 0.9 $\pm$ 1.2 (arb. Units) on flat substrates.

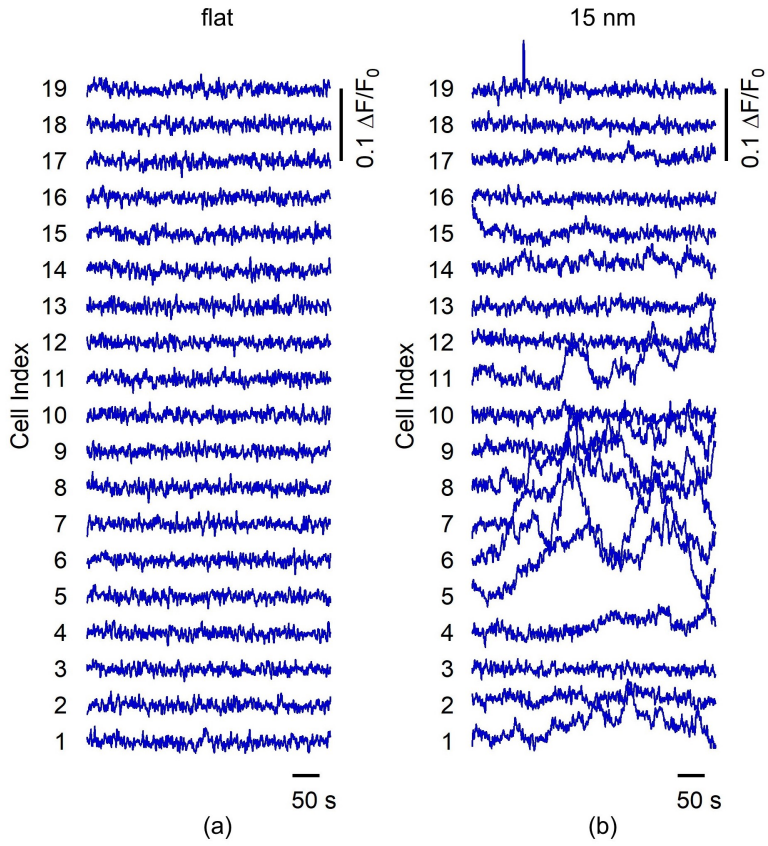

Figure 5.5: Examples of calcium fluorescence intensity traces of cells cultured on flat, graph (a), and nanostructured ZrO_x with a roughness of $15\,\mathrm{nm}$, graph (b). Different traces indicate different cells.

In general, cells on nano-rough substrates display an enhanced spontaneous, single-cell calcium activity compared to cells on flat substrates. Our findings are in line with the work of Singh *et al.* [307], who found that microgroove patterned substrates ($1\,\mu\mathrm{m}$ spacing grooves, with depths of $250\,\mathrm{nm}$ or $500\,\mathrm{nm}$) induced significantly more calcium peaks and intracellular calcium release in astrocytes.

Although preliminary, our results are relevant as calcium oscillation and wave propagation have been proved to be closely related to astrocytic morphology [199] and actin cytoskeleton organization [308–311]. The latter properties are themselves interdependent and are here shown to be impacted significantly by nanostructure.

The precise mechanism underlying spontaneous Ca^{2+} transients in astrocytes is still unclear [199]. One possible explanation is that Ca^{2+} events are triggered by stochastic Ca^{2+} entry through different pathways, like Ca^{2+}-permeable receptors, Ca^{2+} chan-

nels and Na^+/Ca^{2+} exchangers [199]. When the intracellular Ca^{2+} concentration is high enough, Ca^{2+} release via IP_3 receptors can be elicited, with the subsequent amplification and propagation of a calcium wave [231, 312–314]. It has been demonstrated that stochastic Ca^{2+} oscillations are more likely in astrocytic processes which have a high surface-to-volume ratio [315]. Hence, Ca^{2+} fluctuations are more probable in the distal processes than in the cell soma. These observations promote the idea that there may be a relationship between Ca^{2+} dynamics and astrocyte morphology. The relationship might even be both ways, meaning that morphology may impact on Ca^{2+} activity, and vice-versa. A low neuronal activity at the tripartite synapse may reduce the triggered Ca^{2+} response in astrocytes [316], which can in turn retract their processes [317].

Cotrina *et al.* [308] demonstrated that an intact actin cytoskeleton is required for calcium oscillation and propagation. In fact, they showed that cytoskeletal organization, and in particular the distribution of stress fibers, coincided temporally with the number of astrocytes engaged in calcium signaling after plating. Moreover, disruption of the actin cytoskeleton attenuated calcium signaling in stable cultures. These experiments establish that there is a close relationship between the architecture of the actin cytoskeleton and calcium propagation. We know that a certain extent of stress fiber formation is necessary for calcium signaling, but we lack details on the possible impact of the specific cytoskeletal organization. In the previous paragraph it was shown that the nanostructure changes the architecture of the actin cytoskeleton. We can speculate that a precise density of stress fibers may be required for the optimization of calcium oscillations in astrocytes, and this could be closer to the situation observed in cells on cluster-assembled substrates. A possible explanation of the relation between actin cytoskeleton and calcium activity, is that the cytoskeleton may function as a scaffold for signaling molecules [311]. Disruption of the cytoskeletal architecture provokes strong alterations in cell morphology. Since calcium signaling is closely related to the surface-to-volume ratio (i.e., the amount of plasma membrane over endoplasmic reticulum), it is reasonable to assume that cytoskeletal-associated processes are necessary to fully activate Ca^{2+} entry. This explanation is also in line with our observations. In fact, we also observe a more ramified and stellate morphology in astrocytes grown on the nanostructure.

All these results hint at complex, multilateral interactions between the cellular mechanotransductive machinery, astrocytic morphology, cytoskeletal organization and calcium activity. Future experiments are necessary to confirm these results and elucidate the mechanisms underlying calcium propagation, which might reveal an actin-related dynamics.

5.5 Conclusive remarks

Glial cells are mechanosensitive and their biological responses depend highly on extracellular biophysical features including the nature, the nanoscale morphological properties and the stiffness of their substrate.

In this chapter we have characterized the consequences of the interaction between astrocytes and nanotopography at different levels, such as cell morphology, cytoskeleton and functioning. Taken together, our results indicate that an adequate nanoscale surface structure, produced by SCBD of ZrO_x nanoparticles, has the potential to reproduce *in vitro* a phenotype of astrocytes that resembles more closely the *in vivo* situation, while flat substrates tend to cause a quite unphysiological phenotype and potentially astrocytes reactivity. We observed that the nanostructure limits cell proliferation, induces a more *in vivo*-like morphology and changes the cytoskeletal organization. The observed effects on the actin cytoskeleton strongly suggest a modulation of the mechanotransductive sequence due to the interaction with the nanotopography. Also, preliminary experiments revealed an impact in calcium signaling activity, which we speculate to be coherent with the variations in cell morphology.

The obtained data is in line with previous studies of astrocytes interacting with different biomaterials and confirms that zirconia nanostructured substrates might be an interesting tool for astrocytic cultures, to maintain a more a physiological phenotype. Proteomics and further calcium imaging analysis with increased resolution on astrocytic distal processes are needed to get a better image of the functional changes within the astrocytes induced by the nanotopographical cues. Furthermore, a deeper dissection (e.g., with respect to IAC) of the mechanotransductive impact of the astrocyte interaction with the nanostructure would be promising.

This chapter lays a solid cell biological foundation for the design of substrates for the primary brain cell culture and biomaterials that reproduce better the structural characteristics of the CNS ECM with a potential in influencing brain cell survival, growth, and differentiation. This may lead, in the future, to the development of intelligent implant coatings which prevent astrocyte reactivity and glial scar formation. Moreover, we showed that by tuning the nanoscale morphology, in principle, it might be possible to replicate the phenotype of astrocytes in different CNS pathologies. Therefore, cluster-assembled substrates have the potential to serve as platforms for the study of neural diseases or injury and, in parallel, drug testing.

In the following chapter, we add another degree of complexity to the system analyzed here. In fact, we use nanostructured substrates organized geometrically in micrometric patterns. The impact of different spatial scale geometries, at the nano- and mi-

croscale, on cells, is cumulative, but, since the nanostructure features are not related to the micro-patterns from the fabrication side, their effects can be studied independently. This additional degree of freedom can be leveraged for a new class of experiments on mechanotransduction, which were started in this thesis.

CHAPTER 6

Spatially confined astrocytic networks

Astrocytes participate in synaptic plasticity and coordinate neuronal activity as fundamental mediators [318]. They contribute actively to information processing and memory encoding in the brain [236]. According to the tripartite synapse model, described in the previous chapters, astrocytes establish a bidirectional communication with neurons, therein they sense neurotrasmitters and respond with intra- and intercellular Ca^{2+} waves. Astrocyte signaling occurs over different spatial scales, starting from the microdomains at the astrocytic processes, to the whole cell level and then over to the astrocytic network scale, at which groups of cells form functional domains. In all cases, our understanding of the mechanisms of action of astrocytic signaling and its role is still incomplete [189].

Very little is known about the impact of spatial geometric aspects of the astrocyte network on their Ca^{2+} dynamics, even though, as outlined in Chapter 3, astrocytes often have rather specific geometric arrangements *in vivo*, such as the elongated morphology along axon tracts of fibrous astrocytes, or processes that engage with blood vessels. To address this aspect, several micropatterned substrates were fabricated, as described in Chapter 5, and primary hippocampal astrocytes were cultivated on them. Cells grown on different sections of the patterns experience a different geometric environment. With the Ca^{2+} imaging technique, the spontaneous activity of patterned astrocytes were recorded and the fluorescence traces were then analyzed, paying particular attention to the potential differences among the response of cells situated in different topographic configurations.

6.1 Pattern-dependent morphological and cytoskeletal differences

The micropatterned substrates used here are composed of triplets of ZrO_x dots of a diameter of $100\,\mu m$, with an interaxial distance of $500\,\mu m$ and connected by bridges of width $50\,\mu m$ or $20\,\mu m$. Fig. 6.1 shows immunofluorescence images of the astrocytes (the nuclei

are stained in blue, the actin cytoskeleton in red) confined on micropatterned substrates. In (a) there is a full triplet of 100 µm dots with interaxial distance 500 µm connected by a bridge of width 20 µm, in (b) and (c) the close up respectively of a part of a 20 µm bridge and an isolated 100 µm dot.

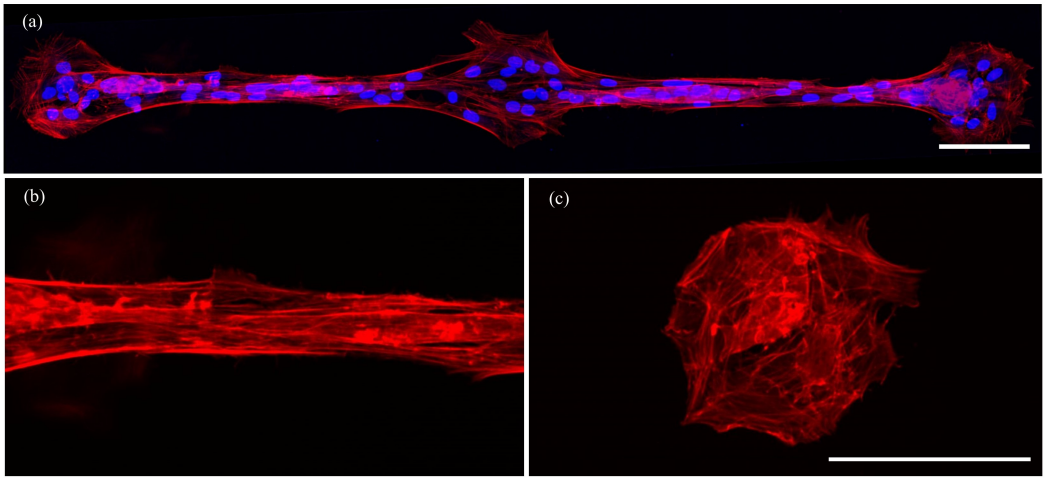

Figure 6.1: Immunofluorescence images of primary hippocampal astrocytes confined on micropatterned zirconia, fixed and stained after 3 DIV. The actin cytoskeleton was stained with phalloidin, tetramethylrhodamine (TRITC-conjugated, red) and the cell nucleus with Hoechst 33,342 (blue). In (a) there is a full triplet of 100 µm dots with interaxial distance 500 µm connected by a bridge of width 20 µm, in (b) and (c) the close up respectively of a part of a 20 µm bridge and an isolated 100 µm dot.

From Fig. 6.1 (a) it can be observed that astrocytes adhering to the bridges present an elongated morphology both of the whole cell soma and of the nucleus, which appear oriented parallel to the direction on the underlying topography. Also, as it is clearly illustrated by Fig. 6.1 (b), where only the cytoskeleton is shown, the actin components are aligned in the direction parallel to the bridge. By contrast, the cells on the dots, have no preferential orientation and they tend to occupy the entire area available, see Fig. 6.1 (c). Astrocytes on $50\,\mu\mathrm{m}$ (not shown here) are in an intermediate topographic configuration since they have enough room for spreading both in the directions parallel and perpendicular to the bridges, but in one direction they encounter no obstacles. Therefore, cells tend to elongate in the direction parallel to the bridges, but their orientation is not as well defined as on the thinner bridges.

The astrocytic networks are also organized differently on bridges or dots. In the first case, the network is anisotropic, one cell statistically will find its first neighbors either on its left or right, toward the direction of the bridge; whereas in the second case, the network has a circular shape, and cells can make connections isotropically. An analy-

sis performed on fluorescence images of astrocytes cultured on the micrometric patterns with the nuclei stained with Hoechst 33342 enabled the quantification of this property. In fact, the eccentricity of astrocyte clusters was calculated as the ratio between the width of the cluster along the axes perpendicular (w_y) and parallel (w_x) to the direction of the bridges. As Sasaki *et al.* reported in [319], astrocytes from the mouse hippocampus typically form clusters of 2 to 5 correlated cells which exhibit repeated synchronous calcium events. Several cells were therefore selected in random locations on dots or bridges. For each cell, a cluster of 5 cells was defined, by locating the first 4 nearest neighbors. The location of each cell was identified as the center of the nucleus, and w_x and w_y were taken as the distances between the two furthest cells in the direction parallel and perpendicular to the bridge. The average eccentricities of 15 clusters for each location (dot, $50\,\mu\mathrm{m}$-bridge or $20\,\mu\mathrm{m}$-bridge) selected from 6 different triplets of dots connected by bridges were calculated (the analysis was carried out on three independent samples). The results are reported in the following table.

dot	$50\,\mu\mathrm{m}$-bridge	$20\,\mu\mathrm{m}$-bridge
1.08 ± 0.23	0.80 ± 0.24	0.36 ± 0.16

Table 6.1: Eccentricity of astrocytic clusters on different locations of the micrometric patterns. The eccentricity of a cluster (i.e., 5 neighboring cells) is defined as the ratio of the distance between the two furthest cells in the direction perpendicular and parallel to the bridge.

Clusters located on dots are practically circular and they have no preferential orientation. Conversely, the eccentricity decreases for clusters on bridges of $50\,\mu\mathrm{m}$ and $20\,\mu\mathrm{m}$, thus revealing that the clusters are more and more elongated toward the direction of the bridge. This is an expected result, since astrocytes tend to occupy all the adhesive surface available and bridges can only be occupied by few cells next to each other in the direction parallel to them, effectively imposing a limit to w_y. There is in fact a chemico-physical constraint (the antifouling treatment) keeping the cells from occupying the unpatterned surface of the cell-culture substrate.

It is thus clear that the morphology and the actin cytoskeletal orientation at the single cell level and at the network level is substantially different for cell on dots and bridges.

6.2 Pattern-dependent differences in cell density

Prior to seeding the astrocytes on the patterned samples, the cells are in a solution that is thoroughly mixed and therefore can be assumed to have a homogeneous cell density. It is therefore reasonable to assume that the astrocytes land homogeneously over the surface of the culture substrate, before spreading and developing protrusions. From a

statistical point of view, the density of cells on dot and bridges should be on average the same, unless during the process of adhesion to the surface and spreading, the different geometries of the topography plays an active role in restricting or favoring the adhesion.

The density of cells on the different locations of the pattern was inferred from immunofluorescence images of astrocytes on patterns (3 independent samples). The spatial coordinates of the astrocytes were taken as the center of the nuclei, stained with Hoechst 33342. Then, the location of the cells on the different section of patterns was manually discriminated (note that cells at the border between dots and bridges were discarded from the analysis). A Kruskal-Wallis test [299] revealed a significant difference in the density of cells on dots, $50\,\mu\mathrm{m}$ bridges and $20\,\mu\mathrm{m}$ bridges. The boxplot in Fig. 6.2 shows that the median density is smallest on dots, and highest on $20\,\mu\mathrm{m}$ bridges.

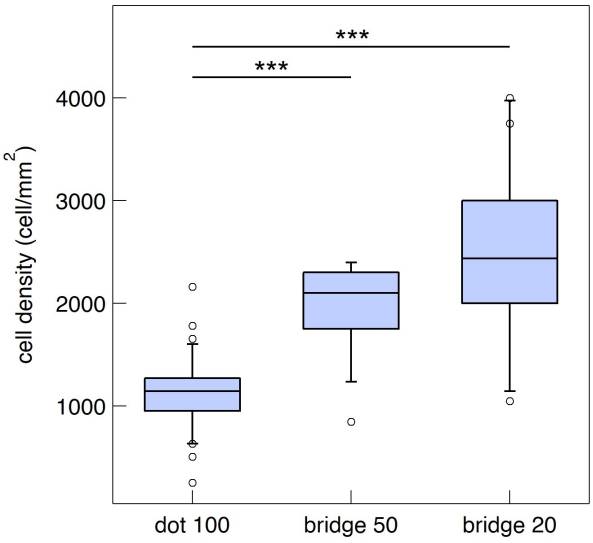

Figure 6.2: Cell density on different areas of the patterned substrates used in this work, consisting of dots of diameter $100\,\mu\mathrm{m}$ connected by bridges wide $50\,\mu\mathrm{m}$ or $20\,\mu\mathrm{m}$. The coordinates of cells were extracted from immunofluorescence images of astrocytes whose nuclei was stained with Hoechst 33342. The location of the cells on the different section of patterns was manually discriminated (cells at the border between dots and bridges were discarded from the analysis). A Kruskal-Wallis test [299] revealed a significant difference in the densities on different topographies, and a multiple comparison with Bonferroni's method confirmed a p-value < 0.05

A multiple comparison with the Bonferroni method [300] revealed that the density of cells on dots is significantly different (p-value <0.05) from the density on both bridges. On the contrary, the difference between the two bridges is not significant, although the median density increases as the bridge width decreases.

The analysis reveals a higher density on bridges, where the spatial distribution of

cells is not isotropic and their morphology appears elongated towards the direction of the bridge. Since this difference cannot be attributed to statistical reasons, it could be related to some preference of astrocytes for adhesion or replication on an elongated topography. Another option is that cells adhere homogeneously on the patterns, but they subsequently move onto the bridges, thus increasing the density. With this data, we are not able to distinguish which effect is predominant, since the analyzed images are of samples fixed at 3 DIV. For the moment being, we have no information of what happens in the hours after cells seeding. In the future, it would be promising to perform time lapse recordings to reveal the spatiotemporal dynamics of astrocyte adhesion and migration, as well as process development, on the micropatterns.

From a biological point of view, this is an interesting result since astrocytes do not have a homogeneous population in the brain and they are characterized by different shape according to their specific functionality [214, 320]. As discussed in the introduction, we know that the shape of astrocytes and astrocytic networks is strongly affected by the morphological boundaries typical of the brain regions in which the cells develop. Astrocytes or their processes often surround CNS blood vessels, synaptic areas [321] or axon tracts [191]. These brain features have similar topology (i.e. elongated structures) as the bridges in our patterns. The dimensions are also comparable - the diameter of the blood vessels in the human brain ranges e.g. between $500\,\mu\mathrm{m}$ to $8\,\mu\mathrm{m}$ [322, 323] and the typical diameter of axon fibers ranges between $0.16\,\mu\mathrm{m}$ to $9\,\mu\mathrm{m}$ [324]. The long and thin shape of the patterns' bridges may therefore be a good tool to simulate both blood vessels and axon tracts. At the same time, nanostructured micropatterns may be particularly indicated to mimic the *in vivo* environment for astrocytes as, from an ultrastructural point of view, in the context of blood vessels, it is known that the surrounding ECM, i.e. a basement membrane, has very similar nanotopographic features as the asperities produced by SCBD [325]. We can speculate that astrocyte may sense the elongated geometry of the patterns and their morphological properties at the nanoscale, recognize their physiological shape and adhere or migrate towards it.

6.3 Integrated calcium intensity

As discussed in section 5.4, it is reasonable to expect that cell morphology and actin cytoskeletal architecture may impact on calcium activity in astrocytes. Therefore, calcium imaging experiments were performed in order to investigate the calcium oscillation and propagation activity in patterned astrocytic networks.

We measured Fluo-4 fluorescent intensity of cells cultivated on micrometric patterns integrated over time and space. This quantity gives a measure of the average concentration of intracellular calcium in the astrocytes, without considering the complex dynamics

of the spontaneous calcium elevations. As discussed in the introduction in section 2.2.4, calcium activity in astrocytes can occur spontaneously, suggesting that these cells do not just provide responses to the neuronal synaptic activity but can drive it, acting as primary source [212]. A higher integrated calcium intensity may be related to a higher predisposition of the cells to act as source of astrocytic/neuronal activity.

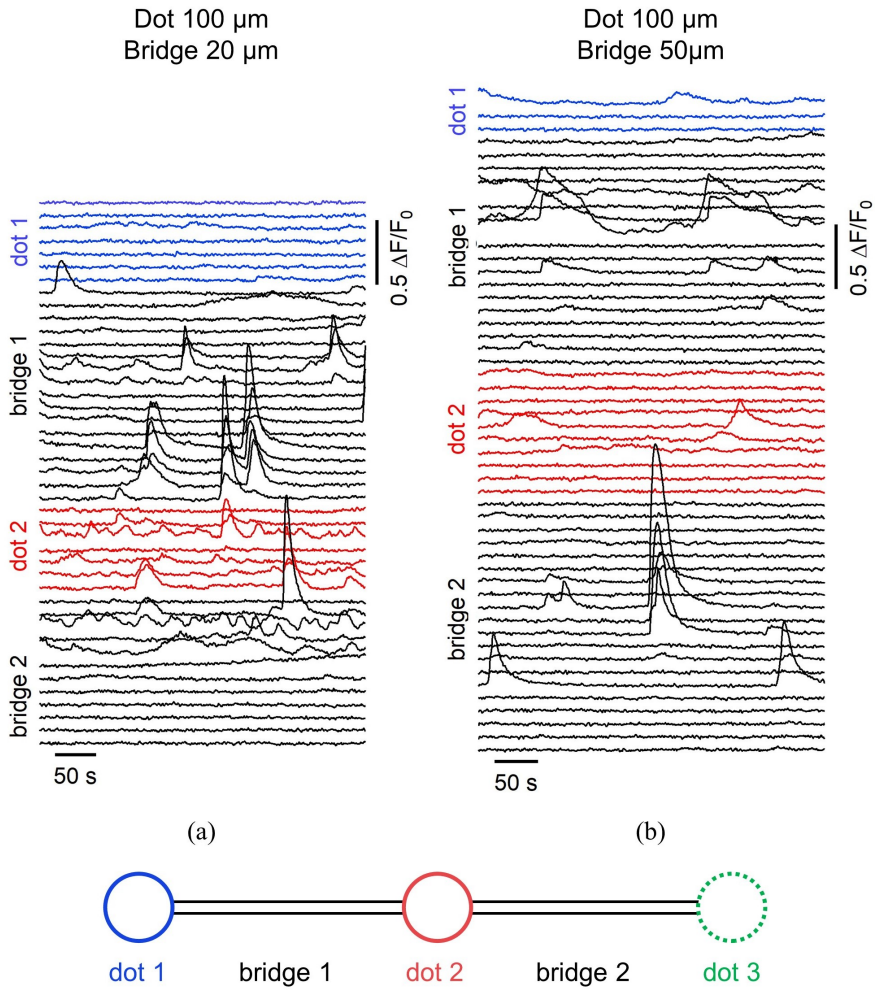

Figure 6.3: Calcium intensity traces ($\Delta F/F$) of cells cultured on micropatterns as a function of time. Different colors indicate the different location of the cells corresponding to the traces, as also highlighted by the pattern schematic reported on top of the traces: blue, red and green traces corresponds to cells on dots, black traces to cells on bridges. (a) Signals reported from cells plated on a pattern consisting of a triplet of dots with diameter $100\,\mu m$ connected by a $20\,\mu m$ bridge. (b) Signals of cells on a pattern consisting of a triplet of dots with diameter $100\,\mu m$ connected by a $50\,\mu m$ bridge.

In Fig. 6.3 the calcium intensity traces of cells cultured on micropatterns are shown, different colors indicate the different location of the cells corresponding to the traces. As the schematics of the pattern reports, blue, red and green traces corresponds to cells on dots, black traces to cells on bridges. Note that there are no green traces due to the limited field of view of the camera used, which only allowed the experimenter to record signals from a part of the pattern. In Fig. 6.3 (a), the signals reported are registered from cells plated on a pattern consisting of $100\,\mu\mathrm{m}$ dots connected by a $20\,\mu\mathrm{m}$ bridge, whereas in Fig. 6.3 (b), the pattern has a wider bridge of $50\,\mu\mathrm{m}$. It should be underlined that, because (as explained in section 3.3.3) we were interested in the network properties of the calcium activity and not in those of the single cell, the signal from a cell derives from a circular ROI with a diameter of $25\,\mu\mathrm{m}$. This ROI coincides with the cell soma and does not include the long astrocytic protrusions.

We calculated the time-integrated calcium intensity for every cell located on the patterns, and then the average integrated intensity per cell over the different areas of the patterns, i.e. bridges and dots. The result of this analysis is reported in the boxplot in 6.4 (a).

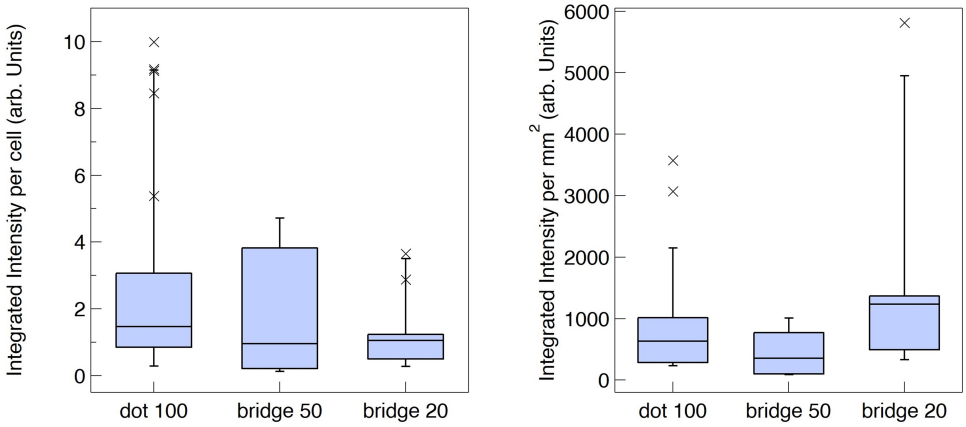

Figure 6.4: Integrated calcium intensities box plots for astrocytes on dots, $50\,\mu\mathrm{m}$- or $20\,\mu\mathrm{m}$-bridges. (a) Time-integrated calcium intensity per cell. There is no statistical difference between the different portions of pattern. (b) Time- and space- integrated calcium intensity per mm^2. Also, in this case there is no statistical difference in the different topographies. Therefore, on average, the amount of calcium influx per cell or per mm^2 is comparable for all the cell seeded on the pattern. Note that this average quantity does neither take into account the time nor the space dynamics of the calcium influx, canceling out the complexity of this phenomenon.

A Kruskal-Wallis test [299] showed no significant statistical difference for the cells in the different locations and the integrated intensities per cell are comparable in the three topographic configurations. A similar result was also obtained when a spatial integration of the calcium intensity over the whole patterned area was performed, thus taking into consideration not only the cell somas, but also the protrusions. In this case, the integrated intensity was normalized over the patterned area. The result is reported in the boxplot in 6.4 (b). This data shows that there is no difference in the integrated calcium intensity of cells cultured on different areas of pattern. On average, the amount of intracellular calcium per cell is uniform all over the pattern.

We may speculate that the integrated calcium intensity is not a good measure for evaluating the calcium activity of astrocytic networks, as it does not account for the dynamics of calcium influx. In the following paragraphs we analyzed a different parameter that includes the spatio-temporal features of calcium propagation.

6.4 Calcium waves in patterned astrocytes

A calcium wave event, as defined in section 2.2.4, is an increase in the intracellular calcium concentration which is propagated to the neighboring cells.

An example of propagating calcium waves in astrocytes seeded on patterned samples is displayed in Fig. 6.5. The image shows different frames, taken every 7.2 s, of the fluorescent signal of cells on a micrometric pattern. Here two dots with a diameter of $100\,\mu\mathrm{m}$ are connected by a $20\,\mu\mathrm{m}$ bridge. With the colormap chosen for this representation, the blue corresponds to the lowest fluorescence registered (i.e. lack of calcium), yellow to the maximum (highest concentration of calcium). Thus, the area unoccupied by cells is blue, cells with a physiological content of calcium have a low fluorescence level that is mapped to green, whereas cells with a high calcium concentration are yellow. Starting from the second frame, there is an increase in the calcium concentration of a few cells near the dot on the right, which then propagates to a few surrounding cells in the following frames.

A quantification of the number of calcium wave events occurring in cells located on bridges or dots on patterned substrates was carried out. The analysis was performed on the cell calcium traces extracted from the fluorescence videos. For each cell, we extracted the position coordinates and the times corresponding to the half-height of the calcium elevation peaks. The details of the analysis are reported in chapter 3.3.5.

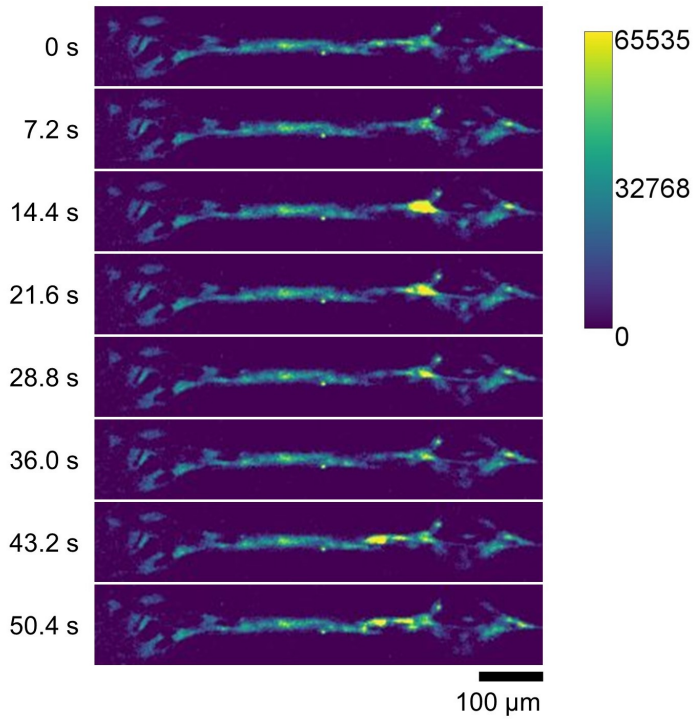

Figure 6.5: Calcium fluorescence image of a calcium wave spreading among cells plated on a micrometric pattern (dots of diameter $100\,\mu\mathrm{m}$ with an interaxial distance of $500\,\mu\mathrm{m}$ and a connecting bridge wide $20\,\mu\mathrm{m}$). The 8 different images represent different time instants, separated by 7.2 s long intervals. The colormap allows the reader to distinguish between areas with a higher calcium concentration, reported in yellow, as the bar indicates . Areas with a low concentration of calcium are reported in blue. Note that the color scale represents the Fluo-4 intensity as $\Delta F/F$, therefore it is in arbitrary units. Starting from the second frame, we can observe an increase in the calcium concentration of a few cells near the dot on the right, which then propagates to a few surrounding cells in the following frames.

Based on the current knowledge about intercellular calcium propagation, we made a few assumptions to provide an analytical definition of a calcium wave. Experimentally observed calcium waves in cultured astrocytes and slices have a velocity of propagation between 15-27 µm/s and a maximal propagation range of 200-350 µm [295–298].

Here, a calcium wave event is defined as the subsequent calcium elevations occurring in cells with a mutual distance $< 350\,\mu\mathrm{m}$ and within a time interval of $23\,\mathrm{s}$, which corresponds to the time needed to travel $350\,\mu\mathrm{m}$ at the minimum velocity of 15 µm/s. Calcium wave events that traveled at a velocity $>$ 27 µm/s were excluded. The first cell displaying a calcium elevation represented the source cell from which the calcium

wave started. We made the assumption that the calcium wave could only travel radially away from the source [222]. The subsequent cells responding were taken as secondary sources which could propagate signals radially away from the primary source. Since calcium waves can be propagated both intercellularly via exchange of molecules through gap-junctions but also extracellularly by diffusion of ATP (see section 2.2.4), we assumed that also the non-nearest neighbors could exchange signals. A schematic representation of a few astrocytes propagating signals is reported in Fig. 6.6.

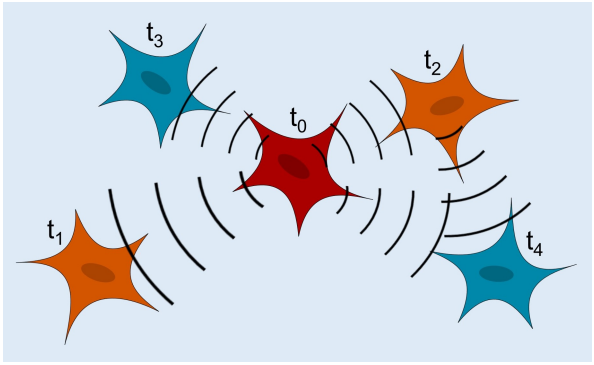

Figure 6.6: Schematics of a calcium wave propagation in neighboring astrocytes. The red cell is the source which increases its calcium content at t_0. Then the orange cells respond at t_1 and t_2. We assumed that the cell responding at t_1 cannot backpropagate the signal to the blue cell that has a calcium elevation at t_3. Instead, the orange cell responding at t_2 can propagate its signal to the blue cell responding at t_4, as the signal travels forward, away from the primary source. In this model, the blue cell with a calcium elevation at t_4 can be stimulated by both the primary source (red cell) or the secondary source (orange cell on the right).

The source cell is depicted in red and increases its calcium content at t_0, then the two orange cells respond at t_1 and t_2. The cell responding at t_1 cannot propagate the signal to the blue cell that has a calcium elevation at t_3 as it would be a backpropagation towards the main source, a process we assumed to be irrelevant for our analysis. Instead, the orange cell responding at t_2 can propagate its signal to the blue cell responding at t_4, as the signal travels forward, away from the primary source. In this model, the calcium elevation occurring at t_4 performed by the blue cell on the right can be elicited by both the primary source (red cell) or the secondary source (orange cell on the right).

With this definition of calcium waves, we could single out the calcium wave events taking place at cells occupying the micrometric patterns. This procedure was carried out with a custom MATLAB script. Then a classification of the calcium waves events with respect to the specific locations (dots or bridges) at which they took place was performed manually. We analyzed the astrocyte calcium traces extracted from several videos (at least 4 per topography type) recorded from 3 independent samples.

In Fig. 6.7 we report a graph with a series of traces extracted from cells on dots connected by $20\,\mu\mathrm{m}$-bridges, where the different colors indicate different locations on the pattern. The gray bars highlight the time intervals in which calcium waves take place, which can be recognized as the groups of intensity peaks on different cell traces.

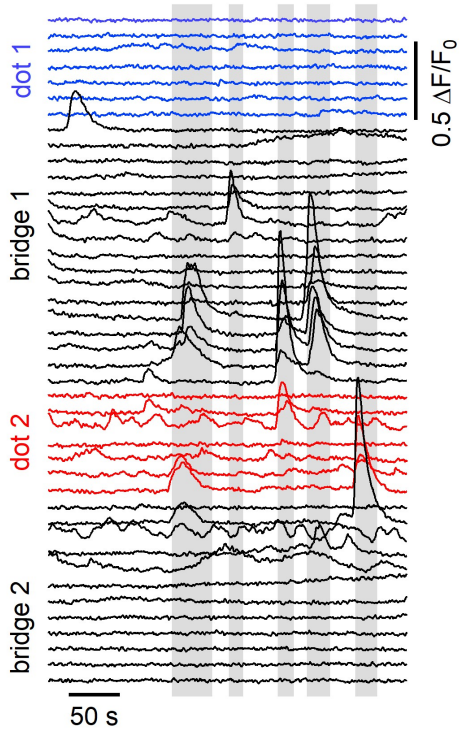

Figure 6.7: Calcium intensity traces ($\Delta F/F$) of cells cultured on micropatterns as a function of time. Different colors indicate the different location of the cells corresponding to the traces. Here the pattern consists of a triplet of dots with diameter $100\,\mu\mathrm{m}$ connected by a $20\,\mu\mathrm{m}$ bridge. The gray bars highlight the calcium wave events, which can be recognized as the groups of intensity peaks on different cell traces. The calcium elevations that are not highlighted by the gray bars are calcium oscillations which remained confined in a single cell, without spreading.

We can see that calcium elevations occurring on isolated traces are not considered calcium waves as they take place at the single cell. Some cells display also repetitive calcium elevations at frequencies of the order of tens of mHz, which can be classified as intracellular calcium oscillations, and they are not comprised in the calcium wave classification.

The density of calcium wave events per cell on dots, $50\,\mu\mathrm{m}$- and $20\,\mu\mathrm{m}$-bridges was

defined as

$$d_e = \sum_{i=0}^{N_e} \frac{n_i}{N} \tag{6.1}$$

where N_e is the total number of events registered on the part of the pattern taken into consideration, N the total number of cells occupying it and n_i is the number of cells involved in the i-th calcium wave event. This definition allows to account for a high number of calcium events or an elevated number of cells participating in events, thus we can say that a high d_e corresponds to more active cells, apt to the propagation of calcium. d_e was calculated for every video analyzed. The results of the analysis are reported in the boxplot in Fig. 6.8.

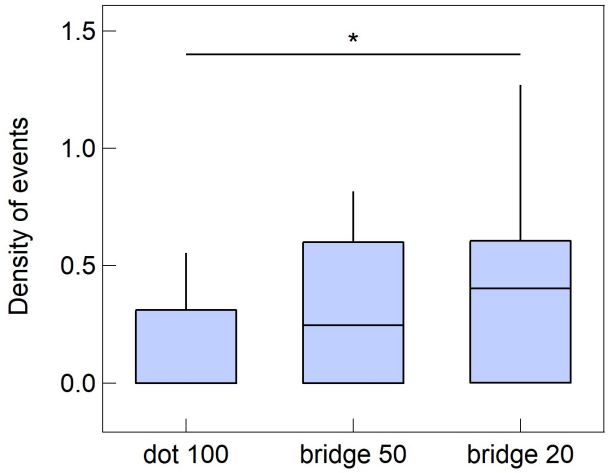

Figure 6.8: Density of calcium events as defined in the main text, for cells located on different areas of the patterned substrates, consisting of dots of $100\,\mu\mathrm{m}$ diameter connected by bridges with a width of either $50\,\mu\mathrm{m}$ or $20\,\mu\mathrm{m}$. A Kruskal-Wallis test [299] revealed that there is a statistically significant difference between the density of events per cell in the different pattern locations. Cells on $20\,\mu\mathrm{m}$-bridges conduct on average more calcium waves than cells on dots, with a significance level $p < 0.1$ (calculated with a multiple comparison exploiting Bonferroni's method [300]). In contrast, cells on bridges of different width do not display significant differences in the dynamics of calcium elevations.

A Kruskal-Wallis test [299] revealed that there is a statistically significant difference between the density of events per cell in the different pattern locations. In particular, cells on $20\,\mu\mathrm{m}$-bridges conduct on average more calcium waves than cells on dots, with a significance level $p < 0.1$ (calculated with a multiple comparison exploiting Bonferroni's method, [300]). In contrast, cells on $50\,\mu\mathrm{m}$-bridges do not display significant differences

in the dynamics of calcium elevations, compared to cells on $20\,\mu\mathrm{m}$-bridges or dots. Once again, these cells have an intermediate behavior between cells on dots and on thinner bridges. We may speculate that a difference in the calcium activity, and in particular the ability to propagate calcium waves may be related to the astrocytic network level of gap-junctional coupling determined by different topologies. A map of how astrocytes are connected by gap-junctions has not yet been reconstructed. There is evidence that astrocytic networks are organized in a complex manner, with a controlled and variable number of connections, depending on the particular brain region [326]. In certain brain structures characterized by particular anatomo-functional compartments, the shape of astrocytic circuits is dictated by functional units of neurons (such as in the somatosensory cortex [327] or the olfactory bulb [328]). Elsewhere, such as in the cortex or the hippocampus [233], it is the pattern of expression of connexins which determines the shape. So far, the functional relevance of this complex connectivity patterns or how it could impact on calcium activity has not been clarified [329]. In this framework, computational approaches revealed a direct impact of network topology and calcium wave propagation, in the context of simulated astrocyte ensembles. Dokukina *et al.* [330] simulated a simple system of less than five cells in 2D, with the main communicating mechanism of IP_3 diffusion through gap-junctions. They showed that in these cell networks, the variation in the spatial configuration of astrocytes determines different calcium responses. In particular, they identified as main parameters the number of gap-junction per cell and the number on nearest neighbors. Consistent results were also found in 3D simulated astrocytic networks by Lallouette *et al.* [331], whose predictions hinted that calcium wave propagation is favored in circuits that are sparsely coupled by gap-junctions and when cell coupling at short distances are favored. An experimental element in favor of this findings is that intracellular calcium waves were far more frequently observed in cell-cultures than in slices or *in vivo* experiments [222]. In fact, a bidimensional geometry imposes necessarily a lower cell-cell coupling compared to 3D cultures.

Our results agree with these computational models. In fact, the micropatterned substrates used in this work effectively impose limitations in the number of nearest neighbors a cell can have. Astrocytes on bridges, in particular the thinner ones, will statistically connect to fewer cells than astrocytes organized on larger pattern features, such as dots.

Another hypothesis is that cell morphology represents a further factor that may contribute the increased calcium wave propagation events in cells on thin bridges. Recent evidence from Wu *et al.* [312] shows that spontaneous calcium events appear more frequently in distal astrocytic processes, where the surface-to-volume ratio of the cells is higher. In fact, these spontaneous events are initiated by a stochastic entry of Ca^{2+}

through the plasma membrane, so areas of cells where a limited volume of cytosol is exposed to a larger surface of membrane are more likely to undergo calcium waves. In this work, astrocytes on bridges have an elongated shape as they can only expand in the direction parallel to the bridges, therefore they present a higher surface-to-volume ratio compared to the astrocytes that can spread isotropically. This may have an impact in increasing the probability of initiation of a calcium event in cells on bridges. Also, as discussed in section 5.4, there is evidence that the organization of an intact actin cytoskeleton is necessary for calcium propagation in astrocytes [308]. We have shown that in cells on patterns and specifically on microbridges, the actin fibers orientate parallel to the direction of the bridge. It would be interesting to further investigate if this architecture may create a favorable setting for calcium propagation, and whether not only the number and distribution of actin fibers impacts on calcium signaling, see [308], but also their spatial and geometric configurations.

6.5 Summary

The micropattern used in this work allow an investigation of astrocytic properties in an *in vivo*-like environment, both from the point of view of the nanoscopic morphology and that of the micrometric geometrical architecture. The results discussed in this chapter highlight numerous interesting features that astrocytic networks acquire on nanostructured micropatterned substrates.

We observed that the astrocytes populate bridges with a higher density and that the morphology of the cells and their actin cytoskeleton organization depend on the geometric shape of the pattern underlying them. In particular cells on bridges have an elongated shape with actin fibers parallel to the bridge, whereas cells on dots have a more isotropic morphology, with no preferential orientation of the actin fibers. In addition, the astrocytic networks, here defined as groups of 5 cells, have a completely different shape depending on their position on the patterns: networks on bridges have a much lower eccentricity compared to those on dots. We know from the literature that all these morphological and spatial attributes may play a crucial role in determining the communication properties of the astrocytic networks.

Here, Ca^{2+} wave signaling in astrocytic networks has been shown to be influenced by the spatial organization of cells thanks to a comparison of the activity of cells on dots or bridges. Indeed, our observations suggest that cells on bridges may be more likely to propagate calcium waves compared to those on dots. Further work would be required to investigate how varying the pattern shape may impact on Ca^{2+} signaling. This could be easily achieved thanks to the versatility of the stencil-assisted fabrication technique that was exploited in this thesis. By changing the stencil masks, we can in principle reproduce

any design that mimics the anatomy of interest (within the technically possible resolution). Moreover, a robust technique for the selective stimulation of astrocytes should be adopted, in order to characterize the propagation of stimulated calcium waves, and not only the spontaneous activity. In fact, the possibility to create astrocytic hubs of different dimensions and shapes may lead to the experimental determination of how Ca^{2+} activity in an isolated cell influences neighboring cells and how these interactions scale to the ensemble Ca^{2+} activity in an astrocyte network

Altogether, our findings hint that micropatterned substrates with nanostructured features represent an invaluable tool for the analysis of astrocytes. The possibility to reproduce *in vitro* networks with anatomically realistic shapes while providing an ECM-like substrate that allows cells to develop a more physiological or pathological phenotype, depending on the choice of the experimenter, opens the route to a variety of experiments for the understanding of the role of astroglia in brain functioning or disease, starting from the mechanisms underlying multiscale communication in networks of astrocytes and astrocytes and neurons e.g. in the context of the tripartite synapse. These could furthermore be used to better understand the role of mechanotransductive processes in healthy and pathological astrocytes

CHAPTER 7

Conclusions

The challenges in creating cultures with controlled topology and in which cells maintain their *in vivo*-like phenotype are manifold. Engineering physiologically relevant brain cell networks requires the precise placement of cell bodies in an organized manner while providing the appropriate biophysical cues typical of the native ECM.

In this work, I employed an additive nanofabrication and micropatterning technique to produce substrates for cell culture aiming at this goal. The films were produced with SCBD by assembling micropatterns of zirconia clusters on glass substrates, previously treated to be cell repulsive [332]. The cluster-assembled films have a surface morphology that mimics the nanoscale features of the ECM [61], with a roughness that can be tailored to provide different topographic signals, according to the experimental requirements. The strength of this approach resides in the fact that the control on the nanoscale properties of the films can be combined with the possibility to limit cell adhesion to predetermined substrate areas arranged in micrometric patterns. This enabled the reproduction of *in vitro* cell networks with anatomically or functionally relevant geometrical shapes.

In spite of the technical difficulties, solid fabrication protocols were developed to obtain patterns with controlled topographic features both at the nanoscale (surface root mean squared (RMS) roughness) and at the microscale (micrometric patterns). We analyzed the limiting factors of the procedures, proposing practical solutions to achieve the resolution and micropattern topologies needed. Up to now, micrometric features as small as few tens of micrometers can be obtained, but, with simple hardware modifications, the resolution can be further improved.

Starting from the findings of previous studies on the mechanotransductive effects of the nanostructure on neuronal cell development [55, 59, 60, 135–137], we used cluster-assembled substrates to perform functional studies on astrocytes. These are a particular type of brain cells that have been lately recognized as active players in brain signaling, with direct implications in neural activity and the development of cognitive functions.

Astrocytes are highly adhesive and adaptive cells [21, 181, 333] that perceive the biophysical cues of the microenvironment surrounding them via mechanotrasductive processes and participate in tissue remodeling in the physiological or pathological context [175].

Astrocytes were cultured on zirconia cluster-assembled micropatterned substrates, and different effects of the interaction between astrocytes and nano- and microscale topography were analyzed, including proliferation, cell morphology, cytoskeletal architecture and calcium activity. We showed that nanostructured substrates favor the development of astrocytes with morphological features similar to those found *in vivo*, compared to cells grown on flat substrates. At a different length scale, also the micrometric architecture of the cultures was shown to impact on cell morphology and behavior. Calcium wave signaling was demonstrated to be more effective in cells forming elongated clusters with dimension in the same range of blood vessels or axon fibers. This result was argued to be coherent with the observed morphological and cytoskeletal variations. Altogether, the findings of this multiscale analysis constitute a consistent whole and provide novel insights on the mechanosensitivity of astrocytes to the nano- and micro-topographic cues of the cellular microenvironment, while highlighting the crucial role of the biophysical properties of the growth scaffolds to direct brain cell behavior.

Nanostructured micropatterned substrates have proven to be powerful tool for the investigation of the relation between the electrical or chemical signaling among brain cells. A natural continuation of this work would be to perform similar experiments with neurons or even combined networks of neurons and astrocytes. The capability to predetermine *a priori* the network topology and engineer circuits of cells that behave similarly to the *in vivo* situation paves the way to the realization of *in vitro* alternative and complementary options to animal models and brain slices, for studying the crosstalk between different brain cells in a pathological or physiological context. A wealth of knowledge could be drawn from the investigation of fundamental spatiotemporal properties of neuro-glial communication carried out with a bottom-up approach in a controlled environment, without being hindered by the surrounding noise of dense cellular tissues.

To conclude, I want to highlight that this thesis is an example of how the contamination between nano- and microfabrication techniques with neurobiology can have a positive impact on scientific research on many levels, from fundamental studies to medical applications. The possible outcomes of this fruitful collaboration are manifold and versatile. This work contributes in setting the foundation for future applications, ranging from the engineering of smart prosthetic materials, to the development of brain-on-chip devices or neural drug testing platform and interfaces [9, 35, 179, 180].

Acronyms

PMCS pulsed microplasma cluster source

MEMS micro-electromechanical systems

SAP stencil-assisted patterning

PRL photo-resist lithography

AFM atomic force microscope

CIMaINa Interdisciplinary Centre for Nanostructured Materials and Interfaces

RMS root mean squared

YAP yes-associated protein

ECM extra-cellular matrix

GFAP glial fibrillary acidic protein

CNS central nervous system

CSPG chondroitin sulfate proteoglycan

ROI regions of interest

DIV days *in vitro*

SCBD supersonic cluster beam deposition

CSI cell shape index

IAC integrin adhesion complexes

CPU central processing units

SEM scanning electron microscopy

Bibliography

1. Seok Jeong, D., Kim, I., Ziegler, M. & Kohlstedt, H. Towards artificial neurons and synapses: a materials point of view. *RSC Advances* **3,** 3169 (2013).
2. Sengupta, B. & Stemmler, M. B. Power Consumption During Neuronal Computation. *Proceedings of the IEEE* **102,** 738–750 (2014).
3. Sporns, O., Tononi, G. & Kötter, R. The Human Connectome: A Structural Description of the Human Brain. *PLOS Computational Biology* **1,** e42 (2005).
4. Kandel, E. *et al. Principles of Neural Science, Fifth Edition* (McGraw-Hill Education, 2013).
5. Neftci, E. O. Data and Power Efficient Intelligence with Neuromorphic Learning Machines. *iScience* **5,** 52–68 (2018).
6. Lerner, T., Ye, L. & Deisseroth, K. Communication in Neural Circuits: Tools, Opportunities, and Challenges. *Cell* **164,** 1136–1150 (2016).
7. Araque, A. *et al.* Gliotransmitters Travel in Time and Space. *Neuron* **81,** 728–739 (2014).
8. Marom, S. & Shahaf, G. Development, learning and memory in large random networks of cortical neurons: lessons beyond anatomy. *Quarterly Reviews of Biophysics* **35,** 63–87 (2002).
9. Aebersold, M. J. *et al.* "Brains on a chip": Towards engineered neural networks. *TrAC Trends in Analytical Chemistry* **78,** 60–69 (2016).
10. Burr, G. W. *et al.* Neuromorphic computing using non-volatile memory. *Advances in Physics: X* **2,** 89–124 (2017).
11. Berg, A. I. *et al.* Synaptic and neuromorphic functions: General discussion. *Faraday Discussions* **213,** 553–578 (2019).
12. Jaeger, H. Exploring the landscapes of "computing": digital, neuromorphic, unconventional – and beyond. *Neuromorphic Computing and Engineering* (2021).
13. Varshney, L. R., Chen, B. L., Paniagua, E., Hall, D. H. & Chklovskii, D. B. Structural Properties of the Caenorhabditis elegans Neuronal Network. *PLOS Computational Biology* **7,** e1001066 (2011).
14. Van den Heuvel, M. P. & Sporns, O. A cross-disorder connectome landscape of brain dysconnectivity. *Nature Reviews Neuroscience* **20,** 435–446 (2019).

15. Bullmore, E. & Sporns, O. The economy of brain network organization. *Nature Reviews Neuroscience* **13,** 336–349 (2012).
16. Chen, Y., Wang, S., Hilgetag, C. C. & Zhou, C. Features of spatial and functional segregation and integration of the primate connectome revealed by trade-off between wiring cost and efficiency. *PLOS Computational Biology* **13,** e1005776 (2017).
17. Fornito, A., Zalesky, A. & Breakspear, M. The connectomics of brain disorders. *Nature Reviews. Neuroscience* **16,** 159–172 (2015).
18. Van den Heuvel, M. P. & Fornito, A. Brain networks in schizophrenia. *Neuropsychology Review* **24,** 32–48 (2014).
19. Fields, R., Woo, D. & Basser, P. Glial Regulation of the Neuronal Connectome through Local and Long-Distant Communication. *Neuron* **86,** 374–386 (2015).
20. Verkhratsky, A. & Kettenmann, H. Calcium signalling in glial cells. *Trends in Neurosciences. Special Issue: Glial Signalling* **19,** 346–352 (1996).
21. Verkhratsky, A., Rodríguez, J. J. & Parpura, V. Calcium signalling in astroglia. *Molecular and Cellular Endocrinology. Cellular Signaling in Physiology and Pathology* **353,** 45–56 (2012).
22. Parpura, V. *et al.* Glutamate-mediated astrocyte–neuron signalling. *Nature* **369,** 744–747 (1994).
23. Araque, A., Parpura, V., Sanzgiri, R. P. & Haydon, P. G. Tripartite synapses: glia, the unacknowledged partner. *Trends in Neurosciences* **22,** 208–215 (1999).
24. Nedergaard, M. Direct signaling from astrocytes to neurons in cultures of mammalian brain cells. *Science (New York, N.Y.)* **263,** 1768–1771 (1994).
25. Bargmann, C. I. Beyond the connectome: how neuromodulators shape neural circuits. *BioEssays: News and Reviews in Molecular, Cellular and Developmental Biology* **34,** 458–465 (2012).
26. Brezina, V. Beyond the wiring diagram: signalling through complex neuromodulator networks. *Philosophical Transactions of the Royal Society B: Biological Sciences* **365,** 2363–2374 (2010).
27. Harris-Warrick, R. & Johnson, B. Checks and Balances in Neuromodulation. *Frontiers in Behavioral Neuroscience* **4,** 47 (2010).
28. Levitan, I. B. Modulation of ion channels in neurons and other cells. *Annual Review of Neuroscience* **11,** 119–136 (1988).
29. Marder, E. Neuromodulation of Neuronal Circuits: Back to the Future. *Neuron* **76,** 1–11 (2012).
30. Stein, W. Modulation of stomatogastric rhythms. *Journal of Comparative Physiology. A, Neuroethology, Sensory, Neural, and Behavioral Physiology* **195,** 989–1009 (2009).
31. Taghert, P. H. & Nitabach, M. N. Peptide Neuromodulation in Invertebrate Model Systems. *Neuron* **76,** 82–97 (2012).
32. Blundell, I. *et al.* Code Generation in Computational Neuroscience: A Review of Tools and Techniques. *Frontiers in Neuroinformatics* **12,** 68 (2018).
33. Kass, R. *et al.* Computational Neuroscience: Mathematical and Statistical Perspectives. *Annual Review of Statistics and Its Application* **5** (2018).

34. Bargmann, C. I. & Marder, E. From the connectome to brain function. *Nature Methods* **10,** 483–490 (2013).
35. Tomba, C. & Villard, C. Brain cells and neuronal networks: Encounters with controlled microenvironments. *Microelectronic Engineering. Micro and Nanofabrication Breakthroughs for Electronics, MEMS and Life Sciences* **132,** 176–191 (2015).
36. Franze, K., Janmey, P. A. & Guck, J. Mechanics in Neuronal Development and Repair. *Annual Review of Biomedical Engineering* **15,** 227–251 (2013).
37. Benson, D. L., Colman, D. R. & Huntley, G. W. Molecules, maps and synapse specificity. *Nature Reviews Neuroscience* **2,** 899–909 (2001).
38. Feinerman, O., Segal, M. & Moses, E. Signal propagation along unidimensional neuronal networks. *Journal of Neurophysiology* **94,** 3406–3416 (2005).
39. Baruchi, I. & Ben-Jacob, E. Towards neuro-memory-chip: Imprinting multiple memories in cultured neural networks. *Physical Review E* **75,** 050901 (2007).
40. Renault, R. *et al.* Combining Microfluidics, Optogenetics and Calcium Imaging to Study Neuronal Communication In Vitro. *PLOS ONE* **10,** e0120680 (2015).
41. Forró, C. *et al.* Modular microstructure design to build neuronal networks of defined functional connectivity. *Biosensors and Bioelectronics* **122,** 75–87 (2018).
42. Yamamoto, H. *et al.* Impact of modular organization on dynamical richness in cortical networks. *Science Advances* **4,** eaau4914 (2018).
43. Amin, H., Dipalo, M., Angelis, F. D. & Berdondini, L. Biofunctionalized 3D Nanopillar Arrays Fostering Cell Guidance and Promoting Synapse Stability and Neuronal Activity in Networks (2018).
44. Chen, C. S. Geometric Control of Cell Life and Death. *Science* **276,** 1425–1428 (1997).
45. Falconnet, D., Csucs, G., Michelle Grandin, H. & Textor, M. Surface engineering approaches to micropattern surfaces for cell-based assays. *Biomaterials* **27,** 3044–3063 (2006).
46. Thomas, C. H., Collier, J. H., Sfeir, C. S. & Healy, K. E. Engineering gene expression and protein synthesis by modulation of nuclear shape. *Proceedings of the National Academy of Sciences* **99,** 1972–1977 (2002).
47. Wheeler, B. C., Corey, J. M., Brewer, G. J. & Branch, D. W. Microcontact printing for precise control of nerve cell growth in culture. *Journal of Biomechanical Engineering* **121,** 73–78 (1999).
48. Chang, J. C., Brewer, G. J. & Wheeler, B. C. A modified microstamping technique enhances polylysine transfer and neuronal cell patterning. *Biomaterials* **24,** 2863–2870 (2003).
49. Ricoult, S. G., Goldman, J. S., Stellwagen, D., Juncker, D. & Kennedy, T. E. Generation of microisland cultures using microcontact printing to pattern protein substrates. *Journal of Neuroscience Methods* **208,** 10–17 (2012).
50. Marconi, E. *et al.* Emergent Functional Properties of Neuronal Networks with Controlled Topology. *PLOS ONE* **7,** e34648 (2012).
51. Mecozzi, L. *et al.* Simple and Rapid Bioink Jet Printing for Multiscale Cell Adhesion Islands. *Macromolecular Bioscience* **17,** 1600307 (2017).
52. Yusof, A. *et al.* Inkjet-like printing of single-cells. *Lab on a Chip* **11,** 2447–2454 (2011).

53. Carpi, N., Carpi, N., Piel, M., Azioune, A. & Fink, J. Micropatterning on glass with deep UV. *Protocol Exchange.* ISSN: 2043-0116 (2011).
54. Carpi, N. *et al.* Micropatterning on silicon elastomer (PDMS) with deep UVs. *Protocol Exchange.* ISSN: 2043-0116 (2011).
55. Schulte, C. *et al.* Scale Invariant Disordered Nanotopography Promotes Hippocampal Neuron Development and Maturation with Involvement of Mechanotransductive Pathways. *Frontiers in Cellular Neuroscience* **10** (2016).
56. Abrams, G. A., Goodman, S. L., Nealey, P. F., Franco, M & Murphy, C. J. Nanoscale topography of the basement membrane underlying the corneal epithelium of the rhesus macaque. *Cell and Tissue Research* **299(1),** 39–46 (2000).
57. Borghi, F., Podestà, A., Piazzoni, C. & Milani, P. Growth Mechanism of Cluster-Assembled Surfaces: From Submonolayer to Thin-Film Regime. *Physical Review Applied,* 044016 (2018).
58. Borghi, F. *et al.* Cluster-assembled cubic zirconia films with tunable and stable nanoscale morphology against thermal annealing. *Journal of Applied Physics* **120,** 055302 (2016).
59. Maffioli, E. *et al.* Proteomic Dissection of Nanotopography-Sensitive Mechanotransductive Signaling Hubs that Foster Neuronal Differentiation in PC12 Cells. *Frontiers in Cellular Neuroscience* **11,** 417 (2018).
60. Schulte, C. *et al.* Conversion of nanoscale topographical information of cluster-assembled zirconia surfaces into mechanotransductive events promotes neuronal differentiation. *Journal of Nanobiotechnology* **14,** 18 (2016).
61. Schulte, C. in *Frontiers of Nanoscience* 271–289 (Elsevier, 2020).
62. Gasiorowski, J. Z., Murphy, C. J. & Nealey, P. F. Biophysical Cues and Cell Behavior: The Big Impact of Little Things. *Annual Review of Biomedical Engineering* **15,** 155–176 (2013).
63. Harris, A. K., Stopak, D. & Wild, P. Fibroblast traction as a mechanism for collagen morphogenesis. *Nature* **290,** 249–251 (1981).
64. Tajerian, M. *et al.* The hippocampal extracellular matrix regulates pain and memory after injury. *Molecular Psychiatry* **23,** 2302–2313 (2018).
65. Hynes, R. O. Extracellular matrix: not just pretty fibrils. *Science (New York, N.Y.)* **326,** 1216–1219 (2009).
66. Frantz, C., Stewart, K. M. & Weaver, V. M. The extracellular matrix at a glance. *Journal of Cell Science* **123,** 4195–4200 (2010).
67. Kim, H. N. *et al.* Nanotopography-guided tissue engineering and regenerative medicine. *Advanced Drug Delivery Reviews. Bionics - Biologically inspired smart materials* **65,** 536–558 (2013).
68. Barnes, J. M., Przybyla, L. & Weaver, V. M. Tissue mechanics regulate brain development, homeostasis and disease. *Journal of Cell Science* **130,** 71–82 (2017).
69. Walma, D. A. C. & Yamada, K. M. The extracellular matrix in development. *Development* **147** (2020).
70. Iskratsch, T., Wolfenson, H. & Sheetz, M. P. Appreciating force and shape — the rise of mechanotransduction in cell biology. *Nature Reviews Molecular Cell Biology* **15,** 825–833 (2014).

71. Chen, W., Shao, Y., Li, X., Zhao, G. & Fu, J. Nanotopographical surfaces for stem cell fate control: Engineering mechanobiology from the bottom. *Nano Today* **9,** 759–784 (2014).

72. Wang, N., Tytell, J. D. & Ingber, D. E. Mechanotransduction at a distance: mechanically coupling the extracellular matrix with the nucleus. *Nature Reviews Molecular Cell Biology* **10,** 75–82 (2009).

73. Pennacchio, F. A., Nastały, P., Poli, A. & Maiuri, P. Tailoring Cellular Function: The Contribution of the Nucleus in Mechanotransduction. *Frontiers in Bioengineering and Biotechnology* **8,** 1474 (2021).

74. Humphrey, J. D., Dufresne, E. R. & Schwartz, M. A. Mechanotransduction and extracellular matrix homeostasis. *Nature Reviews Molecular Cell Biology* **15,** 802–812 (2014).

75. Case, L. B. & Waterman, C. M. Integration of actin dynamics and cell adhesion by a three-dimensional, mechanosensitive molecular clutch. *Nature Cell Biology* **17,** 955–963 (2015).

76. Gao, Y. *et al.* The ECM-Cell Interaction of Cartilage Extracellular Matrix on Chondrocytes. *BioMed Research International* **2014,** e648459 (2014).

77. Kechagia, J. Z., Ivaska, J. & Roca-Cusachs, P. Integrins as biomechanical sensors of the microenvironment. *Nature Reviews Molecular Cell Biology* **20,** 457–473 (2019).

78. Sun, Z., Costell, M. & Fässler, R. Integrin activation by talin, kindlin and mechanical forces. *Nature Cell Biology* **21,** 25–31 (2019).

79. Wang, X. & Ha, T. Defining Single Molecular Forces Required to Activate Integrin and Notch Signaling. *Science* **340,** 991–994 (2013).

80. Paszek, M. J. *et al.* The cancer glycocalyx mechanically primes integrin-mediated growth and survival. *Nature* **511,** 319–325 (2014).

81. Gauthier, N. C. & Roca-Cusachs, P. Mechanosensing at integrin-mediated cell–matrix adhesions: from molecular to integrated mechanisms. *Current Opinion in Cell Biology. Cell Architecture* **50,** 20–26 (2018).

82. Chighizola, M. *et al.* Mechanotransduction in neuronal cell development and functioning. *Biophysical Reviews* **11,** 701–720 (2019).

83. Kong, F., García, A. J., Mould, A. P., Humphries, M. J. & Zhu, C. Demonstration of catch bonds between an integrin and its ligand. *Journal of Cell Biology* **185,** 1275–1284 (2009).

84. Winograd-Katz, S. E., Fässler, R., Geiger, B. & Legate, K. R. The integrin adhesome: from genes and proteins to human disease. *Nature Reviews. Molecular Cell Biology* **15,** 273–288 (2014).

85. Humphries, J. D., Paul, N. R., Humphries, M. J. & Morgan, M. R. Emerging properties of adhesion complexes: what are they and what do they do? *Trends in Cell Biology* **25,** 388–397 (2015).

86. Horton, E. R. *et al.* Definition of a consensus integrin adhesome and its dynamics during adhesion complex assembly and disassembly. *Nature Cell Biology* **17,** 1577–1587 (2015).

87. Panciera, T., Azzolin, L., Cordenonsi, M. & Piccolo, S. Mechanobiology of YAP and TAZ in physiology and disease. *Nature Reviews. Molecular Cell Biology* **18,** 758–770 (2017).

88. Uhler, C. & Shivashankar, G. V. Chromosome Intermingling: Mechanical Hotspots for Genome Regulation. *Trends in Cell Biology* **27,** 810–819 (2017).

89. Chan, C. E. & Odde, D. J. Traction Dynamics of Filopodia on Compliant Substrates. *Science* **322,** 1687–1691 (2008).

90. Bangasser, B. *et al.* Shifting the optimal stiffness for cell migration. *Nature Communications* **8** (2017).

91. Elosegui-Artola, A. *et al.* Force Triggers YAP Nuclear Entry by Regulating Transport across Nuclear Pores. *Cell* **171,** 1397–1410.e14 (2017).

92. Oria, R. *et al.* Force loading explains spatial sensing of ligands by cells. *Nature* **552,** 219–224 (2017).

93. Moroishi, T., Hansen, C. G. & Guan, K.-L. The emerging roles of YAP and TAZ in cancer. *Nature Reviews Cancer* **15,** 73–79 (2015).

94. Porazinski, S. *et al.* YAP is essential for tissue tension to ensure vertebrate 3D body shape. *Nature* **521,** 217–221 (2015).

95. Zhao, B. *et al.* Inactivation of YAP oncoprotein by the Hippo pathway is involved in cell contact inhibition and tissue growth control. *Genes & Development* **21,** 2747–2761 (2007).

96. Caliari, S. R. & Burdick, J. A. A practical guide to hydrogels for cell culture. *Nature Methods* **13,** 405–414 (2016).

97. Discher, D. E., Janmey, P. & Wang, Y.-l. Tissue Cells Feel and Respond to the Stiffness of Their Substrate. *Science* **310,** 1139–1143 (2005).

98. Gobaa, S. *et al.* Artificial niche microarrays for probing single stem cell fate in high throughput. *Nature Methods* **8,** 949–955 (2011).

99. Aisenbrey, E. A. & Murphy, W. L. Synthetic alternatives to Matrigel. *Nature Reviews Materials* **5,** 539–551 (2020).

100. Mendes, P. M. Cellular nanotechnology: making biological interfaces smarter. *Chemical Society Reviews* **42,** 9207–9218 (2013).

101. Dalby, M. J., Gadegaard, N. & Oreffo, R. O. C. Harnessing nanotopography and integrin–matrix interactions to influence stem cell fate. *Nature Materials* **13,** 558–569 (2014).

102. Palchesko, R. N., Zhang, L., Sun, Y. & Feinberg, A. W. Development of Polydimethylsiloxane Substrates with Tunable Elastic Modulus to Study Cell Mechanobiology in Muscle and Nerve. *PLOS ONE* **7,** e51499 (2012).

103. Vertelov, G. *et al.* Rigidity of silicone substrates controls cell spreading and stem cell differentiation. *Scientific Reports* **6,** 33411 (2016).

104. Engler, A. J., Sen, S., Sweeney, H. L. & Discher, D. E. Matrix Elasticity Directs Stem Cell Lineage Specification. *Cell* **126,** 677–689 (2006).

105. Pelham, R. J. & Wang, Y.-l. Cell locomotion and focal adhesions are regulated by substrate flexibility. *Proceedings of the National Academy of Sciences* **94,** 13661–13665 (1997).

106. Kong, H. J., Polte, T. R., Alsberg, E. & Mooney, D. J. FRET measurements of cell-traction forces and nano-scale clustering of adhesion ligands varied by substrate stiffness. *Proceedings of the National Academy of Sciences* **102,** 4300–4305 (2005).

107. Huebsch, N. *et al.* Harnessing traction-mediated manipulation of the cell/matrix interface to control stem-cell fate. *Nature Materials* **9,** 518–526 (2010).

108. Georges, P. C., Miller, W. J., Meaney, D. F., Sawyer, E. S. & Janmey, P. A. Matrices with Compliance Comparable to that of Brain Tissue Select Neuronal over Glial Growth in Mixed Cortical Cultures. *Biophysical Journal* **90,** 3012–3018 (2006).

109. Saha, K. *et al.* Substrate Modulus Directs Neural Stem Cell Behavior. *Biophysical Journal* **95,** 4426–4438 (2008).

110. Teixeira, A. I., Abrams, G. A., Bertics, P. J., Murphy, C. J. & Nealey, P. F. Epithelial contact guidance on well-defined micro- and nanostructured substrates. *Journal of Cell Science* **116,** 1881–1892 (2003).

111. Kingham, E. & Oreffo, R. O. Embryonic and Induced Pluripotent Stem Cells: Understanding, Creating, and Exploiting the Nano-Niche for Regenerative Medicine. *ACS Nano* **7,** 1867–1881 (2013).

112. Spradling, A., Drummond-Barbosa, D. & Kai, T. Stem cells find their niche. *Nature* **414,** 98–104 (2001).

113. Sun, Y., Chen, C. S. & Fu, J. Forcing Stem Cells to Behave: A Biophysical Perspective of the Cellular Microenvironment. *Annual review of biophysics* **41,** 519–542. (2021) (2012).

114. DuFort, C. C., Paszek, M. J. & Weaver, V. M. Balancing forces: architectural control of mechanotransduction. *Nature Reviews. Molecular Cell Biology* **12,** 308–319 (2011).

115. Geiger, B., Spatz, J. P. & Bershadsky, A. D. Environmental sensing through focal adhesions. *Nature Reviews Molecular Cell Biology* **10,** 21–33. (2021) (Jan. 2009).

116. Buxboim, A., Ivanovska, I. L. & Discher, D. E. Matrix elasticity, cytoskeletal forces and physics of the nucleus: how deeply do cells 'feel' outside and in? *Journal of Cell Science* **123,** 297–308 (2010).

117. Isermann, P. & Lammerding, J. Nuclear mechanics and mechanotransduction in health and disease. *Current biology: CB* **23,** R1113–1121 (2013).

118. Xie, J. *et al.* The differentiation of embryonic stem cells seeded on electrospun nanofibers into neural lineages. *Biomaterials* **30,** 354–362 (2009).

119. Lee, M. R. *et al.* Direct differentiation of human embryonic stem cells into selective neurons on nanoscale ridge/groove pattern arrays. *Biomaterials* **31,** 4360–4366 (2010).

120. Yang, K. *et al.* Nanotopographical Manipulation of Focal Adhesion Formation for Enhanced Differentiation of Human Neural Stem Cells. *ACS Applied Materials & Interfaces* **5,** 10529–10540 (2013).

121. Smith Callahan, L. A. *et al.* Directed differentiation and neurite extension of mouse embryonic stem cell on aligned poly(lactide) nanofibers functionalized with YIGSR peptide. *Biomaterials* **34,** 9089–9095 (2013).

122. Dalby, M. J. *et al.* The control of human mesenchymal cell differentiation using nanoscale symmetry and disorder. *Nature Materials* **6,** 997–1003 (2007).

123. Andersson, A.-S., Brink, J., Lidberg, U. & Sutherland, D. Influence of systematically varied nanoscale topography on the morphology of epithelial cells. *IEEE Transactions on NanoBioscience* **2,** 49–57 (2003).

124. Yim, E. *et al.* Nanopattern-induced changes in morphology and motility of smooth muscle cells. *Biomaterials* **26,** 5405–5413 (2005).

125. Gallagher, J., McGhee, K., Wilkinson, C. & Riehle, M. Interaction of animal cells with ordered nanotopography. *IEEE Transactions on NanoBioscience* **99,** 24–28 (2002).

126. Thapa, A., Webster, T. & Haberstroh, K. Polymers with nano-dimensional surface features enhance bladder smooth muscle cell adhesion. *Journal of Biomedical Materials Research - Part A* **67,** 1374–1383 (2003).

127. Boyan, B. *et al.* Titanium surface roughness alters responsiveness of MG63 osteoblast-like cells to 1α,25-(OH)2D3. *Journal of Biomedical Materials Research* **39,** 77–85 (1998).

128. Chen, W., Shao, Y., Li, X., Zhao, G. & Fu, J. Nanotopographical Surfaces for Stem Cell Fate Control: Engineering Mechanobiology from the Bottom. *Nano Today* **9,** 759–784 (2014).

129. Dang, J. & Leong, K. Myogenic induction of aligned mesenchymal stem cell sheets by culture on thermally responsive electrospun nanofibers. *Advanced Materials* **19,** 2775–2779 (2007).

130. Smith, L. A., Liu, X., Hu, J., Wang, P. & Ma, P. X. Enhancing Osteogenic Differentiation of Mouse Embryonic Stem Cells by Nanofibers. *Tissue Engineering Part A* **15,** 1855–1864 (2009).

131. Oh, S. *et al.* Stem cell fate dictated solely by altered nanotube dimension. *Proceedings of the National Academy of Sciences of the United States of America* **106,** 2130–2135 (2009).

132. Dulgar-Tulloch, A., Bizios, R. & Siegel, R. Human mesenchymal stem cell adhesion and proliferation in response to ceramic chemistry and nanoscale topography. *Journal of Biomedical Materials Research - Part A* **90,** 586–594 (2009).

133. Wegner, K., Piseri, P., Tafreshi, H. V. & Milani, P. Cluster beam deposition: a tool for nanoscale science and technology. *Journal of Physics D: Applied Physics* **39,** R439–R459 (2006).

134. Podestà, A. *et al.* Nanomanufacturing of titania interfaces with controlled structural and functional properties by supersonic cluster beam deposition. *Journal of Applied Physics* **118,** 234309 (2015).

135. Schulte, C., Podestà, A., Lenardi, C., Tedeschi, G. & Milani, P. Quantitative Control of Protein and Cell Interaction with Nanostructured Surfaces by Cluster Assembling. *Accounts of Chemical Research* **50,** 231–239 (2017).

136. Schulte, C. *et al.* Neuronal Cells Confinement by Micropatterned Cluster-Assembled Dots with Mechanotransductive Nanotopography. *ACS Biomaterials Science & Engineering* **4,** 4062–4075 (2018).

137. Chighizola, M. *et al.* Adhesion force spectroscopy with nanostructured colloidal probes reveals nanotopography-dependent early mechanotransductive interactions at the cell membrane level. *Nanoscale* **12,** 14708–14723 (2020).

138. Milani, P. & Iannotta, S. *Cluster Beam Synthesis of Nanostructured Materials* 194 pp. (1999).

139. Gleiter, H. Nanocrystalline materials. *Progress in Materials Science* **33,** 223–315 (1989).

140. Yuan, C.-N., Li, Y.-F., Sheng, Y.-J. & Tsao, H.-K. Dry nanogranular materials. *Applied Physics Letters* **98,** 144102 (2011).

141. Family, F. & Vicsek, T. s. *Dynamics of Fractal Surfaces* 500 pp. (World Scientific, 1991).

142. Family, F. & Vicsek, T. Scaling of the active zone in the Eden process on percolation networks and the ballistic deposition model. *Journal of Physics A: Mathematical and General* **18,** L75–L81 (1985).

143. Barabasi, A. L., Stanley, H. E. & Sander, L. M. Fractal Concepts in Surface Growth. *Physics Today* **48,** 68–69 (1995).

144. Manicone, P. F., Rossi Iommetti, P. & Raffaelli, L. An overview of zirconia ceramics: Basic properties and clinical applications. *Journal of Dentistry* **35,** 819–826 (2007).

145. Carbone, R *et al.* Biocompatibility of cluster-assembled nanostructured TiO2 with primary and cancer cells. *Biomaterials* **27,** 3221–3229 (2006).

146. Galli, A. *et al.* Cluster-assembled zirconia substrates promote long-term differentiation and functioning of human islets of Langerhans. *Scientific Reports* **8,** 9979 (2018).

147. Singh, A. V. *et al.* Bottom-up engineering of the surface roughness of nanostructured cubic zirconia to control cell adhesion. *Nanotechnology* **23,** 475101 (2012).

148. Cavalcanti-Adam, E. A. *et al.* Cell Spreading and Focal Adhesion Dynamics Are Regulated by Spacing of Integrin Ligands. *Biophysical Journal* **92,** 2964–2974 (2007).

149. Borghi, F., Scaparra, B., Paternoster, C., Milani, P. & Podestà, A. Electrostatic Double-Layer Interaction at the Surface of Rough Cluster-Assembled Films: The Case of Nanostructured Zirconia. *Langmuir* **34,** 10230–10242 (2018).

150. Belicchi, M. *et al.* Ex vivo expansion of human circulating myogenic progenitors on cluster-assembled nanostructured TiO2. *Biomaterials* **31,** 5385–5396 (2010).

151. Astis, S. D. *et al.* Nanostructured TiO2 surfaces promote polarized activation of microglia, but not astrocytes, toward a proinflammatory profile. *Nanoscale* **5,** 10963–10974 (2013).

152. Changede, R. & Sheetz, M. Integrin and cadherin clusters: A robust way to organize adhesions for cell mechanics. *BioEssays: News and Reviews in Molecular, Cellular and Developmental Biology* **39,** 1–12 (2017).

153. Stukel, J. M. & Willits, R. K. Mechanotransduction of Neural Cells Through Cell–Substrate Interactions. *Tissue Engineering Part B: Reviews* **22,** 173–182 (2016).

154. Park, Y. K. & Goda, Y. Integrins in synapse regulation. *Nature Reviews Neuroscience* **17,** 745–756 (2016).

155. Lilja, J. & Ivaska, J. Integrin activity in neuronal connectivity. *Journal of Cell Science* **131** (2018).

156. Kotov, N. A. *et al.* Nanomaterials for Neural Interfaces. *Advanced Materials* **21,** 3970–4004 (2009).

157. Fattahi, P., Yang, G., Kim, G. & Abidian, M. R. A Review of Organic and Inorganic Biomaterials for Neural Interfaces. *Advanced Materials* **26,** 1846–1885 (2014).

158. Sandoe, J. & Eggan, K. Opportunities and challenges of pluripotent stem cell neurodegenerative disease models. *Nature Neuroscience* **16,** 780–789 (2013).

159. Abematsu, M. *et al.* Neurons derived from transplanted neural stem cells restore disrupted neuronal circuitry in a mouse model of spinal cord injury. *The Journal of Clinical Investigation* **120,** 3255–3266 (2010).

160. Lu, P. *et al.* Long-Distance Growth and Connectivity of Neural Stem Cells after Severe Spinal Cord Injury. *Cell* **150,** 1264–1273 (2012).

161. Tong, Z. *et al.* Application of biomaterials to advance induced pluripotent stem cell research and therapy. *The EMBO journal* **34,** 987–1008 (2015).

162. Brunetti, V. *et al.* Neurons sense nanoscale roughness with nanometer sensitivity. *Proceedings of the National Academy of Sciences* **107,** 6264–6269 (2010).

163. Tamplenizza, M. *et al.* Nitric oxide synthase mediates PC12 differentiation induced by the surface topography of nanostructured TiO2. *Journal of Nanobiotechnology* **11,** 35 (2013).

164. Raineteau, O., Rietschin, L., Gradwohl, G., Guillemot, F. & Gähwiler, B. H. Neurogenesis in hippocampal slice cultures. *Molecular and Cellular Neuroscience* **26,** 241–250 (2004).

165. Cheyne, J. E. *et al.* Synaptic integration of newly generated neurons in rat dissociated hippocampal cultures. *Molecular and Cellular Neuroscience* **47,** 203–214 (2011).

166. Chiappalone, M., Bove, M., Vato, A., Tedesco, M. & Martinoia, S. Dissociated cortical networks show spontaneously correlated activity patterns during in vitro development. *Brain Research* **1093,** 41–53 (2006).

167. Wagenaar, D. A., Pine, J. & Potter, S. M. An extremely rich repertoire of bursting patterns during the development of cortical cultures. *BMC Neuroscience* **7,** 11 (2006).

168. Barborini, E., Piseri, P., Podesta', A. & Milani, P. Cluster beam microfabrication of patterns of three-dimensional nanostructured objects. *Applied Physics Letters* **77,** 1059 (2000).

169. Marelli, M. *et al.* Flexible and biocompatible microelectrode arrays fabricated by supersonic cluster beam deposition on SU-8. *Journal of Micromechanics and Microengineering* **21,** 045013 (2011).

170. Shirure, V. S. & George, S. C. Design considerations to minimize the impact of drug absorption in polymer-based organ-on-a-chip platforms. *Lab on a Chip* **17,** 681–690 (2017).

171. Ware, B. R., Berger, D. R. & Khetani, S. R. Prediction of Drug-Induced Liver Injury in Micropatterned Co-cultures Containing iPSC-Derived Human Hepatocytes. *Toxicological Sciences: An Official Journal of the Society of Toxicology* **145,** 252–262 (2015).

172. Phan, D. T. *et al.* Blood-brain barrier-on-a-chip: Microphysiological systems that capture the complexity of the blood-central nervous system interface. *Experimental Biology and Medicine (Maywood, N.J.)* **242,** 1669–1678 (2017).

173. Huh, D. *et al.* Reconstituting Organ-Level Lung Functions on a Chip. *Science* **328,** 1662–1668 (2010).

174. Park, T. H. & Shuler, M. L. Integration of Cell Culture and Microfabrication Technology. *Biotechnology Progress* **19,** 243–253 (2003).

175. Marinval, N. & Chew, S. Y. Mechanotransduction assays for neural regeneration strategies: A focus on glial cells. *APL Bioengineering* **5,** 021505 (2021).

176. Bechler, M. E., Byrne, L. & Ffrench-Constant, C. CNS Myelin Sheath Lengths Are an Intrinsic Property of Oligodendrocytes. *Current biology: CB* **25,** 2411–2416 (2015).

177. Peyrin, J.-M. *et al.* Axon diodes for the reconstruction of oriented neuronal networks in microfluidic chambers. *Lab on a Chip* **11,** 3663–3673 (2011).

178. Brewer, G. *et al.* Toward a self-wired active reconstruction of the hippocampal trisynaptic loop: DG-CA3. *Frontiers in Neural Circuits* **7,** 165 (2013).

179. Wheeler, B. & Brewer, G. Designing Neural Networks in Culture. *Proceedings of the IEEE* **98,** 398–406 (2010).

180. Shein-Idelson, M., Cohen, G., Ben-Jacob, E. & Hanein, Y. Modularity Induced Gating and Delays in Neuronal Networks. *PLOS Computational Biology* **12,** e1004883 (2016).

181. Raos, B. J. *et al.* Patterning of functional human astrocytes onto parylene-C/SiO_2 substrates for the study of Ca^{2+} dynamics in astrocytic networks. *Journal of Neural Engineering* **15,** 036015 (2018).

182. Jordan, M. D. *et al.* Human astrocytic grid networks patterned in parylene-C inlayed SiO2 trenches. *Biomaterials* **105,** 117–126 (2016).

183. Somjen, G. G. Nervenkitt: notes on the history of the concept of neuroglia. *Glia* **1,** 2–9 (1988).

184. Helmut Kettenmann & Bruce R. Ransom. *Neuroglia* Third Edition (OUP USA, 2013).

185. Salzer, J. L. & Zalc, B. Myelination. *Current Biology* **26,** R971–R975 (2016).

186. Yin, J., Valin, K. L., Dixon, M. L. & Leavenworth, J. W. The Role of Microglia and Macrophages in CNS Homeostasis, Autoimmunity, and Cancer. *Journal of Immunology Research* **2017,** 5150678 (2017).

187. Kettenmann, H. & Verkhratsky, A. *Glial Cells: Neuroglia* (eds Pfaff, D. W. & Volkow, N. D.) 547–578 (Springer, New York, NY, 2016).

188. Volterra, A., Liaudet, N. & Savtchouk, I. Astrocyte Ca2+ signalling: an unexpected complexity. *Nature Reviews Neuroscience* **15,** 327–335 (2014).

189. Astrocyte calcium signaling: the third wave. **19.**

190. Zhang, Y. & Barres, B. A. Astrocyte heterogeneity: an underappreciated topic in neurobiology. *Current Opinion in Neurobiology. Neuronal and glial cell biology – New technologies* **20,** 588–594 (2010).

191. Haim, L. B. & Rowitch, D. H. Functional diversity of astrocytes in neural circuit regulation. *Nature Reviews Neuroscience* **18,** 31–41 (2017).

192. Oberheim, N. A., Goldman, S. A. & Nedergaard, M. in *Astrocytes* (ed Milner, R.) 23–45 (Humana Press, Totowa, NJ, 2012).

193. Bushong, E. A., Martone, M. E., Jones, Y. Z. & Ellisman, M. H. Protoplasmic Astrocytes in CA1 Stratum Radiatum Occupy Separate Anatomical Domains. *The Journal of Neuroscience* **22,** 183–192 (2002).

194. Rusakov, D. A. Disentangling calcium-driven astrocyte physiology. *Nature Reviews Neuroscience* **16,** 226–233 (2015).

195. Arizono, M. *et al.* Structural basis of astrocytic Ca2+ signals at tripartite synapses. *Nature Communications* **11,** 1906 (Apr. 20, 2020).

196. Stobart, J. L. *et al.* Cortical Circuit Activity Evokes Rapid Astrocyte Calcium Signals on a Similar Timescale to Neurons. *Neuron* **98,** 726–735.e4 (2018).

197. Mathiesen, C., Brazhe, A., Thomsen, K. & Lauritzen, M. Spontaneous Calcium Waves in Bergman Glia Increase with Age and Hypoxia and may Reduce Tissue Oxygen. *Journal of Cerebral Blood Flow & Metabolism* **33,** 161–169 (2013).

198. Marina, N. *et al.* Astrocytes monitor cerebral perfusion and control systemic circulation to maintain brain blood flow. *Nature Communications* **11,** 131 (2020).

199. Semyanov, A., Henneberger, C. & Agarwal, A. Making sense of astrocytic calcium signals — from acquisition to interpretation. *Nature Reviews Neuroscience* **21,** 551–564 (2020).

200. Serrano, A., Haddjeri, N., Lacaille, J.-C. & Robitaille, R. GABAergic Network Activation of Glial Cells Underlies Hippocampal Heterosynaptic Depression. *Journal of Neuroscience* **26,** 5370–5382 (2006).

201. Pfrieger, F. W. Role of glia in synapse development. *Current Opinion in Neurobiology* **12,** 486–490 (2002).

202. Scemes, E. & Spray, D. C. in *Advances in Molecular and Cell Biology* 165–179 (Elsevier, 2003).

203. Mayorquin, L. C., Rodriguez, A. V., Sutachan, J.-J. & Albarracín, S. L. Connexin-Mediated Functional and Metabolic Coupling Between Astrocytes and Neurons. *Frontiers in Molecular Neuroscience* **11,** 118 (2018).

204. Giaume, C. & McCarthy, K. D. Control of gap-junctional communication in astrocytic networks. *Trends in Neurosciences* **19,** 319–325 (1996).

205. Rose, C. R. & Ransom, B. R. Gap junctions equalize intracellular Na+ concentration in astrocytes. *Glia* **20,** 299–307 (1997).

206. Plata, A. *et al.* Astrocytic Atrophy Following Status Epilepticus Parallels Reduced Ca2+ Activity and Impaired Synaptic Plasticity in the Rat Hippocampus. *Frontiers in Molecular Neuroscience* **11,** 215 (2018).

207. Genetic Deletion of TREK-1 or TWIK-1/TREK-1 Potassium Channels does not Alter the Basic Electrophysiological Properties of Mature Hippocampal Astrocytes In Situ. **10.**

208. Kang, J., Jiang, L., Goldman, S. A. & Nedergaard, M. Astrocyte-mediated potentiation of inhibitory synaptic transmission. *Nature Neuroscience* **1,** 683–692 (1998).

209. Charles, A. C. Glia-Neuron Intercellular Calcium Signaling. *Developmental Neuroscience* **16,** 196–206 (1994).

210. Mulligan, S. J. & MacVicar, B. A. Calcium transients in astrocyte endfeet cause cerebrovascular constrictions. *Nature* **431,** 195–199 (2004).

211. Nett, W. J., Oloff, S. H. & McCarthy, K. D. Hippocampal Astrocytes In Situ Exhibit Calcium Oscillations That Occur Independent of Neuronal Activity. *Journal of Neurophysiology* **87,** 528–537 (2002).

212. Parri, H. R., Gould, T. M. & Crunelli, V. Spontaneous astrocytic Ca2+ oscillations in situ drive NMDAR-mediated neuronal excitation. *Nature Neuroscience* **4,** 803–812 (2001).

213. McNeill, J., Rudyk, C., Hildebrand, M. E. & Salmaso, N. Ion Channels and Electrophysiological Properties of Astrocytes: Implications for Emergent Stimulation Technologies. *Frontiers in Cellular Neuroscience* **15,** 183 (2021).

214. Cornell-Bell, A., Finkbeiner, S., Cooper, M. & Smith, S. Glutamate induces calcium waves in cultured astrocytes: long-range glial signaling. *Science* **247,** 470–473 (1990).

215. Smith, S. J. in *Progress in Brain Research* (eds Yu, A. C. H., Hertz, L., Norenberg, M. D., Syková, E. & Waxman, S. G.) 119–136 (Elsevier, 1992).

216. Weissman, T. A., Riquelme, P. A., Ivic, L., Flint, A. C. & Kriegstein, A. R. Calcium Waves Propagate through Radial Glial Cells and Modulate Proliferation in the Developing Neocortex. *Neuron* **43,** 647–661 (2004).

217. Willmott, N. J., Wong, K. & Strong, A. J. Intercellular Ca2+ waves in rat hippocampal slice and dissociated glial–neuron cultures mediated by nitric oxide. *FEBS Letters* **487,** 239–247 (2000).

218. Höfer, T., Venance, L. & Giaume, C. Control and Plasticity of Intercellular Calcium Waves in Astrocytes: A Modeling Approach. *Journal of Neuroscience* **22,** 4850–4859 (2002).

219. Leybaert, L. & Sanderson, M. J. in *Connexin Methods and Protocols* (eds Bruzzone, R. & Giaume, C.) 407–430 (Humana Press, Totowa, NJ, 2001).

220. Arcuino, G. *et al.* Intercellular calcium signaling mediated by point-source burst release of ATP. *Proceedings of the National Academy of Sciences* **99,** 9840–9845 (2002).

221. Fujii, Y., Maekawa, S. & Morita, M. Astrocyte calcium waves propagate proximally by gap junction and distally by extracellular diffusion of ATP released from volume-regulated anion channels. *Scientific Reports* **7,** 1–15 (2017).

222. Scemes, E. & Giaume, C. Astrocyte calcium waves: What they are and what they do. *Glia* **54,** 716–725 (2006).

223. Maragakis, N. J. & Rothstein, J. D. Mechanisms of Disease: astrocytes in neurodegenerative disease. *Nature Clinical Practice Neurology* **2,** 679–689 (2006).

224. Kim, W. T., Rioult, M. G. & Cornell-Bell, A. H. Glutamate-induced calcium signaling in astrocytes. *Glia* **11,** 173–184 (1994).

225. Charles, A. C., Merrill, J. E., Dirksen, E. R. & Sanderson, M. J. Intercellular signaling in glial cells: calcium waves and oscillations in response to mechanical stimulation and glutamate. *Neuron,* 983–992 (1991).

226. Tóth, R. *et al.* Astrocyte Ca2+ Waves and Subsequent Non-Synchronized Ca2+ Oscillations Coincide with Arteriole Diameter Changes in Response to Spreading Depolarization. *International Journal of Molecular Sciences,* 3442 (2021).

227. Berridge, M. J. & Galione, A. Cytosolic calcium oscillators. *The FASEB Journal* **2,** 3074–3082 (1988).

228. Wakui, M., Osipchuk, Y. V. & Petersen, O. H. Receptor-activated cytoplasmic Ca2+ spiking mediated by inositol trisphosphate is due to Ca2+-induced Ca2+ release. *Cell,* 1025–1032 (1990).

229. Haas, B. *et al.* Activity-dependent ATP-waves in the mouse neocortex are independent from astrocytic calcium waves. *Cerebral Cortex (New York, N.Y.: 1991)* **16,** 237–246 (2006).

230. Schipke, C. G., Boucsein, C., Ohlemeyer, C., Kirchhoff, F. & Kettenmann, H. Astrocyte Ca2+ waves trigger responses in microglial cells in brain slices. *FASEB journal: official publication of the Federation of American Societies for Experimental Biology* **16,** 255–257 (2002).

231. Rungta, R. L. *et al.* Ca2+ transients in astrocyte fine processes occur via Ca2+ influx in the adult mouse hippocampus. *Glia* **64,** 2093–2103 (2016).

232. Verisokin, A. Y., Verveyko, D. V., Postnov, D. E. & Brazhe, A. R. Modeling of Astrocyte Networks: Toward Realistic Topology and Dynamics. *Frontiers in Cellular Neuroscience* **15,** 50 (2021).

233. Houades, V. *et al.* Shapes of astrocyte networks in the juvenile brain. *Neuron Glia Biology* **2,** 3–14 (2006).

234. Oberheim, N. A. *et al.* Uniquely Hominid Features of Adult Human Astrocytes. *Journal of Neuroscience* **29** (2009).

235. Savtchouk, I. & Volterra, A. Gliotransmission: Beyond Black-and-White. *Journal of Neuroscience* **38,** 14–25 (2018).

236. Santello, M., Toni, N. & Volterra, A. Astrocyte function from information processing to cognition and cognitive impairment. *Nature Neuroscience* **22,** 154–166 (2019).

237. Giaume, C. & Theis, M. Pharmacological and genetic approaches to study connexin-mediated channels in glial cells of the central nervous system. *Brain Research Reviews* **63,** 160–176 (2010).

238. Escartin, C., Guillemaud, O. & Carrillo-de Sauvage, M.-A. Questions and (some) answers on reactive astrocytes. *Glia* **67,** 2221–2247 (2019).

239. Escartin, C. *et al.* Reactive astrocyte nomenclature, definitions, and future directions. *Nature Neuroscience,* 1–14 (2021).

240. Anderson, M. A., Ao, Y. & Sofroniew, M. V. Heterogeneity of reactive astrocytes. *Neuroscience Letters* **565,** 23–29 (2014).

241. Herrmann, J. E. *et al.* STAT3 is a critical regulator of astrogliosis and scar formation after spinal cord injury. *The Journal of Neuroscience: The Official Journal of the Society for Neuroscience,* 7231–7243 (2008).

242. Wanner, I. B. *et al.* Glial Scar Borders Are Formed by Newly Proliferated, Elongated Astrocytes That Interact to Corral Inflammatory and Fibrotic Cells via STAT3-Dependent Mechanisms after Spinal Cord Injury. *Journal of Neuroscience* **33,** 12870–12886 (2013).

243. Bardehle, S. *et al.* Live imaging of astrocyte responses to acute injury reveals selective juxtavascular proliferation. *Nature Neuroscience* **16,** 580–586 (2013).

244. Wilhelmsson, U. *et al.* Redefining the concept of reactive astrocytes as cells that remain within their unique domains upon reaction to injury. *Proceedings of the National Academy of Sciences of the United States of America,* 17513–17518 (2006).

245. Olabarria, M., Noristani, H. N., Verkhratsky, A. & Rodríguez, J. J. Concomitant astroglial atrophy and astrogliosis in a triple transgenic animal model of Alzheimer's disease. *Glia* **58,** 831–838 (2010).

246. Rossi, D. *et al.* Focal degeneration of astrocytes in amyotrophic lateral sclerosis. *Cell Death & Differentiation* **15,** 1691–1700 (2008).

247. Black, J. A., Newcombe, J. & Waxman, S. G. Astrocytes within multiple sclerosis lesions upregulate sodium channel Nav1.5. *Brain: A Journal of Neurology* **133,** 835–846 (Pt 3 2010).

248. Oberheim, N. A. *et al.* Loss of astrocytic domain organization in the epileptic brain. *The Journal of Neuroscience: The Official Journal of the Society for Neuroscience* **28,** 3264–3276 (2008).

249. Sun, D. & Jakobs, T. C. Structural Remodeling of Astrocytes in the Injured CNS. *The Neuroscientist* **18,** 567–588 (2012).

250. Hol, E. M. & Pekny, M. Glial fibrillary acidic protein (GFAP) and the astrocyte intermediate filament system in diseases of the central nervous system. *Current Opinion in Cell Biology. Cell architecture* **32,** 121–130 (2015).

251. Liddelow, S. A. & Barres, B. A. Reactive Astrocytes: Production, Function, and Therapeutic Potential. *Immunity* **46,** 957–967 (2017).

252. Orre, M. *et al.* Isolation of glia from Alzheimer's mice reveals inflammation and dysfunction. *Neurobiology of Aging* **35,** 2746–2760 (2014).

253. Zamanian, J. L. *et al.* Genomic Analysis of Reactive Astrogliosis. *Journal of Neuroscience* **32,** 6391–6410 (2012).

254. Pekny, M., Wilhelmsson, U., Tatlisumak, T. & Pekna, M. Astrocyte activation and reactive gliosis—A new target in stroke? *Neuroscience Letters. Spatio-temporal organisation of astroglial cellular signalling in physiology and pathophysiology* **689,** 45–55 (2019).

255. Perez-Nievas, B. G. & Serrano-Pozo, A. Deciphering the Astrocyte Reaction in Alzheimer's Disease. *Frontiers in Aging Neuroscience* **10,** 114 (2018).

256. Sirko, S. *et al.* Reactive Glia in the Injured Brain Acquire Stem Cell Properties in Response to Sonic Hedgehog. *Cell Stem Cell* **12,** 426–439 (2013).

257. Wang, L. *et al.* Tissue and cellular rigidity and mechanosensitive signaling activation in Alexander disease. *Nature Communications* **9,** 1899 (2018).

258. Wolf, J. A., Stys, P. K., Lusardi, T., Meaney, D. & Smith, D. H. Traumatic Axonal Injury Induces Calcium Influx Modulated by Tetrodotoxin-Sensitive Sodium Channels. *Journal of Neuroscience* **21,** 1923–1930 (2001).

259. Smith, D. H., Johnson, V. E. & Stewart, W. Chronic neuropathologies of single and repetitive TBI: substrates of dementia? *Nature Reviews Neurology* **9,** 211–221 (2013).

260. Levy Nogueira, M. *et al.* Mechanical stress related to brain atrophy in Alzheimer's disease. *Alzheimer's & Dementia: The Journal of the Alzheimer's Association* **12,** 11–20 (2016).

261. Levy Nogueira, M. *et al.* Mechanical stress increases brain amyloid beta, tau, and alpha-synuclein concentrations in wild-type mice. *Alzheimer's & Dementia* **14,** 444–453 (2018).

262. Moeendarbary, E. *et al.* The soft mechanical signature of glial scars in the central nervous system. *Nature Communications* **8,** 14787 (2017).

263. Weickenmeier, J. *et al.* Brain stiffness increases with myelin content. *Acta Biomaterialia* **42,** 265–272 (2016).

264. Chen, X. *et al.* A Feedforward Mechanism Mediated by Mechanosensitive Ion Channel PIEZO1 and Tissue Mechanics Promotes Glioma Aggression. *Neuron* **100,** 799–815.e7 (2018).

265. Hemphill, M. A., Dauth, S., Yu, C. J., Dabiri, B. E. & Parker, K. K. Traumatic Brain Injury and the Neuronal Microenvironment: A Potential Role for Neuropathological Mechanotransduction. *Neuron* **85,** 1177–1192 (2015).

266. Moshayedi, P. *et al.* Mechanosensitivity of astrocytes on optimized polyacrylamide gels analyzed by quantitative morphometry. *Journal of Physics: Condensed Matter* **22,** 194114 (2010).

267. Gottipati, M. K., Zuidema, J. M. & Gilbert, R. J. Biomaterial strategies for creating in vitro astrocyte cultures resembling in vivo astrocyte morphologies and phenotypes. *Current Opinion in Biomedical Engineering. Tissue Engineering and Regenerative Medicine: Brain organoids/Brain tissue engineering - As disease model and for understanding* **14,** 67–74 (2020).

268. Wang, H., Tewari, A., Einheber, S., Salzer, J. L. & Melendez-Vasquez, C. V. Myosin II has distinct functions in PNS and CNS myelin sheath formation. *Journal of Cell Biology* **182,** 1171–1184 (2008).

269. Lourenço, T. *et al.* Modulation of oligodendrocyte differentiation and maturation by combined biochemical and mechanical cues. *Scientific Reports* **6,** 21563 (2016).

270. Stretch-activated ion channel Piezo1 directs lineage choice in human neural stem cells. **111.**

271. East, E., Golding, J. P. & Phillips, J. B. A versatile 3D culture model facilitates monitoring of astrocytes undergoing reactive gliosis. *Journal of Tissue Engineering and Regenerative Medicine* **3,** 634–646 (2009).

272. Frampton, J. P., Hynd, M. R., Shuler, M. L. & Shain, W. Fabrication and optimization of alginate hydrogel constructs for use in 3D neural cell culture. *Biomedical Materials (Bristol, England)* **6,** 015002 (2011).

273. Galarza, S., Crosby, A., Pak, C. & Peyton, S. *Control of Astrocyte Quiescence and Activation in a Synthetic Brain Hydrogel* (2019).

274. Nagano, N., Aoyagi, M. & Hirakawa, K. Extracellular matrix modulates the proliferation of rat astrocytes in serum-free culture. *Glia* **8,** 71–76 (1993).

275. Martín-López, E., Alonso, F. R., Nieto-Díaz, M. & Nieto-Sampedro, M. Chitosan, gelatin and poly(L-lysine) polyelectrolyte-based scaffolds and films for neural tissue engineering. *Journal of Biomaterials Science. Polymer Edition* **23,** 207–232 (2012).

276. Hsiao, T. W., Tresco, P. A. & Hlady, V. Astrocytes alignment and reactivity on collagen hydrogels patterned with ECM proteins. *Biomaterials* **39,** 124–130 (2015).

277. Silver, J. & Miller, J. H. Regeneration beyond the glial scar. *Nature Reviews Neuroscience* **5,** 146–156 (2004).

278. Ereifej, E. S. *et al.* Nanopatterning effects on astrocyte reactivity. *Journal of Biomedical Materials Research. Part A,* 1743–1757 (2013).

279. Lansky, Z. *et al.* 3D mapping of native extracellular matrix reveals cellular responses to the microenvironment. *Journal of Structural Biology: X* **1,** 100002 (2019).

280. Kim, D.-H., Provenzano, P. P., Smith, C. L. & Levchenko, A. Matrix nanotopography as a regulator of cell function. *Journal of Cell Biology* **197,** 351–360 (2012).

281. Ong, W. *et al.* Microfiber drug/gene delivery platform for study of myelination. *Acta Biomaterialia* **75,** 152–160 (2018).

282. Curtis, A. & Wilkinson, C. Topographical control of cells. *Biomaterials* **18,** 1573–1583 (1997).

283. Puschmann, T. B. *et al.* Bioactive 3D cell culture system minimizes cellular stress and maintains the in vivo-like morphological complexity of astroglial cells. *Glia* **61,** 432–440 (2013).

284. Cao, H. *et al.* The effects of nanofiber topography on astrocyte behavior and gene silencing efficiency. *Macromolecular Bioscience* **12,** 666–674 (2012).

285. Lau, C. L. *et al.* 3D Electrospun scaffolds promote a cytotrophic phenotype of cultured primary astrocytes. *Journal of Neurochemistry* **130,** 215–226 (2014).

286. Gottipati, M. K. *et al.* Chemically Functionalized Single-Walled Carbon Nanotube Films Modulate the Morpho-Functional and Proliferative Characteristics of Astrocytes. *Nano Letters* **13,** 4387–4392 (2013).

287. Johnson, C. D. L. *et al.* The Effect of Electrospun Fiber Diameter on Astrocyte-Mediated Neurite Guidance and Protection. *ACS Applied Bio Materials* **2,** 104–117 (2019).

288. Mirigliano, M. *Characterization of nanostructured films with non-linear electrical properties for the fabrication of neuromorphic devices and unconventional data processing* PhD thesis (Università degli Studi di Milano, 2021).

289. Tafreshi, H. V. *et al.* A Simple Nozzle Configuration for the Production of Low Divergence Supersonic Cluster Beam by Aerodynamic Focusing. *Aerosol Science and Technology* **36,** 593–606 (2002).

290. Piseri, P., Podestà, A., Barborini, E. & Milani, P. Production and characterization of highly intense and collimated cluster beams by inertial focusing in supersonic expansions. *Review of Scientific Instruments* **72,** 2261–2267 (2001).

291. Barborini, E *et al.* Batch fabrication of metal oxide sensors on micro-hotplates. *Journal of Micromechanics and Microengineering* **18,** 055015 (2008).

292. Weydert, S. *et al.* Easy to Apply Polyoxazoline-Based Coating for Precise and Long-Term Control of Neural Patterns. *Langmuir* **33,** 8594–8605 (2017).

293. Henini, M. Handbook of Thin-Film Deposition Processes and Techniques. *Microelectronics Journal* **31,** 219 (2000).

294. Conrads, H. & Schmidt, M. Plasma generation and plasma sources. *Plasma Sources Science and Technology* **9,** 441–454 (2000).

295. Kang, M. & Othmer, H. G. Spatiotemporal characteristics of calcium dynamics in astrocytes. *Chaos: An Interdisciplinary Journal of Nonlinear Science* **19,** 037116 (2009).

296. Wang, Z., Haydon, P. G. & Yeung, E. S. Direct Observation of Calcium-Independent Intercellular ATP Signaling in Astrocytes. *Analytical Chemistry* **72,** 2001–2007 (2000).

297. Newman, E. A. Propagation of Intercellular Calcium Waves in Retinal Astrocytes and Müller Cells. *Journal of Neuroscience* **21,** 2215–2223 (2001).

298. Venance, L., Stella, N., Glowinski, J. & Giaume, C. Mechanism Involved in Initiation and Propagation of Receptor-Induced Intercellular Calcium Signaling in Cultured Rat Astrocytes. *The Journal of Neuroscience* **17,** 1981–1992 (1997).

299. Kruskal, W. H. & Wallis, W. A. Use of Ranks in One-Criterion Variance Analysis. *Journal of the American Statistical Association* **47,** 583–621 (1952).

300. Dunn, O. J. Multiple Comparisons among Means. *Journal of the American Statistical Association* **56,** 52–64 (1961).

301. Rao, S. S. *et al.* Glioblastoma Behaviors in Three-Dimensional Collagen-Hyaluronan Composite Hydrogels. *ACS Applied Materials & Interfaces* **5,** 9276–9284 (2013).

302. Sofroniew, M. V. & Vinters, H. V. Astrocytes: biology and pathology. *Acta Neuropathologica* **119,** 7–35 (2010).

303. McKenzie, J. L., Waid, M. C., Shi, R. & Webster, T. J. Decreased functions of astrocytes on carbon nanofiber materials. *Biomaterials* **25,** 1309–1317 (2004).

304. Hu, W.-w. *et al.* Morphology and functions of astrocytes cultured on water-repellent fractal tripalmitin surfaces. *Biomaterials* **35,** 7386–7397 (2014).

305. Wilson, C. L., Hayward, S. L. & Kidambi, S. Astrogliosis in a dish: substrate stiffness induces astrogliosis in primary rat astrocytes. *RSC advances* **6,** 34447–34457 (2016).

306. Kanchanawong, P. *et al.* Nanoscale architecture of integrin-based cell adhesions. *Nature* **468,** 580–584 (2010).

307. Singh, A. V. *et al.* Astrocytes Increase ATP Exocytosis Mediated Calcium Signaling in Response to Microgroove Structures. *Scientific Reports* **5,** 7847 (2015).

308. Cotrina, M. L., Lin, J. H.-C. & Nedergaard, M. Cytoskeletal Assembly and ATP Release Regulate Astrocytic Calcium Signaling. *Journal of Neuroscience* **18,** 8794–8804 (1998).

309. Hansson, E. Actin Filament Reorganization in Astrocyte Networks is a Key Functional Step in Neuroinflammation Resulting in Persistent Pain: Novel Findings on Network Restoration. *Neurochemical Research* **40,** 372–379 (2015).

310. Hansson, E., Werner, T., Björklund, U. & Skiöldebrand, E. Therapeutic innovation: Inflammatory-reactive astrocytes as targets of inflammation. *IBRO Reports* **1,** 1–9 (2016).

311. Sergeeva, M, Ubl, J. J & Reiser, G. Disruption of actin cytoskeleton in cultured rat astrocytes suppresses ATP- and bradykinin-induced [Ca2+]i oscillations by reducing the coupling efficiency between Ca2+ release, capacitative Ca2+ entry, and store refilling. *Neuroscience* **97,** 765–769 (2000).

312. Wu, Y.-W. *et al.* Morphological profile determines the frequency of spontaneous calcium events in astrocytic processes. *Glia* **67,** 246–262 (2019).

313. Spatiotemporal pattern of calcium activity in astrocytic network. *Cell Calcium* **78,** 15–25 (2019).

314. Denizot, A., Arizono, M., Nägerl, U. V., Soula, H. & Berry, H. Simulation of calcium signaling in fine astrocytic processes: Effect of spatial properties on spontaneous activity. *PLOS Computational Biology* **15,** e1006795 (2019).

315. Stobart, J. L. *et al.* Long-term In Vivo Calcium Imaging of Astrocytes Reveals Distinct Cellular Compartment Responses to Sensory Stimulation. *Cerebral Cortex (New York, N.Y.: 1991)* **28,** 184–198 (2018).

316. Molotkov, D., Zobova, S., Arcas, J. M. & Khiroug, L. Calcium-induced outgrowth of astrocytic peripheral processes requires actin binding by Profilin-1. *Cell Calcium* **53,** 338–348 (2013).

317. Tanaka, M. *et al.* Astrocytic Ca2+ signals are required for the functional integrity of tripartite synapses. *Molecular Brain* **6,** 6 (2013).

318. Durkee, C. A. & Araque, A. Diversity and Specificity of Astrocyte–neuron Communication. *Neuroscience* **396,** 73–78 (2019).

319. Sasaki, T., Kuga, N., Namiki, S., Matsuki, N. & Ikegaya, Y. Locally synchronized astrocytes. *Cerebral Cortex (New York, N.Y.: 1991)* **21,** 1889–1900 (2011).

320. Matias, I., Morgado, J. & Gomes, F. C. A. Astrocyte Heterogeneity: Impact to Brain Aging and Disease. *Frontiers in Aging Neuroscience* **11,** 59 (2019).

321. Kimelberg, H. K. The problem of astrocyte identity. *Neurochemistry International. Glial Biology: Functional Interactions Among Glia and Neurons* **45,** 191–202 (2004).

322. Spallazzi, M. *et al.* Hippocampal vascularization patterns: A high-resolution 7 Tesla time-of-flight magnetic resonance angiography study. *NeuroImage: Clinical* **21,** 101609 (2019).

323. Xiong, B. *et al.* Precise Cerebral Vascular Atlas in Stereotaxic Coordinates of Whole Mouse Brain. *Frontiers in Neuroanatomy* **11,** 128 (2017).

324. Liewald, D., Miller, R., Logothetis, N., Wagner, H.-J. & Schüz, A. Distribution of axon diameters in cortical white matter: an electron-microscopic study on three human brains and a macaque. *Biological Cybernetics* **108,** 541–557 (2014).

325. Leclech, C., Natale, C. F. & Barakat, A. I. The basement membrane as a structured surface - role in vascular health and disease. *Journal of Cell Science* **133,** jcs239889 (2020).

326. Giaume, C. Astroglial Wiring is Adding Complexity to Neuroglial Networking. *Frontiers in Neuroenergetics* **2** (2010).

327. Houades, V., Koulakoff, A., Ezan, P., Seif, I. & Giaume, C. Gap junction-mediated astrocytic networks in the mouse barrel cortex. *The Journal of Neuroscience: The Official Journal of the Society for Neuroscience* **28,** 5207–5217 (2008).

328. Roux, L., Benchenane, K., Rothstein, J. D., Bonvento, G. & Giaume, C. Plasticity of astroglial networks in olfactory glomeruli. *Proceedings of the National Academy of Sciences* **108,** 18442–18446 (2011).

329. Pannasch, U. & Rouach, N. Emerging role for astroglial networks in information processing: from synapse to behavior. *Trends in Neurosciences* **36,** 405–417 (2013).

330. Dokukina, I. V., Gracheva, M. E., Grachev, E. A. & Gunton, J. D. Role of network connectivity in intercellular calcium signaling. *Physica D: Nonlinear Phenomena* **237,** 745–754 (2008).

331. Lallouette, J., de Pitta, M., Ben-Jacob, E. & Berry, H. Spare short-distance connections enhance calcium wave propagation in a 3D model of astrocyte networks. **8,** 45 (Apr. 2014).

332. Previdi, A. *et al.* Micropatterning of Substrates for the Culture of Cell Networks by Stencil-Assisted Additive Nanofabrication. *Micromachines* **12,** 94 (2021).

333. Liddelow, S. & Hoyer, D. Astrocytes: Adhesion Molecules and Immunomodulation. *Current Drug Targets* **17,** 1871–1881 (2016).

Acknowledgements

I wish to show my appreciation to all the people who contributed to this thesis.

In particular, I would like to thank my supervisor, Prof. Paolo Milani, for his consistent guidance and encouragement during the running of this project.

I am grateful to Prof. Cristina Lenardi, who was my tutor during the first year and greatly helped me navigate the world of research.

I also wish to thank Prof. Antonio Malgaroli and the people from the BNC (Università Vita-Salute San Raffaele), Jacopo Lamanna, Andrea Moro, Sara Gabriella Racchetti, Sara Spadini, who have greatly contributed to the neuroscientifical side of this work and were of great patience in helping me with the cell culture and all the calcium imaging experiments.

Many thanks to Dr. Leandro Lorenzelli, for providing the silicon stencil masks, essential for this work.

Also, I am thankful to all the scientists from the CIMaINA group who supported me during these three years of work. Carsten Schulte, who has accompanied me in the first steps of a physicist in a biology lab and who has been of incredible support in helping me with the experimental work. Claudio Piazzoni, a steady presence in fabbrica, helping me with the SCBD. Francesca Borghi, for the endless scientific discussions and who was always there for me when I needed a boost of confidence. Prof. Paolo Piseri and Prof. Alessandro Podestà, for the precious advice, conversations and the support in the lab. Prof. Marcel Di Vece, who gave me the chance to tutor his courses.

A warm thank to my collegues, Sara and Matteo M. (grande cosa la pazienza), Matteo C., Hatice, Ewelina, Matteo G., Francesca O., Marco, Lorenzo, Tommaso. You have been the greatest team and you gave me both scientific support and the greatest laughs, along with the students I was lucky enough to meet during the PhD, especially Filippo, Gianluca and Chiara.

A special thank also to the Officina Meccanica of the Physics department, in particular Francesco Cavaliere, Federico Pezzotta, Daniele Viganò and William Merli, for

manufacturing with the greatest precision and competence all the mechanical parts necessary for experimental work. I had great fun working with you.

Lastly, I want to thank all the people that are not part of this project, but have indirectly supported me during the years of PhD. My friends Nebo, Jeffrey, Simone, Martina, Alice, Cecilia, Marta and Andy. My family and Giacomo, for always being there for me.